UNIVERSITÀ DEGLI STUDI DI MILANO

Scuola di Dottorato in Fisica, Astrofisica e Fisica Applicata

Dipartimento di Fisica

Corso di Dottorato in Fisica, Astrofisica e Fisica Applicata

Ciclo XXIX

Maximum Muon Production Depth and its fluctuations above 15 EeV at the Pierre Auger Observatory: mass composition and constraints on hadronic interaction models

Settore Scientifico Disciplinare FIS/04

Supervisor: Professor Lino MIRAMONTI

Co-Supervisor: Dott. Barbara CACCIANIGA

Coordinator: Professor Francesco RAGUSA

Tesi di Dottorato di:

Manuela Mallamaci

Referees:

Prof. Antonio Insolia

Prof. Mosé Mariotti

Commission of the final examination:

External Member:
Prof. Daniele Martello

External Member:
Prof. Rossella Caruso

External Member:
Prof. Alessandro De Angelis

Final examination:

March 20th 2017

Università degli Studi di Milano, Dipartimento di Fisica, Milano, Italy

Al mio Signore Gesu'

"[The study of cosmic rays is] unique in modern physics
for the minuteness of the phenomena,
the delicacy of the observations,
the adventurous excursions of the observers,
the subtlety of the analysis,
and the grandeur of the inferences."
(K.K. Darrow)

Cover illustration:

One of the 1660 Surface Detector stations of the Pierre Auger Observatory, in western Argentina's Pampa Amarilla. The Andes Cordillera is visible in the background.

Image credit: http://www.nature.com/news/astronomy-to-catch-a-cosmic-ray-1.16037

Contents

Introduction

Ultra-High Energy Cosmic Rays (briefly UHECRs) are charged particles observed with energies from 10^{18} eV (= 1 EeV) up to 3×10^{20} eV. Although the first indications of their existence were obtained more than fifty years ago, they remain one of the big mysteries in modern astrophysics. The open points regard their origin and the propagation mechanisms. From the experimental point of view, there are a few observables that can be used in order to answer the fundamental questions about UHECRs: the energy, the mass and the arrival direction.

One of the most significant difficulties about their study is related to the extremely low flux. To have an idea, at 10^{20} eV the cosmic ray rate is about 1 particle/km^2/century. As a consequence, their detection can not be performed with balloons probes or satellites and it is necessary to use ground arrays.

Further complications arise because their detection is not direct. Indeed, UHECRs can be measured only through the cascade of secondary particles they produce by the interaction with the atmosphere. This phenomenon is known with the name of *Extensive Air Shower* (briefly EAS). The shower physics is very complex and the properties of secondary particles depend strongly on the primary interaction, which happens at energies greater than those accessed by modern accelerator experiments, like LHC. This implies that UHECR analysis is affected by large uncertainties, as it is based on the extrapolation of measurements performed at lower energies and in different kinematic regions.

The Pierre Auger Observatory, located in Argentina, started to collect data in 2004, with the purpose of investigating the underlying physics of UHECRs. This is the world's largest cosmic ray experiment and it consists of two kinds of detectors: the *Surface Detector* (SD), an array of Water-Cherenkov stations located over an area of 3000 km^2, and the *Fluorescence Detector* (FD), a set of 27 fluorescence telescopes placed around the array. The SD measures the shower footprint on ground, i.e. its lateral development given the signals recorded by the stations. The FD measures the longitudinal shower profile, exploiting the fluorescence light emitted by the passage of the shower through the atmosphere. These measurements allow to extract information about the energy, the mass and the arrival direction of the so-called *primary* CR that induced the secondary particle cascade.

The UHECR spectrum (as for cosmic rays of lower energies) is described by a power-law function. In particular, a change of slope, called *ankle* is observed around 5×10^{18} eV, where the spectral index changes from -3.3 to -2.6. For energies around 4.2×10^{19} eV a cut-off in the flux has been measured with unprecedented precision. These features can be attributed to production processes, propagation mechanisms and/or chemical composition variation. The aim of the presented work is related to this last point, i.e. to

chemical composition.
Establishing the composition at the highest energies is of fundamental importance from the astrophysical point of view, since it could discriminate between different scenarios of origin and propagation of cosmic rays. However, composition studies on a shower to shower basis are challenging because of the intrinsic shower-to-shower fluctuations, which characterise shower properties. These fluctuations come from the statistical nature of the interaction processes, in particular the height of the first interaction. Showers originating from different primaries can be distinguished, at least statistically, given their different cross sections with air nuclei and distinct hadronic multi-particle production properties. Masses may be inferred by comparing the measured observables to those predicted in Monte Carlo (MC) simulations.
The Pierre Auger Observatory traditionally studies the UHECR mass composition by means of the FD: the mass-sensitive observable is the atmospheric depth where the size of the shower is maximum, called X_{max}. Showers induced by light nuclei will have a deeper X_{max} with respect to showers induced by heavier nuclei. Besides, the fluctuations related to X_{max} are another mass-sensitive quantity: for light nuclei the fluctuations will be greater than for heavy nuclei. These properties are described by simple models like the Heitler model, but quantitative predictions are possible only by using detailed MC simulations of the EAS. On the basis of the current predictions, the X_{max} measurements indicate that the composition is mainly light up to $3{\times}10^{18}$ eV, for higher energies a trend towards heavier composition is observed. The measurements performed with the FD are affected by small systematic uncertainties, but they suffer poor statistics at energies above 10^{19} eV. This is mainly related to the detector duty cycle, which is about 14%.
The Pierre Auger Collaboration has developed alternative and independent researches, in order to extend the measurements to the highest spectrum energies. These studies exploit the SD, whose duty cycle is about 100%.
The subject of this thesis is focused on one of these alternative methods, in particular the reconstruction of the muonic longitudinal profile called *Muon Production Depth* (briefly MPD). This is based on the SD measurement of the muon arrival times from EAS and it is a promising study for many reasons. First of all, the MPD provides two mass-sensitive observables, correlated with those reconstructed by the FD: the X^{μ}_{max}, i.e. the point along the shower axis where the muon production is maximum, and the corresponding fluctuations $\sigma_{sh}(X^{\mu}_{max})$. Secondly, the MPD is a muon-related observable and for this reason it plays an important role in testing the validity of the current hadronic interaction models used for EAS simulations. Indeed, muons, being the secondary products of charged pions and kaons, represent a direct handle to explore the hadronic interactions at energies at least a factor of 10 higher than the collisions produced at the LHC. A significant discrepancy between observations and predictions can thus be interpreted as a possible indication of an incomplete description of hadronic interactions. In particular, independent analyses at the Pierre Auger Observatory, based on muon-related observables, reached the conclusion that the most recent hadronic event generators, QGSJetII-04 and EPOS-LHC, predict less muons than observed.
For what concerns the MPD, the Pierre Auger Collaboration has already published a study about X^{μ}_{max}. The analysis was performed on inclined events with zenith angle between 55° and 65°, energies between 20 EeV (=$10^{19.3}$ eV) and 100 EeV (=10^{20} eV), and sampling muons at distances from the shower core in the range [1700m-4000m].
The scope of the presented study is extending the analysis range in energy (down to 15 EeV $\simeq 10^{19.2}$ eV), zenith angle and distance from the shower core respectively as follows:

- $10^{19.2} \leq \mathrm{E} \leq 10^{20}$ eV
- $45^\circ \leq \theta \leq 65^\circ$
- $1200 \leq \mathrm{r} \leq 4000$ m

The extension of the applicability intervals is important for several reasons: the statistics of events at disposal increase considerably (about a factor 2.5 with respect to the published analysis, without considering about 4 years more of data taken). Besides, the wider distance range increases the number of detected muons and this makes the $\sigma_{sh}(X^{\mu}_{max})$ reconstruction possible. Finally, this extension allows to test the agreement between data and simulations on a larger zenith and energy range.
In this work I will discuss the aforementioned contents. In particular, in the first chapter, I will describe briefly some basic concepts of the UHECR theory. I will explain which is the standard mechanism that accounts for the UHECR production and which are the interactions experienced by UHECRs during their propagation towards the observer. In the second chapter, I will discuss the physics of EAS and, in this context, I will then underline the techniques used for the shower detection. In the third chapter, I will talk about the Pierre Auger Observatory. I will describe the detector components and the energy, mass and direction reconstruction methods. A section will be dedicated to the main experimental results, like those briefly mentioned here. The fourth chapter will be focused on the different composition measurements performed at the Pierre Auger Observatory. The first part will be dedicated to Fluorescence Detector data, the second one to the studies done by means of the Surface Detector.
The subject of the fifth chapter will be the MPD, whose general properties will be illustrated. Its dependence on the distance cut, energy and zenith angle will be described. In the sixth chapter I will introduce the MPD method. The explorable energy, zenith and distance ranges will be defined and I will discuss step by step all the different ingredients needed for the MPD reconstruction chain, like the electromagnetic background subtraction, the detector effect removal and the fit procedure for the extraction of X^{μ}_{max}.
The seventh chapter will be dedicated to the procedure used for obtaining the shower-to-shower fluctuations. In order to do so, the evaluation of the detector resolution is needed. Starting from this quantity and from the observed X^{μ}_{max} distribution, the physical fluctuations, $\sigma_{sh}(X^{\mu}_{max})$, will be derived.
In the last chapter, I will concentrate on MPD data analysis. After a discussion about the systematics, the results of X^{μ}_{max} and $\sigma_{sh}(X^{\mu}_{max})$ will be examined in the light of the MC simulations, which are based on the most recent hadronic interaction models EPOS-LHC and QGSJetII-04.

CHAPTER 1

Ultra-High Energy Cosmic Rays

Until the beginning of the twentieth century, the astrophysicists thought that photons were the only useful probes for investigating the universe. This idea radically changed when they discovered that charged particles coming from outer space continuously "rain" above our heads. Detected with the balloon-borne experiment performed by Victor Hess in 1913, they were called *Cosmic Rays* (CRs briefly). A further fundamental discovery in this field happened later on, in 1938, when the phenomenon of extensive air showers became known. It allowed to investigate the most extreme energies in the universe and, in particular, the so-called *Ultra-High Energy Cosmic Rays* (from now on UHECRs, briefly) .
After a first general overview about cosmic rays (Sec. 1.1), this chapter will address the main issues about UHECRs, which are the subject of this work. These particles, whose energy is greater than 10^{18} eV (=1 EeV), are still a great mystery and represent one of the most puzzling enigmas of modern astrophysics, despite the wealth of exciting experimental results collected in the last decades by detectors reaching apertures as large as tens of thousands $\mathrm{km}^2\ \mathrm{sr\ yr}$.
In this chapter, I will ideally follow the travel of UHECRs from their source to the Earth. After a general introduction, the discussion is thus organised in two parts. In the first one (Sec. 1.2), I will focus on the most accepted mechanism through which such high energies can be reached and if astrophysical environments able to accelerate the UHECRs exist. In the second part (Sec 1.3), I will follow these particles in their path across the intergalactic and/or galactic space, where they lose energy by interaction with photon fields and suffer trajectory deviation by magnetic fields.

1.1 A general overwiew about cosmic rays

Cosmic rays are charged particles coming from space. Their energy spectrum has been measured with very high precision and it extends almost over 13 orders of magnitude in energy and 33 orders of magnitude in flux. Fig. 1.1 shows the cosmic ray energy spectrum, multiplied by E^2, for energies above 10^{11} eV, where it can be described by a series of power-law distributions of the type:

$$\frac{\mathrm{d}N}{\mathrm{d}E\mathrm{d}\Omega\mathrm{d}A\mathrm{d}t} \propto E^{-\gamma} \tag{1.1}$$

with γ called *spectral index*. For energies under 10^{11} eV, the cosmic ray flux consists of charged particles of solar origin and it is thus modulated by the 11-year solar cycle. In addition, it is affected by the geomagnetic field. For this reasons, it can not nbe described by a simple power law function.

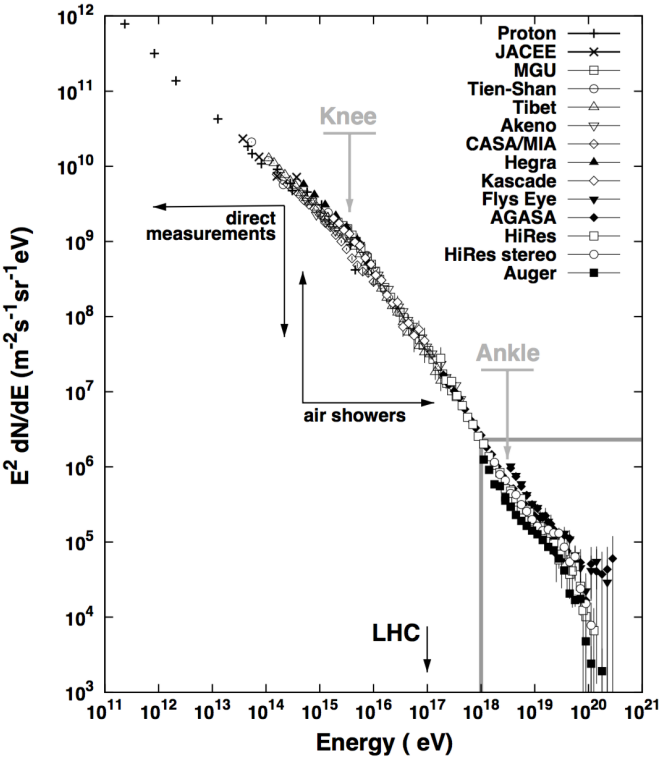

Figure 1.1: Differential energy spectrum of cosmic rays of energy above 10^{11} eV from various experiments. The spectrum is multiplied by E^2. Prominent features like the *knee* and the *ankle* are highlighted. In addition, the type of measurements is shown: for energies > 10^{14} eV cosmic rays are detected through shower of secondary particles they produce in the atmosphere. As a reference, the cosmic ray energy which corresponds to the LHC center-of-mass energy (14 TeV) is shown ($\simeq 10^{17}$ eV).

Looking at Fig. 1.1, it is easy to understand that the cosmic ray flux greatly decreases with the energy. In particular, it amounts to 1 particle per square meter per second at 10^{11} eV, it becomes 1 particle per square kilometer per year above 10^{19} eV and it reduces to less than 1 particle per square kilometer per century at the end of the spectrum. The kind of detection is related to the cosmic ray flux: cosmic rays of energies above 10^{14} eV are difficult to measure by direct experiments performed on balloons and satellites, because they have small areas and can not detect enough particles. At higher energies, cosmic rays are seen indirectly on ground through the cascade of secondary particles they produce, i.e. through the so-called *air showers*. In Fig. 1.1, the cosmic ray flux as a function of the energy is multiplied by E^2 to highlight the changes of the slope, which are briefly summarised here.

- For energies greater than 3×10^{15} eV, the flux starts to decrease more steeply. The spectral index changes from about 2.7 to about 3. This feature is marked with the term *knee*. CRs below and around the knee are generally believed to be accelerated at galactic astrophysical objects, mainly by supernova remnants and possibly by powerful binary systems [1]. In the current understanding, the features seen in the energy spectrum between 10^{15} and 10^{18} eV are compatible with the bending of the different components of CRs, supporting a rigidity dependence of the phenomena. Whether this is related to galactic diffusion mechanisms or limitations of the astrophysical accelerators is still unclear. For a more detailed discussion, refer to [2].

- At about 4.8×10^{18} eV the spectrum flattens and the spectral index returns to 2.6. The corresponding feature on the spectrum is called *ankle* and it could mark the transition between galactic and extragalactic cosmic rays. According to this scenario, the two populations contribute equally to the flux and the former is predicted to have a heavy composition, the latter a light composition mainly. There are also other models proposed to interprete the ankle, like for example the *dip model* [3].

- For energies around 4.2×10^{19} eV a cut-off in the flux is observed with a high degree of significance (see Sec. 3.8). This suppression can be ascribed to interactions with background radiation and/or to a maximum energy of cosmic rays at the sources. The maximum energy to which a particle can be accelerated by astrophysical objects and the propagation effects will be described in Sec. 1.2 and 1.3.

In chapter 4, the possible interpretation of the spectrum in the UHE region, i.e. above 10^{18} eV, together with the composition measurements will be discussed. The flux exhibits another change in slope at about 10^{17} eV, where the spectral index becomes about 3.3. This feature was observed recently and called *second knee*. Its origin is still debated [4].
As briefly outlined, the features of the spectrum reflect changes in the properties of cosmic rays, which can be associated to a variation of the mass composition, sources and/or propagation effect. For what concerns their composition at energies $E<10^{14}$ eV, about 98 % of the cosmic rays are proton and nuclei, while about 2 % are electrons. In particular that 98% is made up of about 80% of protons and the remaining fraction of heavier nuclei. At the UHE energies, the knowledge about chemical composition is incomplete, but this will be discussed in detail in chapter 4.
Fig. 1.1 displays in addition the cosmic ray energy ($\simeq 10^{17}$ eV) which corresponds to the LHC center-of-mass energy energy (14 TeV). It is clear that the ultra-high energies

of these particles are well far above those accessible by man-made particle accelerators. This causes one of the dominating systematic uncertainties in the study of UHECRs, which is therefore very difficult, but fascinating at the same time, because it could give hints of something totally new either in astrophysics or in particle physics.
From now on, I will concentrate on UHECRs.

1.2 Origin of UHECRs

The first issue with the UHECRs concerns their origin. The main question is how a macroscopic amount of energy (up to 20 Joules) can be transferred efficiently to a microscopic particle.
Different ideas were proposed over the years. They can be summarised in two classes:

- *bottom-up* models: according to this scenario, UHECRs are accelerated from astrophysical sources;
- *top-down* models: UHECRs are considered as the decay product of exotic particles.

For this last class of models the acceleration is not necessary, because charged particles emerge directly with ultra-high energy from the decay cascade. However, they require the existence of a new unstable or meta-stable super-massive particle (for example, such as supersymmetric particles or topological defects). Its decay should produce quarks and leptons, which will result in a large cascade of energetic photons, neutrinos, light leptons and a small fraction of protons and neutrons. A fundamental characteristic of these models is therefore the prediction of a large fraction of ultra-high energy photons and neutrinos. The recent observations by the Pierre Auger Observatory put a limit on these fluxes (see Sec. 3.8). This is the reason why top-down processes are now strongly disfavoured as sources for UHECRs.
In the following section, I will focus on the basic concepts of the diffusive shock acceleration mechanism, only related to the bottom-up models.

1.2.1 Diffusive shock acceleration

One of the big mysteries about the highest energy cosmic rays involves the acceleration mechanisms. The original idea was proposed by Fermi [5]: particles can gain energy scattering off randomly moving magnetised clouds. On average this gain per cloud interaction $\langle \Delta E \rangle$ is related to the velocity of the cloud V by:

$$\frac{\langle \Delta E \rangle}{E} = \frac{4}{3}\beta^2 \tag{1.2}$$

where E is the initial particle energy and β = V/c is the cloud velocity. Random velocity of interstellar clouds in the Galaxy are very small, tipically $\beta \approx 10^{-4}$. So, this process, known as *second-order Fermi acceleration*, is not efficient in the acceleration to the observed energies.
An acceleration to the first order in β is supplied by shock waves, for example the shock waves which propagate through the interstellar medium ahead of the supersonic shells of supernova remnants [1] . Every time a particle crosses the shock front, it receives an increase of energy:

$$\frac{\langle \Delta E \rangle}{E} = \frac{4}{3}\beta \tag{1.3}$$

This mechanism is known as *first-order diffusive acceleration*. Given that β can be of the order of 0.1, a particle can gain 10% of its energy.
The success of this model lies in the expected particle energy spectrum:

$$N(E)\mathrm{d}E \propto E^{-2}\mathrm{d}E \tag{1.4}$$

The proposed mechanism provides an excellent physical reason why power-law energy spectra with a unique spectral index should be found in diverse astrophysical environments. Various acceleration mechanisms discussed in the literature include the first order Fermi shock acceleration, here briefly described [6], plasma wakefield acceleration [7] and reconnection [8].
The final observed spectral index will depend therefore on the injection spectrum from sources. Another important element is the maximum energy to which a cosmic ray can be accelerated. The key ingredients regarding the maximum energy can be summarised as follows:

- the acceleration rate, i.e. the rate at which a particle can gain energy from the shock;
- the time a particle remains in the accelerating region before escaping, which is related to the size of the source;
- the energy losses suffered because of interactions with photons and magnetic fields during the acceleration phase.

These points will be briefly addressed in the following subsections.

Acceleration rate

Every time a cosmic ray traverses the shock front, it gains energy. If it is confined, it will have more probability to cross the shock at a high rate, gaining energy at a high rate. Magnetic fields and their configuration with respect to the shock front play a fundamental role in this scenario. Starting from reasonable assumptions, it was shown [9] that for a shock speed of 0.1c, the acceleration rate for first-order acceleration is:

$$\frac{\mathrm{d}E}{\mathrm{d}t} \propto Zec^2B \tag{1.5}$$

Z is the atomic number of the cosmic ray particle and B the magnetic field strength. The confinement (and therefore the acceleration rate) is more effective for a magnetic field perpendicularly oriented with respect to the normal to the shock front. This kind of configuration is (paradoxically) called *perpendicular shock*.
The time a particle remains in the accelerating region depends on the so called *Larmor radius*. This is the radius of the helical path followed by a relativistic particle which moves in a uniform magnetic field. It is given by the formula:

$$r_L = 1.08\frac{E_{15}}{ZB_{\mu G}}\ \mathrm{pc} \tag{1.6}$$

E_{15} is the energy in units of 10^{15} eV and B is in units of μG and the Larmor radius r_L is given in units of parsec (1 pc is approximately 3.2 light years). Higher Z particles have a smaller Larmor radii, so they diffuse away from the shock more slowly.

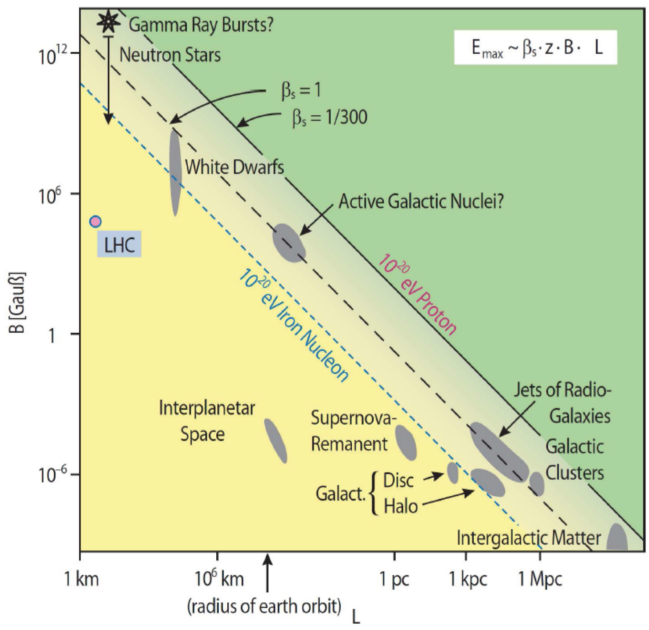

Figure 1.2: The combination of size (shown on the x-axis) and magnetic field intensity (on the y-axis) required to accelerate cosmic rays to an energy of 10^{20} eV [12]. See text for details.

Size of accelerating region

There is an upper limit to the energy to which particles can be accelerated by first-order mechanism [10]. This is related to the dimension of the accelerating region and to the Larmor radius defined in Eq. (1.6). The latter must be smaller than the former (L>2r_L). The theory uses this constraint and derives the maximum energy [11]:

$$(E_{15})_{max} \simeq 0.5 Z B_{\mu G} L \beta \tag{1.7}$$

L is the size of the accelerating region and β is again the shock speed in terms of light speed. This equation is usually represented with the so-called *Hillas plot*, shown in Fig. 1.2. All the lines indicate which are the magnetic field B and size values L required for accelerating a particle to 10^{20} eV. In particular, the solid and dotted black lines are referred to proton, for two different shock speeds: $\beta = 1$ and β=$\frac{1}{300}$ respectively. It is easy to visualise how for a relatively small shock speed, larger sizes and magnetic fields are required.
The dependence on the particle charge is highlighted comparing the black dotted line with the blue dotted one, which represents the acceleration conditions for iron. For a fixed energy, heavier nuclei are more efficiently confined, thus they experience a higher acceleration rate. This translates into less strict requirements for the magnetic field and the size of the source.
The Hillas plot shows also several astrophysical objects and plausible acceleration sites lie above the lines.

Fig. 1.2 does not take into account energy losses during acceleration process. These losses reduce our options for likely cosmic ray sources still further. In particular, ultra-relativistic particles, which spiralise around magnetic field lines, loose energy through

synchrotron process. On the other hand, in regions where the magnetic field is low, another loss mechanism may dominate, based on interactions with photons. These processes involves photons from any sources and from cosmic background radiation and they include pion-photo production and pair production. As it will be explained in Sec. 1.3, these reactions are also important during propagation.

1.2.2 Possible candidates for UHECR acceleration

Shock acceleration in supernovae can explain cosmic rays of energies up to 10^{15} eV [13] and, according to some unverified models, up to 10^{18} eV [14]. On the contrary, the origin of the UHECRs is debated and there are few plausible objects that can accelerate charged particles to the highest energies. Looking at Fig. 1.2, there are various candidate sources. Actually, additional limitations, due for example to energy losses, further restrict the maximum energies and, as a consequence, the allowed sites for UHECR acceleration. I report here a list with a more detailed description of the candidate sources.

- **Pulsars**. The acceleration of particles in pulsar environments has been suggested since their discovery. For what concerns observations, while nearby pulsars show direct evidence of accelerated electrons and positrons, the acceleration of hadrons is still unclear. However, it has been demonstrated that young magnetized neutron stars with surface magnetic fields of 10^{13} G can accelerate charged iron nuclei up to energies of 10^{20} eV [15]. The acceleration process is magnetohydrodynamic, rather than stochastic as it happens around astrophysical shocks. There are also models for UHECR acceleration at magnetars, neutron stars with surface magnetic fields up to 10^{15} G [16]. More recent studies show that fast spinning pulsars can explain the observed spectrum of UHECRs and the composition trend described by the Auger collaboration [17].

- **AGN**. Active Galactic Nuclei (AGN) are extragalactic sources with luminous active nuclei, powered by supermassive black holes. They have long been considered as candidate sources [1, 11]. Indeed, both the core region and the plasma ejecta, called *jets*, emerging from it should offer the right combination of sizes and magnetic fields. The jets have magnetic field of the order of a few Gauss, but dimension of the order of the parsec; these conditions lead in principle to a maximum proton energy of the order of 10^{19} eV. The core region can accelerate about up to the same energy, having relatively small sizes of a few 10^{-5} parsec, but higher magnetic fields of about 10^3 G. Actually, realistic calculations, which take into account the energy losses outlined in the previous section, lead to a maximum energy of only a small fraction of EeV [18], which can exclude them as candidate sources.
  There's also a particular class of AGNs, called *radio-loud* AGN, which exhibits a strong radio emission. In general, these objects do not have sufficiently fast shocks to keep the acceleration rate above the loss rate; but a small sub-class called *Fanaroff-Riley Class II* (FR-II) fulfills the requirements for accelerating particles up to 10^{20} eV. In particular UHECRs can be accelerated around special areas with intense magnetic fields: the so-called *hotspots*. Hotspots are regions with very strong radio emission. They are produced from powerful plasma shock waves, which are in turn generated by jets emitted from the cores of AGNs [19]. A typical example of this kind of sources is reported in Fig. 1.3.

- **Gamma-ray Bursts (GBRs)** GBRs are among the most energetic events in the universe. The first suggestions [20] that GBRs could be the sources of the UHECRs

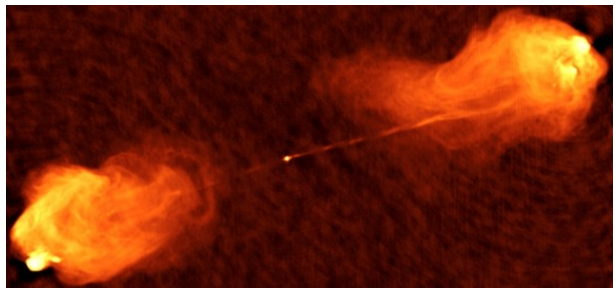

Figure 1.3: Cygnus-A is one of the brightest radio galaxy in the sky. This image clearly shows the strong radio emission from the lobe hotspots (image courtesy of NRAO/AUI).

were based on the directional coincidence between the two highest energy cosmic rays and the two most powerful GRB detected. Besides, the small size of the source and the time variability of the phenomena suggest that they produce shocks with a bulk Lorenz factor of a few hundreds. This condition is in principle sufficient to accelerate charged particles up to 10^{20} eV. The doubts about these candidates are due to their cosmological distance (about 100 Mpc). For such distant sources the *GZK effect* come into play, as I will explain in Sec. 1.3.1, thus reducing the possibility to explain the UHECRs flux from GBRs .

- **Colliding Galaxies**. A collision between two galaxies produce large scale shocks. In particular, a typical shock dimension of 30 kpc for the colliding galaxies and a shock magnetic field of 20 μG [21] provide the conditions for acceleration to above 10^{20} eV. These objects thus offer the suitable environment for UHECR acceleration.

- **Clusters of Galaxies**. These objects may have magnetic fields of order several μG and sizes of 500 kpc. Therefore, the acceleration to almost 10^{20} eV would be possible, but the large dimensions of these systems and the energy losses limit the maximum energy to about 10^{19} eV [22].

1.3 UHECR propagation

Another point which has to be addressed is the cosmic ray propagation from the sources to the observation point. Indeed, an UHECR will interact with photon fields and it will be deflected by intergalactic and/or galactic magnetic fields. These kinds of interactions will lead to a modification in the observed spectrum and to a change in the arrival direction of the UHECRs.

1.3.1 Interaction with Cosmic Microwave Background

During their travel across the space, UHECRs interact with the so-called *Cosmic Microwave Background* (CMB) radiation. This is the residual electromagnetic energy from the Big Bang. Its spectrum is described by the Planck black body function, with a characteristic temperature of 2.7 K and a density of 415 photons/cm^3. The mean photon energy is $E_0 = 6.4 \times 10^{-4}$ eV, placed in the microwave region of the spectrum.
This background radiation was discovered by Penzias and Wilson in 1964. Shortly after, Greisen [23] and independently Zatsepin and Kuz'min [24] predicted that the UHE

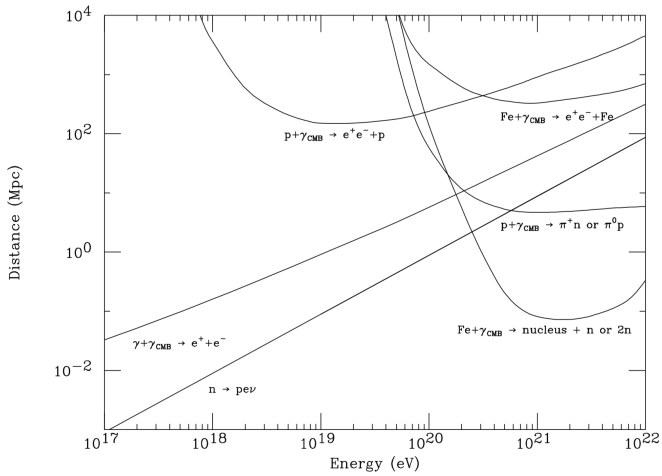

Figure 1.4: Summary of the possible interactions of UHECRs with the CMB [25]. Both the photo pion production for UHE protons and the photo-disintegration of UHE Fe nuclei lead to significative energy losses to which the observed cut-off of the spectrum could be related. See text for the details.

protons and the CMB radiation could interact via the photo-pion production, inducing a cut-off in the CR spectrum around $5{\times}10^{19}$ eV. This cut-off became known as *GZK cut-off* and it is common to refer to this process as the *GZK effect*.
Actually, the panorama of the possible interactions between cosmic rays and CMB is wider and it is reported in Fig. 1.4. The photo-pion production is represented by the following reactions:

$$p + \gamma_{CMB} \rightarrow \pi^+ + n \tag{1.8}$$

$$p + \gamma_{CMB} \rightarrow \pi^0 + p \tag{1.9}$$

In addition, UHECRs can interact with CMB photons producing electron-positron pairs:

$$p + \gamma_{CMB} \rightarrow e^+e^- + p \tag{1.10}$$

$$Fe + \gamma_{CMB} \rightarrow e^+e^- + Fe \tag{1.11}$$

Finally, another important interaction is the photo-disintegration, where one or two nucleons are chipped off the nucleus:

$$Fe + \gamma_{CMB} \rightarrow nucleus + n \text{ or } 2n \tag{1.12}$$

Fig. 1.4 shows also the mean free path for the interaction of a high-energy photon with the CMB: $\gamma + \gamma_{CMB} \rightarrow e^+e^-$. Added for reference is the mean decay length for a neutron indicated by $n \rightarrow pe\nu$. At 10^{20} eV a neutron decays into a proton with a decay length of the order of the Mpc.
The quoted interactions can happen because UHECRs have such large Lorentz factors that CMB photons have very high energies in the rest frame of cosmic rays. It is possible to derive the main physical quantities of these processes, using the relativistic kinematics. In the rest frame of cosmic ray, the CMB photon energy is:

$$E = E_0\gamma\left(1 + \frac{v}{c}\cos\theta\right) \tag{1.13}$$

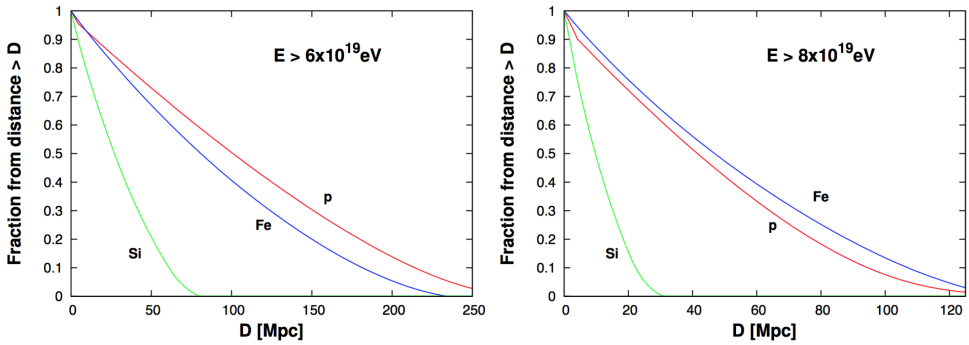

Figure 1.5: GZK horizons for protons and iron and silicon nuclei [26]. See text for details.

For the photo-pion production (Eq. (1.8) and (1.9)), the energy threshold, which is $E_{th} \simeq$ 200 MeV, corresponds to an energy for a proton E=2$\gamma m_p c^2$, in the limit $v \to c$, $cos\theta = 1$. Given that $\gamma = E_{th}/E_0$, a proton energy of about 10^{20} eV is obtained. When including the integration over the Planck spectrum of CMB radiation and over all angles, the threshold for the photo-pion production decreases to about $5{\times}10^{19}$ eV, well within the observed ultra-high energies of the cosmic rays.
This reaction produces a significative energy loss for the UHE proton, in particular it loses about 20% of its energy after each interaction and its energy will decrease by an order of magnitude after traversing 100 Mpc. Given the CMB density and the interaction cross-section, it is possible to derive the mean free path of a cosmic ray $\lambda = (n_\gamma \sigma_{\pi p})^{-1}$ as a function of the energy. Inspecting Fig. 1.4, it is clear that the mean free path of photo-pion production become rather short at the typical energies of the end of the UHECR spectrum: it is about 50 Mpc at 10^{20} eV and 5 Mpc at $3{\times}10^{20}$ eV. Looking at the problem from another point of view, this implies that it is possible to observe a proton with energy above 10^{20} eV ($3{\times}10^{20}$ eV) only if its source is within 50 Mpc (5 Mpc). This kind of distance limit is called *GZK horizon*. Fig. 1.4 shows also another possible interaction between proton and the CMB radiation, i.e. the pair production (Eq. (1.10)). This reaction has a lower energy threshold of about 1 MeV, which corresponds to a proton energy of about 10^{17} eV. Consequently, this process is more important for lower CR energies.
UHE photons as well as protons interact with CMB radiation, being quickly removed via the electron-pair production.
Finally, considering heavy nuclei, photo-disintegration reactions and pair production (Eq. (1.12) and (1.11)) are important. The threshold energy for photo-disintegration increases with the mass, so lighter components are more quickly disintegrated. For iron nuclei, it corresponds to an energy which is again about $5{\times}10^{19}$ eV. The energy loss associated with these processes leads to a cut-off. In addition, like for the other cited reactions, this can be associated to a limit on the distance from which a source can contribute significantly to the flux at Earth. Fig. 1.5 allows to better understand the dependence of this limit on the energy and CR mass [26]. In fact, it displays the GZK horizon for proton, iron and silicon nuclei, which are injected from uniformly distributed sources, located farther away than a distance D. Particles are assumed to be injected with an input spectrum of $\frac{dN}{dE} \propto E^{-\alpha}$. An attenuation factor is evaluated, given by the fraction of the events injected with energy above E_{th} which still remain with $E > E_{th}$ after traversing a distance D. Fig. 1.5 shows this attenuation factor, in particular the fraction of nuclei that

arrives at Earth with energy above 6×10^{19} eV (left panel) and 8×10^{19} eV (right panel) is reported. The GZK horizon is of comparable size for protons and iron nuclei, it is smaller for intermediate-mass nuclei. It decreases for higher energy thresholds. In other words, unless UHECRs originate from nearby sources (within a few tens Mpc), they must be mainly protons or heavy (A $\simeq$ 40) nuclei with very few intermediate nuclei.
Finally, it has to be mentioned that the propagation of UHE nuclei is affected also by the Extragalactic Background Light (EBL). This radiation was mostly emitted during star formation, plus a contribution from AGN; its spectrum exhibits one peak at about 8 meV (far IR) and one at about 1 eV (near IR, with a tail extending in the visible and UV). Nuclei heavier than protons interact with EBL by pair production and photo-disintegration.

1.3.2 Magnetic fields

One of the big difficulties for understanding UHECR propagation is related to the poor knowledge of galactic and especially extragalactic magnetic fields. Some measurements with galaxy clusters suggest that these fields are of the order of μG [27]. These measurements are carried out using Faraday rotation. Outside the cluster boundaries, it is difficult to measure field strengths, because of the intergalactic material lack. Often nG strengths are assumed for these regions, but they could be larger. For more details see [28] and [29]. This scenario is even more complicated because magnetic fields are expected to be turbulent. The propagation of cosmic rays in these fields can be described as a diffusion process. Assuming that the space is filled with cells of constant dimension with the same magnetic field strength B, but different field orientation, the diffusion theory predicts that the deviation angle with respect to the original direction has the form:

$$\Delta\phi = K\left(\frac{\mathrm{d}}{10\mathrm{Mpc}}\right)^{1/2}\left(\frac{L}{100\mathrm{kpc}}\right)^{1/2}\left(\frac{2\times10^{20}\mathrm{eV}}{E}\right)\left(\frac{B}{0.1\mu\mathrm{G}}\right) \tag{1.14}$$

where d is the distance to the source, E is the particle energy and L is the turbulence cell size. The deflection for a nucleus of charge Z would be a factor Z larger.
In order to have an idea of the deflections suffered by cosmic rays, Fig. 1.6 is reported from [25]. The four panels represent four different proton energies (1 EeV - 3 EeV - 10 EeV - 100 EeV): for each of them, 20 simulated trajectories are shown. These are projected on the XY plane and they are referred to protons which propagate for 40 Mpc in a constant magnetic field of 1 nG. Energy losses are neglected. It easy to visualise how the propagation of the protons passes from diffusive propagation at 1 EeV to rectilinear propagation at 100 EeV.
If instead the magnetic field were 100 nG, propagation at 100 EeV would be completely diffusive. For energies higher than 100 EeV the propagation would not be simply rectilinear. In fact the scenario would be complicated by the GZK effect, which quickly reduces the energies of cosmic rays. Considering iron nuclei and the same magnetic field of 1 nG, the rectilinear motion would be reached for energies higher than those shown in Fig. 1.6.
These examples reveal the complexity introduced in propagation of cosmic rays due to magnetic fields. It is interesting to mention that if UHECR were protons and if we knew magnetic fields very accurately, we would be able to point the sources that produce the cosmic rays, doing the so-called *UHECR astronomy*.

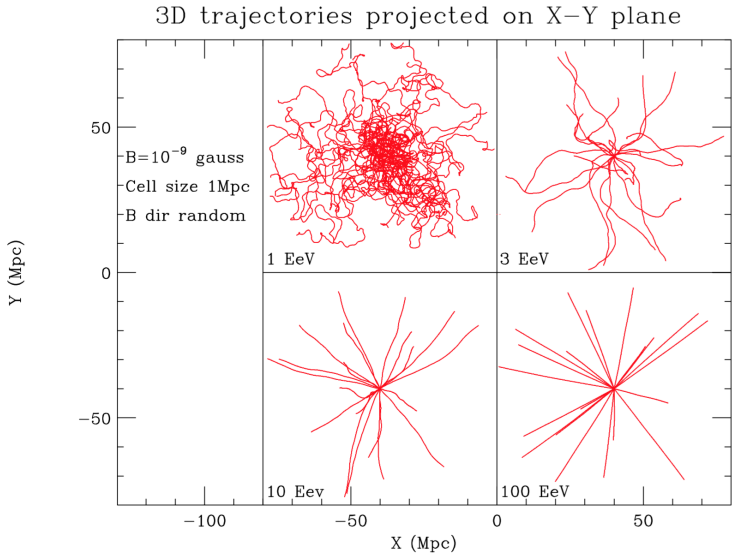

Figure 1.6: Projected view of 20 trajectories of proton primaries propagating from a point source for several energies and for a given magnetic field configuration [25]. Trajectories are plotted until they reach a physical distance from the source of 40 Mpc. See text for details.

CHAPTER 2

Detection of Ultra-High Energy Cosmic Rays

The decreasing flux of the cosmic ray energy spectrum has an immediate consequence on the detection techniques, as outlined in Sec. 1.1. Measurements are inefficient through satellites or balloon probes at E>10^{14} eV and large detection areas are needed. In addition, at these energies cosmic rays generate a sufficient number of particles on Earth's surface, so that the primary CR is observed indirectly, through the secondary products arriving on the ground.
Following these arguments, this chapter is divided in two sections. In the first one (Sec. 2.1) , I will focus on the final part of the UHECR travel, when it arrives on Earth. In particular, I will describe the phenomenon of the *Extensive Air Shower*, i.e. the cascade of secondary particles, generated by the UHECR interaction with the atmosphere.
In the second section (2.2), I will highlight the different techniques that have been developed for the detection of UHECRs. Particular attention is given to the ground array and fluorescence methods, which are both exploited at the Pierre Auger Observatory since the beginning of its operation.

2.1 Extensive Air Showers

The phenomenon of *Extensive Air Shower* (EAS) results from the interaction of the cosmic ray, called *primary particle*, with air molecules (mainly nitrogen, oxygen, and argon) at a typical height of 15 to 35 km. This interaction produces a cascade of many secondary particles, which arrive nearly-simultaneously over an extended area on ground. It was discovered by Bruno Rossi in 1934 and independently by K. Schmeiser and W. Bothe in 1938, who observed correlated arrivals of particles at widely separated points. In 1939, Pierre Auger estimated the energy of the primary particles initiating such showers as 10^{15} eV. To have an idea of the relevant quantities of an EAS, just consider an UHE proton at 10^{19} eV. It produces at sea level about 10^{10} secondary particles. These are mostly photons and electrons/positrons. Their energy is between 1 and 10 MeV and they carry about the 85% of the total energy. The remaining fraction of secondary particles consists of muons with an average energy of 1 GeV (transporting 10% of the total energy), pions with energy of a few GeV (4% of the total energy) and a smaller fraction of neutrinos and baryons. These secondary particles are spread over a few km^2. For increasing energy of the primary UHECR proton, more particles will be produced: at 10^{20} eV some 10^{11} particles are produced and they are spread over about 10 km^2 on ground.
The EAS phenomenon gives us the opportunity of investigating the nature of UHECRs and also it opens a window on the study of particle interactions at energies not reachable by man-made accelerators.
The basic processes involved in the development of an EAS are the nucleonic cascades

and the electromagnetic cascades. In order to infer the properties of the primary cosmic ray, it is necessary to compare the measuraments to detailed numerical simulations. Before the era of high-speed computing, Heitler [30] presented a very simple model of the electromagnetic cascade development, which allows to understand the basic physics involved. The method was also recently extended to hadronic showers [31]. In the following sections, the phenomenon of electromagnetic showers and the extension to the hadronic part will be summarised. In addition, some details about hadronic interaction models used for simulating EAS will be given.

2.1.1 Electromagnetic showers

Heitler's model describes cascades initiated by high energy electrons or γ-rays. When these particles enter the atmosphere, they undergo repeated two-body splittings, either one-photon bremsstrahlung or electron-positron pair production. In the ultra-relativistic limit, the radiation lengths λ_r for bremsstrahlung and pair production are the same. The probability that these processes take place is one-half at path length R and it is given by:

$$\exp(-R/\lambda_r) = \frac{1}{2} \qquad \text{or} \qquad R = \lambda_r \ln 2 \tag{2.1}$$

Therefore, if the cascade is initiated by a γ-ray of energy E_0, after an average distance of R an e^+e^- pair is produced. For simplicity, it is assumed that the pair shares the energy of the γ-ray, that is, $E_0/2$ each. In the next length R, the electron and positron lose about half of their energy and they each radiate a photon of energy $E_0/4$. Thus, after distance 2R we end up with two particles and two photons with energy $E_0/4$. As shown in Fig. 2.1 (panel a), this chain is repeated until the energy of photons and particles is degraded through the atmosphere. After distance nR, the number of photons, electrons and positrons is 2^n and their energy is $E_0/2^n$ on average. The shower will consist of about $\frac{2}{3}$ e^+e^- and $\frac{1}{3}$ photons. The cascade eventually reaches its maximum development when the particle energy falls below the critical energy E_c^γ, so that ionisation losses become dominant with respect to bremsstrahlung. From this point on, the number of particles in the shower does not change. Besides, with decreasing energy, the production cross-section for pairs decreases until it becomes comparable to Compton scattering and photoelectric absorption.
Two main shower observables can be defined: the number of particle at maximum shower development N_{max} and the corresponding column density (i.e. the slant depth $X = \int \rho(l)\mathrm{d}l$) at which this maximum is reached, X_{max}:

$$N_{max} = E_0/E_c^\gamma \qquad \text{and} \qquad X_{max} = X_0 + \lambda_r \ln(E_0/E_c^\gamma) \tag{2.2}$$

where X_0 is the depth of the first interaction. Even this very simplistic model reproduces two important features of air showers: the number of particles (called also shower *size*) at shower maximum N_{max} is proportional to E_0, and the depth of shower maximum X_{max} depends logarithmically on the primary energy E_0.
It is also possible to define the rate of change of the shower maximum depth as a function of the energy, i.e. the so-called *elongation rate*:

$$D_{10} \equiv \frac{\mathrm{d}X_{max}}{\mathrm{d}\log_{10}E_0} = \lambda_r \ln 10 \simeq 85 \text{ g/cm}^2 \tag{2.3}$$

In air, radiation length λ_r is 37 g/cm^2 and by using Eq. (2.2), one obtains that the depth of the maximum increases logarithmically with energy, at a rate of 85 g/cm^2 per energy decade.

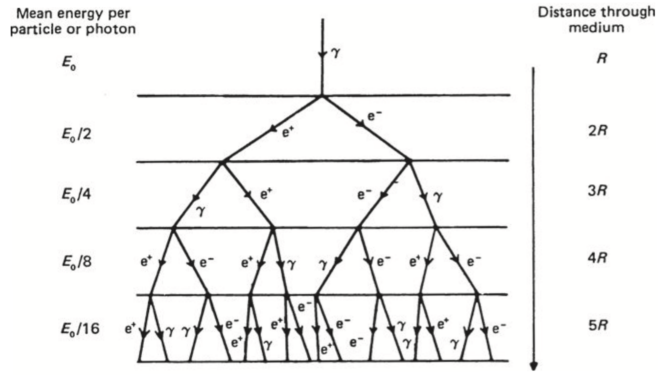

(a)

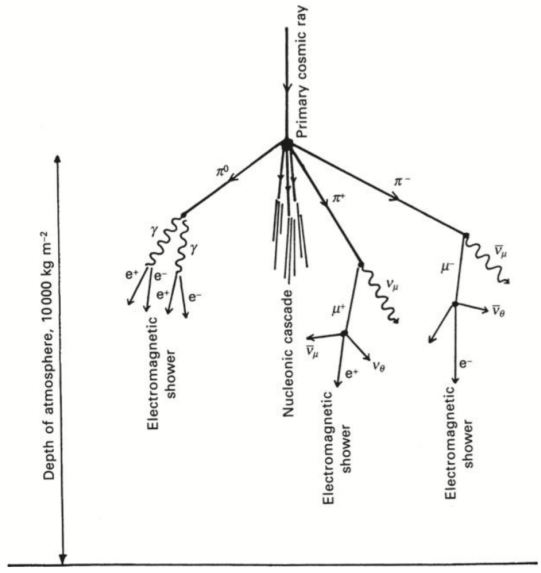

(b)

Figure 2.1: A schematic view for electromagnetic showers (panel a) and hadronic showers (panel b) in the atmosphere.

2.1.2 Hadronic showers

When high energy cosmic rays interact with atmospheric molecules, they initiate hadronic cascades, similar in some respects to the electromagnetic ones described in the previous section. The schematic evolution of a hadronic cascade is shown in Fig. 2.1 (panel b). The main features of such a process can be summarised as follows :

- The atmosphere is imagined in layers of fixed thickness $\lambda_I \ln 2$, where λ_I is now the interaction length of strongly interacting particles. For interactions in the energy range 10-1000 GeV, it is a fairly good approximation for λ_I to be constant. For pions in air, $\lambda_I \simeq 120$ g/cm^2 [32].
- The interacting primary cosmic ray produces a cascade of secondary particles belonging to three main components: the hadronic one (nucleons, mesons K and pions π^+, π^-, π^0), the muonic one (μ^+, μ^-) and the electromagnetic one (γ, e^+, e^-). The hadronic component is close to the shower axis.
- Hadrons interact after traversing one layer, producing N_{ch} charged pions and $\frac{1}{2}N_{ch}$ neutral pions. The secondary nucleons and charged pions which have sufficient energy continue to multiply through successive generations of nuclear interactions until the energy per nucleon drops below that required for pion production. 1/3 of the available energy goes into the electromagnetic component, while the remaining 2/3 goes into hadrons. In this simplified picture, the number of charged pions, i.e. the pion *multiplicity*, is energy independent.
- The neutral pions π_0 have short lifetimes, of the order of 10^{-16} s, therefore they decay immediately into two γ-rays, $\pi_0 \rightarrow 2\gamma$, each of which starts an electromagnetic cascade.
- Charged pions have a longer lifetime, of the order of 10^{-8} s. Many of them decay in flight into muons releasing muonic neutrinos and antineutrinos:

  $$\pi^+ \rightarrow \mu^+ + \nu_\mu$$
  $$\pi^- \rightarrow \mu^- + \bar{\nu}_\mu$$

  In turn, the low energy muons decay into positrons, electrons and muonic neutrinos:

  $$\mu^+ \rightarrow e^+ + \nu_e + \bar{\nu}_\mu$$
  $$\mu^- \rightarrow e^- + \bar{\nu}_e + \nu_\mu$$

  Muons are produced with very high energy and are highly penetrating. Because they have long radiation lengths, high energy muons are observed at the surface of Earth and they can be exploited to infer hadronic properties of the EAS.

To obtain the number of muons N_μ in the shower one simply assumes that all (charged) pions N_π decay into muons when they reach the critical energy E_c^π:

$$N_\mu = (2N_\pi)^{n_c} \tag{2.4}$$

where n_c is the number of steps needed for the pions to reach E_c^π. n_c can be calculated using the pion energy E_π:

$$E_\pi = \frac{E_0}{(\frac{3}{2}N_{ch})^n} \tag{2.5}$$

This expression stems from the assumption of equal energy sharing among the hadronic component and the electromagnetic one. E_0 is the initial cosmic ray energy, n is the number of interactions (or atmospheric layers), after which there are $N_\pi = (N_{ch})^n$ charged pions, carrying a total energy of $(2/3)^n E_0$. Thus, the number of interactions n_c needed for pions to reach the critical energy E_c^π, below which they will decay into muons, is:

$$n_c = \frac{\ln(E_0/E_c^\pi)}{\ln 3N_\pi} \tag{2.6}$$

Introducing $\beta = \ln 2N_\pi / \ln 3N_\pi$ we have:

$$N_\mu = (E_0/E_c^\pi)^\beta \tag{2.7}$$

Unlike the electron number, the muon number does not grow linearly with the primary energy but at a slower rate, depending on β. This value is related to the average pion number N_π and to the inelasticity, another parameter of hadronic interactions, neglected in this simplified model. Detailed simulations give values of β in the range 0.9 to 0.95 [33].
Another prediction of the extension of the Heitler model to hadronic showers is obtained by comparing Eq. (2.2) and Eq. (2.7):

$$\frac{N_{max}}{N_\mu} = \left(\frac{E_0}{E_c^\gamma}\right)^{1-\beta} \left(\frac{E_c^\pi}{E_c^\gamma}\right)^\beta \simeq O(1000) \text{ for } E_0 \simeq 10^{19} \text{ eV} \tag{2.8}$$

Eq. (2.8) means that an EAS contains a much larger number of electrons with respect to the number of muons. As a consequence the energy of the showers is carried essentially by the electromagnetic cascade.
The determination of the position of the shower maximum X_{max} and the elongation rate are more complicated, depending on the cross-sections, on multiplicity and on inelasticity of interactions, as it will be explained in Sec. 2.1.4. Using a proton-air cross section of 550 mb at 10^{18} eV and a rate of change of about 50 mb per decade of energy [34], one obtains a more realistic parametrisation of λ_I as a function of the energy:

$$\lambda_I \simeq 90 - 9\log(E_0/\text{EeV}) \text{ g/cm}^2 \tag{2.9}$$

Assuming, as in [31], that the first interaction initiates $2N_\pi$ (each π_0 produce two γ) electromagnetic cascades of energy $E_0/6N_\pi$ with $N_\pi \propto (E_0/\text{PeV})^{1/5}$ for the evolution of the first interaction multiplicity with energy, one can calculate the elongation rate:

$$D_{10}^p = \frac{\mathrm{d}X_{max}}{\mathrm{dlogE_0}} = \frac{\mathrm{d}(\lambda_I \ln 2 + \lambda_r \ln[E_0/(6N_\pi E^\gamma{}_c)])}{\mathrm{dlogE_0}} \tag{2.10}$$

or

$$D_{10}^p = \frac{4}{5} D_{10}^\gamma - 9\ln 2 \simeq 62 \text{ g/cm}^2 \tag{2.11}$$

D_{10}^γ is the electromagnetic elongation rate and Eq. (2.11) predicts that the electromagnetic elongation rate is larger than the hadronic one. This fact expresses the *Elongation Rate Theorem* [35], which pointed out that the elongation rate for electromagnetic showers is an upper limit to the elongation rate for hadronic showers.
A smaller elongation rate means a faster rate of energy transfer. This is a direct consequence of the larger hadronic multiplicity, which increases the rate of conversion of the primary energy into secondary particles. This result is in good agreement with simulations, but the assumptions we made lead to an underestimation of the absolute value of X_{max}. In fact, we have here considered only the first generation of photons, which, in the reality, is followed by additional showers from each subsequent interaction point.

2.1.3 The superposition model

The model described in the previous section can be extended to heavier primaries using the theoretical framework called *superposition model*. This provides a qualitative understanding of the basic features of EAS initiated by different nuclei. Note, however, that the superposition assumption is a simplification of the correct treatment of nucleus-nucleus interactions, which does not take into account the fact that in most collisions the number of interacting nucleons is not equal to that of the projectile. In particular, according to this model, the nuclear interaction of a nucleus with atomic number A is described as the superposition of the interactions of A nucleons of individual energy E_0/A. As a consequence, showers from heavy nuclei develop faster, which means that pions will reach their critical energy sooner and therefore increase the relative number of muons with respect to the electromagnetic component. The number of muons for a nucleus of mass A can be written as:

$$N_\mu^A = N_\mu^p A^{1-\beta} \tag{2.12}$$

where N_μ^p is the number of muons for a proton. This means that showers initiated by nuclei with atomic number A have a larger muon number.
For what concerns the maximum shower development, it is reached higher in the atmosphere for heavier primaries. The offset with respect to proton showers is simply :

$$X_{max}^A = X_{max}^p - \lambda_r \ln A \tag{2.13}$$

The elongation rate for nuclei of mass A is predicted to be the same of protons:

$$D_{10}^A = \frac{\mathrm{d}X_{max}^A}{\mathrm{dlog}_{10}E_0} = \frac{\mathrm{d}(X_{max}^p - \lambda_r A)}{\mathrm{dlog}E_0} = \frac{\mathrm{d}X_{max}^p}{\mathrm{dlog}_{10}E_0} = D_{10}^p \tag{2.14}$$

Finally, nuclei show smaller shower-to-shower fluctuations:

$$\sigma_A = \sigma_p/\sqrt{A} \tag{2.15}$$

where σ_A and σ_p are fluctuations of nuclei of mass A and of protons respectively. All these basic trends regarding the evolution of X_{max} and N_μ with energy and atomic number are reproduced by detailed MC simulations, even if, of course, there are differences in quantitative terms. Indeed, the superposition model does not take into account several effects, like for example re-interaction in the target nucleus or nuclear fragmentations. For this reason MC simulations of EAS are fundamental.

2.1.4 Monte Carlo simulations

The simplified arguments given in Sec. 2.1.2 and 2.1.3 are very useful for understanding the basic evolution of hadronic showers, but reality is much more complex and it can be better described using MC simulations. Those rely on phenomenological models based on experiments at accelerators and on Quantum Chromo Dynamics (QCD) theory. The key elements for describing an EAS can be summarised as follows:

- the inelastic cross-sections $\sigma_{\mathrm{inel}}^{p-air}$ of primary and secondary particles with air nuclei
- the average number of charged particles produced in an interaction, i.e. the so-called *multiplicity* N_{ch}

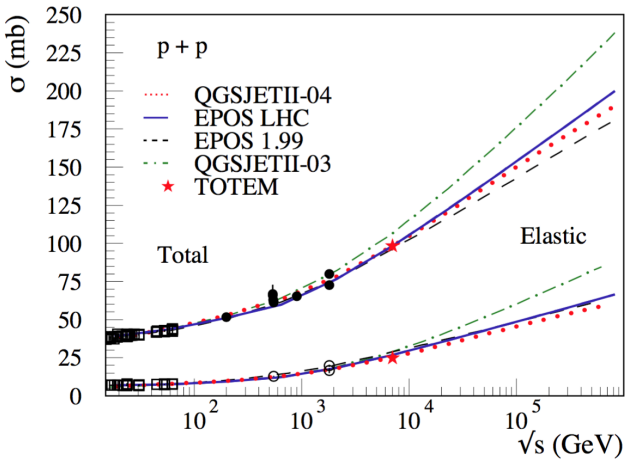

Figure 2.2: Total and elastic p-p cross section calculated with EPOS LHC (full line), QGSJetII-04 (dotted line), EPOS 1.99 (dashed line) and QGSJetII-03 (dashed-dotted line). The red stars are the measurement from the TOTEM experiment at LHC, black dots are earlier measurements done with different accelerators.

- the production ratio of neutral to charged particles
- the average fraction of energy transferred into secondary particles. This quantity is known with the term *inelasticity* $K_{\rm inel}$.

The determination of these parameters among others is of fundamental importance, because it has an impact on EAS properties. For example, an increase of the inelastic cross-section results in an earlier development of the cascade. This correlation between changes in the proton-air cross-section and the depth of the shower maximum X_{max} has been quantified [36]:

$$\frac{\Delta X_{max}}{X_{max}} \simeq -\frac{5}{7}\frac{\Delta\sigma_{\rm inel}^{p-air}}{\sigma_{\rm inel}^{p-air}} \tag{2.16}$$

Similarly, the relative change of X_{max} as function of the changes of multiplicity and inelasticity has been derived:

$$\frac{\Delta X_{max}}{X_{max}} \simeq -\frac{1}{2}\frac{\Delta N_{ch}}{N_{ch}} - \frac{1}{10}\frac{\Delta K_{\rm inel}}{K_{\rm inel}} \tag{2.17}$$

If inelasticity increases, the particles lose more energy, hence the shower reaches its maximum earlier in the atmosphere. A reduction of the multiplicity produces less particles in the first interactions. Due to energy conservation, they will be more energetic and the shower will develop more slowly, i.e. the maximum will be deeper in the atmosphere.
The take-home message is that a precise knowledge of UHE interactions is fundamental for a reliable prediction of the EAS properties, from which we have to infer information about the the primary cosmic ray. Different codes have been developed for EAS simulations: the most known are CORSIKA [37] and AIRES [38]. These codes can implement different hadronic interaction models. The most recent are EPOS-LHC [39] and QGSJetII-04 [40]. These models include the experimental data of LHC at 7 TeV and both

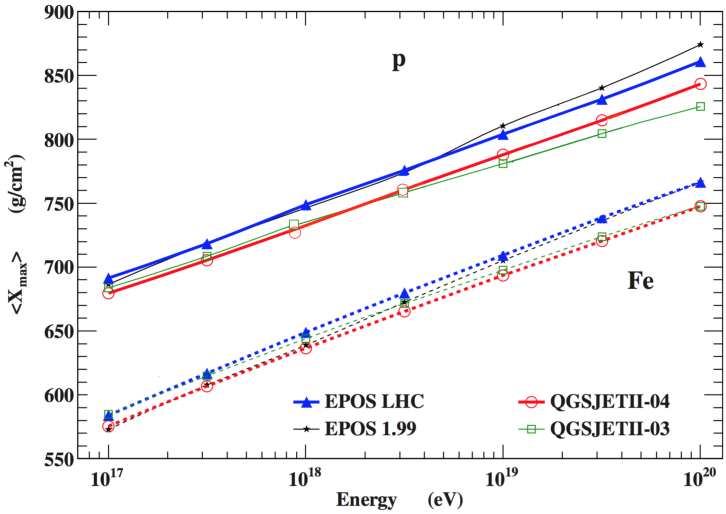

Figure 2.3: Average X_{max} for proton (solid lines) and iron (dotted lines) induced showers as a function of the primary energy for different high-energy hadronic interaction models [46].

are used in this work. They come respectively from the old versions EPOS 1.99 [41] and QGSJetII-03 [42]. It is worthy to mention another hadronic interaction model, Sybill2.1 [43], which has been found in good agreement with LHC measurements and which has been recently updated to Sibyll2.3 [44].
The main problem in simulating EAS is the lack of direct measurements for the ultra-high energy interactions. In fact, current experiments measure interactions at lower energies and between different nuclear species (UHECRs interact with atmosphere). This aspect is one of the largest sources of uncertainty for the UHECR study. Fig. 2.2 represents clearly the difficulty of this task. In particular, the figure shows the proton-proton total cross-section (related to proton-air cross-section) for different measurements, together with the extrapolations evaluated with different hadronic models. On the x-axis, there's the center-of-mass (cms) energy (for a proton at 10^{20} eV, the cms energy is about $0.4{\times}10^{15}$ eV). The red stars indicate the recent measurements by the TOTEM experiment [45] at LHC, on which the updated versions of the hadronic models EPOS-LHC and QGSJetII-04 are based. The black points are instead referred to earlier measurements done with different accelerators. The older versions of the models EPOS 1.99 and QGSJetII-03 were based on them. The cross-section is well described by all the models at low energy, where data exist. Then it diverges above 2 TeV cms energy. It is clear how with the new measurement the difference between the models is reduced by a factor of 5 (50 to 10 mb).
Fig. 2.3 reports X_{max} predictions from EAS simulation using EPOS-LHC and QGSJetII-04. The expectations are compared to former results using QGSJetII-03 and EPOS 1.99. In particular, X_{max} is shown for proton (solid lines) and iron (dotted lines) induced showers. Difference between the different hadronic interaction models are visible, but the updated versions EPOS-LHC and QGSJetII-04 exhibit the same elongation rate. On the contrary, EPOS 1.99 had an elongation rate larger than QGSJetII-03. This has an impact on the interpretation we can give about UHECR composition.
The number of muons arriving at ground N_μ, like X_{max}, is another quantity containing

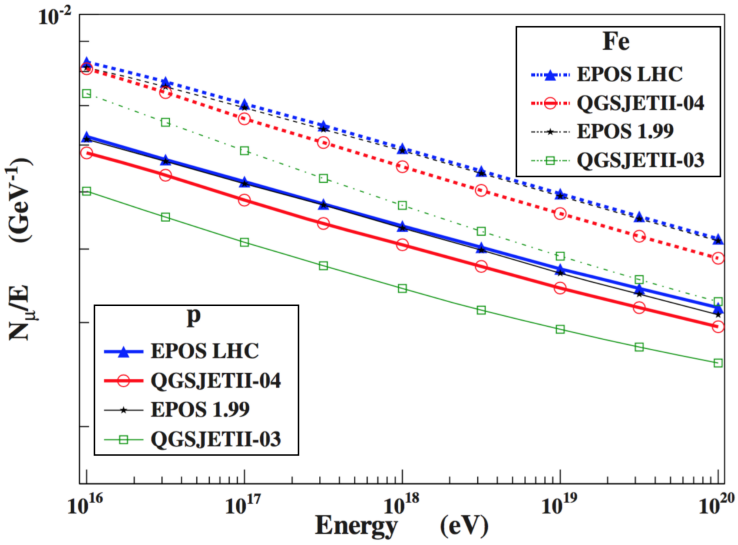

Figure 2.4: Mean number of muons at ground divided by the primary energy for proton (solid lines) and iron (dotted lines) showers at $40°$. Predictions are shown as a function of the primary energy for different hadronic interaction models [46].

information about the primary mass (see Eq. (2.12)). Results for air shower simulations with zenith angle of $40°$ are shown in Fig. 2.4. The difference between the new QGSJetII-04 and the old QGSJetII-03 is very large. QGSJetII-04 predicts about the same number of muons as EPOS 1.99 which is about 20% more than QGSJetII-03. The predictions of EPOS-LHC are instead very similar to EPOS 1.99. Even if the number of muons is much more similar for the two most recent hadronic models, there is still a difference of about 10%.
Furthermore, as it will be described in more details in Sec. 3.8 and Sec. 4.2.2, there is still a large discrepancy between the simulated number of muons and the observations. Recently the Pierre Auger Collaboration has found that the average hadronic shower is 1.33 ± 0.16 (1.61 ± 0.21) times larger than predicted using EPOS-LHC (QGSJetII-04), with a corresponding excess of muons [47]. This is still an open point on simulations of EAS.

2.2 Techniques of UHECR detection

As anticipated, for energies $E > 10^{14}$ eV the very low flux of cosmic rays makes impossible direct detection by satellites or balloon-borne experiment. For these energies, as described in Sec. 2.1, the enormous production of secondary particles triggered by cosmic rays in the atmosphere can be exploited for inferring physical properties of the primaries.
The detection of large extensive air showers typically falls into three categories: detection by arrays of particle detectors, detection of fluorescence light and detection of Cherenkov light. In addition, during the last decade new techniques have been developed, like the radio detection. All the developed techniques aim at deriving from the observables three main properties of the primary CR:

- energy

- mass
- arrival direction

In the following section, the various techniques will be described individually, although they can be combined to increase the performance of EAS detection. The Pierre Auger Observatory [48] and Telescope Array [49] are the modern examples of hybrid detection. The two experiments consist of both a surface detector array and a set of fluorescence detectors. The Pierre Auger Observatory will be described in details in the following chapter 3.

2.2.1 Ground array technique

A ground array samples the lateral profile of an EAS, i.e. the footprint generated at ground by air shower particles. It consists of a set of detectors whose extension, spacing and altitude is optimised depending on the CR energy that has to be measured. In particular, these characteristics can be summarised as follows.

- The area covered by a ground array is chosen depending on the rate of cosmic rays to be detected. A dimension of few thousands of m^2 is enough for the knee region around 10^{15} eV, while areas of thousands of km^2 are needed above 10^{18} eV.
- The spacing between the single detector elements depends on the dimension of the EAS that has to be measured (and therefore on the energy of the primary cosmic ray, as explained in the previous section). A spacing of about 1 km is sufficient at the UHECR energies, while a denser array is necessary going to lower energies. In other words, the spacing between detectors determines the accessible threshold energy.
- Finally, the altitude at which the array is located has to be chosen depending on the energy of the cosmic rays. In fact, the more energetic is the cosmic ray, the more it will develop deeper in the atmosphere, i.e. at lower altitudes. The detection of an EAS near its maximum allows a better reconstruction, since the number of secondary particles is larger and the fluctuations smaller. Following these arguments, altitudes around 1400 m are sufficient for the ultra-high energies, while for lower energies the array should be located at higher altitudes.

Fig. 2.5 (panel a) shows a sketch of a ground array. The single detector elements are typically scintillators or water Cherenkov detectors. The historical examples for the two types are respectively given by Volcano Ranch (the first event in the 10^{20} eV range was detected with this array [50]) and Haverah Park [51]. Another ground array experiment was AGASA (Akeno Giant Air-Shower Array) [52], which in the 90's was the biggest air shower detector: it consisted of 111 scintillator counters located on 100 km^2. Smaller arrays, exploring a lower energy region, are, among others, the EAS-TOP detector [53], active from 1989 to 2000 and the more recent KASCADE [54] and KASCADE-Grande [55] experiments. A scintillator array is usually made of few m^2 flat pieces of plastic scintillators laid on the ground. Instead, water Cherenkov detectors are tanks filled with extra pure water, which requires excellent protection against contamination.
An important difference between the two kinds of detectors is related to the acceptance of particles: it decreases with the zenith angle for the flat scintillators, while because of the Cherenkov tank height, this type of detectors offers a non zero effective surface for horizontal showers.

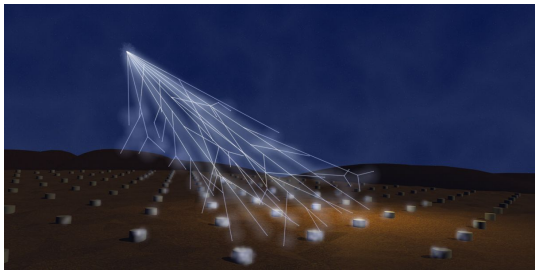

(a)

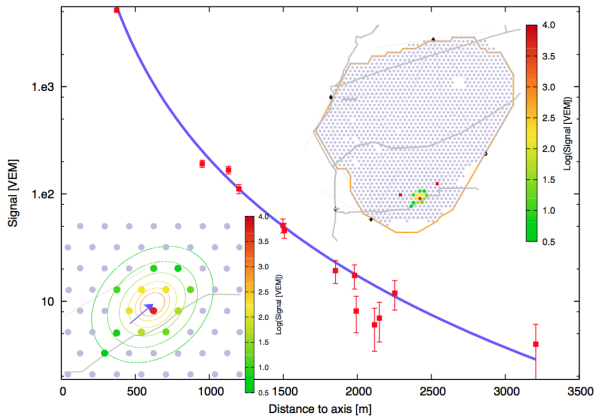

(b)

Figure 2.5: (Panel a) Sketch of detection of an EAS by a ground array. (Panel b) Example of detection using a surface array taken from the Auger collaboration public event display (**http://auger.colostate.edu/ED/**). The upper small panel displays the surface array of the Pierre Auger Observatory. The lower panel shows the footprint of an air shower with the estimated contours of particle density level and with the LDF. Red points are the measured densities as a function of the distance from the shower core.

The reconstruction of the arrival direction and the energy of the cosmic ray is based on timing and on the signal density distribution. The shower axis, and therefore the direction of the primary cosmic ray, is reconstructed using the arrival times of the shower particles in the detectors. Precision of 1° to 3° is usually achieved, because of the large base line of the detector spacing. In order to reconstruct the primary energy, the so-called *lateral distribution function* (LDF) is evaluated: signal densities are studied as a function of the lateral distance of the detectors to the shower axis. In particular, an energy estimator is the signal at an optimal core distance r_{opt}, almost completely determined by the array geometry, at which LDF fluctuations are minimal. In Fig. 2.5 (panel b) a typical footprint of an air shower on ground together with its LDF is shown. It is taken from the Auger Collaboration public event display. The reconstruction method exploited by this experiment will be described more in detail in Chapter 3.
For what concerns UHECR composition measurements, ground arrays do not have direct access to the position of the shower maximum and this is a strong limitation for the primary identification with this technique. The Pierre Auger Collaboration has developed various alternative methods for measuring mass with the Surface Detector and they will be described in detail in Chapter 4. Among them, there's the Muon Production Depth reconstruction, which is the topic of this thesis.

2.2.2 Fluorescence light technique

Unlike the ground array, the fluorescence light detector measures the longitudinal development of an EAS, looking at the fluorescence emission produced by the passage of the cosmic ray in the atmosphere. This technique is sketched in Fig. 2.6.
Among the first to realise that atmospheric nitrogen fluorescence light could be used to detect EAS were Chudakov in Soviet Union [56] and Tanahashi in Japan [57] during the 1960s. This approach depends on observing the faint fluorescence radiation (300-400 nm) which is emitted isotropically when the 2P and 1N band spectra associated with molecular nitrogen are excited by ionising particles. The first successful demonstration of the technique was performed by the Utah group in 1976 and led to the realisation of the Fly's Eye experiment. It was the first fully functional detector and it took data from 1981 until 1993. It measured the highest energy CR particle ever detected at 320 ± 90 EeV [58], dubbed the *"Oh-My-God particle"*. It was then upgraded to the High resolution Fly's Eye, briefly HiRes, that was operational from 1993 to 2006 [59].
The isotropic photon emission allows detectors to view showers from the side and at large distances. Fluorescence radiation reaches the telescopes following a straight line from the production point (see Fig. 2.6). Thus, the measured image maps the shower longitudinal development (shower size vs. atmospheric depth). For an accurate reconstruction of the shower geometry, a single telescope is not usually enough. Additional information by another fluorescence telescope (the so-called *stereo observation*) or by a ground array (the so-called *hybrid reconstruction*) is required.
A fundamental aspect of this kind of detection is that it is affected by various electromagnetic backgrounds, being the fluorescence light very faint. The main one derives from the moon light. Therefore, a fluorescence telescope operates only during dark nights. This greatly reduces the duty cycle of the detector. On the other hand, the energy and the composition of the UHECR can be estimated more precisely with respect to the ground array detectors. In particular, a calorimetric estimation of the primary energy is done by measuring the shower deposit profile in the atmosphere. In addition, the maximum of this profile gives a direct information about the mass of the primary particle. The reconstruction methods of these quantities will be described in Chapter 3, taking the Pierre

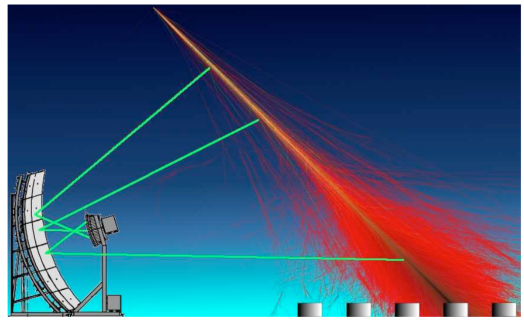

Figure 2.6: A sketch of the fluorescence detection technique. The fluorescence light by an air shower is collected by the telescope large mirror and focused onto a camera. In the sketch a few ground detectors are depicted. This picture helps in figuring out how the the two kinds of detection techniques map the lateral and longitudinal part of a shower.

Auger Observatory as reference.

2.2.3 Cherenkov light technique

Like the fluorescence light, the Cherenkov light emission from the charged component of an air shower provides an integrated measurement of the longitudinal development. The Cherenkov light technique was pioneered by the Chudakov's experiments, which were carried out in the Pamirs Mountains [60]. Modern experiments usually include many detectors of Cherenkov light distributed over a large area and can be associated to standard particle detector arrays. The largest Cherenkov array was composed by 150 photomultipliers distributed every $\simeq$ 40 m and was installed on the Fly's Eye site together with the CASA and CASA-MIA detector array [61]. More recent examples of Cherenkov detection are given by TUNKA [62] and Yakutsk [63].
From air shower simulations, it was shown that the density of Cherenkov light is proportional to the primary energy but essentially independent of its nature, at distances larger than about 150 m from the shower core. Instead the light profile close to the core is sensitive to the atmospheric depth of the shower, which correlates with primary cross section [64]. This makes this technique inappropriate to study EAS beyond 10^{17} eV, together with the low duty cycle of the detector. Cherenkov light is used in high energy gamma-astronomy and in this case it is collected by large-area mirrors. Typical examples of this kind of telescopes are given by MAGIC [65], VERITAS [66], H.E.S.S. [67] and the forthcoming CTA [68].

2.2.4 Radio technique

The first detection of pulsed radio emission produced by air showers was made in 1965 [69], but technical limitations did not allow further progress. It is a decade ago that the field was revived with the application of powerful digital signal processing techniques. Radio emission can be interpreted as a coherent superposition of geomagnetic emission, Askaryan charge-excess radiation and Cherenkov-like coherence effects arising in the density gradient of the atmosphere. Air shower radio signals carry information on both the energy and the mass of the primary particle. LOPES [70] and CODALEMA [71] are experiments measuring in the frequency range between the AM band at $\simeq$ 20 MHz and the FM band at $\simeq$ 80 MHz. Both experiments have access to energies of up to about 10^{18}

eV. Another important example of EAS radio detection is the Auger Engineering Radio Array (AERA) [72], aiming at energies > 10^{19} eV, the Tunka radio extension (Tunka-Rex) [73] and the Low Frequency Array (LOFAR) [74].

2.2.5 Current UHECR experiments

It is worth to report briefly which are the current experiments of UHECRs. One of them is the Yakutsk array [63], already mentioned in Sec. 2.2.3. It is located in the Lena river valley (Siberia, Russia), about 100 m above sea level. It has been taking data continuously since 1974, with a configuration that has been changed several times. It covered an area of about 17 km^2 in 1990, while now it is reduced to about 10 km^2. It consists of several different types of surface detectors.
The Telescope Array (TA) [49] located in Millard County, Utah, US, about 1400 m above sea level, started to collect data in March 2008. It is composed by 507 plastic scintillator detectors in a square grid with 1.2 km spacing and it covers an area of 700 km^2. This is viewed by 38 fluorescence telescopes placed in three stations. Each station has 12-14 telescopes viewing the range from 3 to 33 degrees in elevation.
The Pierre Auger Observatory is the largest experimental set-up devoted to the study of UHECRs. It is located in western Argentina and it comprises 1660 water Cherenkov detectors spread over a 3000 km^2 area, operating since 2004 together with 27 fluorescence telescopes.

CHAPTER 3

The Pierre Auger Observatory

The Pierre Auger Observatory is the world's largest experiment in Ultra-High Energy Cosmic Ray field. With its 13 years of data taken, it has reached a total exposure exceeding 50000 km^2 sr yr, together with the wide range of sky observed (in declination from -90° to 45°).
In the following chapter, the structure of the experiment will be described. After some introductory remarks (Sec. 3.1 and 3.2), I will focus on the characteristics of the main components of the observatory: in particular, the Surface Detector (Sec. 3.3) and the Fluorescence Detector (Sec. 3.4). In addition, the reconstruction techniques will be illustrated, which are generally performed exploiting a dedicate software called Offline[75]. In the last part of this chapter (Sec. 3.8), the main scientific results will be discussed.

3.1 Some historical remarks

In August 1991, the Pierre Auger Observatory was conceived by Jim Cronin of the University of Chicago and Alan Watson of the University of Leeds. Its main goal was to measure the properties of the UHECRs with unprecedented statistical precision, in order to derive information on the existence or absence of a flux suppression at the ultra-high energies. Controversial results were in fact obtained by the largest observatories at that time, AGASA and HiRes. In particular, the GZK cut-off was expected, but the AGASA experiment had not observed it [76]. Cronin and Watson decided to try to form a collaboration to build a detector of 5000 km^2, initially without fluorescence devices. An international workshop, held in Paris in 1992, opened a number of focused studies. During 1995, the discussion culminated in a 6-month Design Study hosted at the Fermi National Accelerator Laboratory by the then director, John Peoples. Two sites of 3000 km^2 on each hemisphere were proposed after the design study. Later on, this was not approved by the US funding agencies who would only support a Southern site. In November 1995 there was a democratic vote for the site position at the UNESCO headquarter in Paris. Argentina was designated for the purpose. In 2001 the construction of the engineering array started in Malargüe. January 1st 2004 physics data taking began with about 150 water-Cherenkov tanks and 6 fluorescence telescopes. The construction of the observatory finished in mid-2008 with a total number of 1600 tanks and 24 fluorescence telescopes. The first physics results were presented during the 2005 summer conference season. Many other important results have now been published by the Auger Collaboration that have had a major impact on the field of cosmic ray physics.

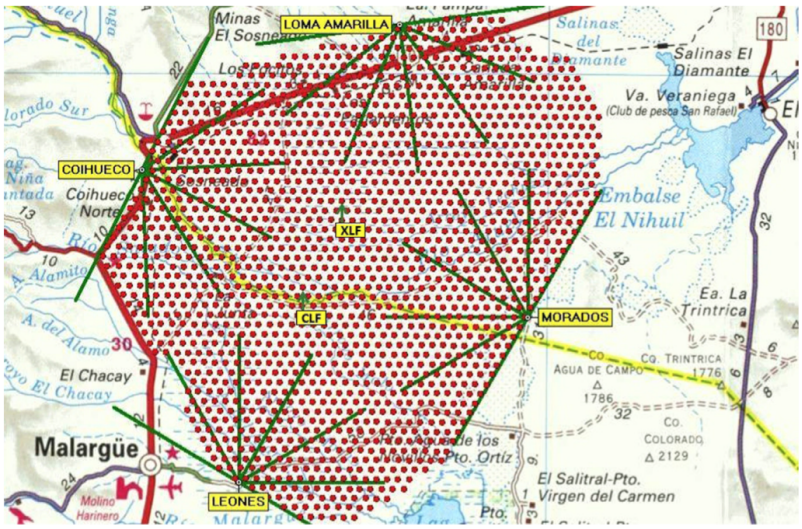

Figure 3.1: A map of the Pierre Auger Observatory. Each red dot corresponds to one of the 1660 surface detector stations. The four fluorescence detector enclosures are shown. The two laser facilities, CLF and XLF, near the Observatory center, are also shown.

3.2 Overwiew

The Pierre Auger Observatory is located near the Malargüe town, in the province of Mendoza, between latitudes 35.0° and 35.3°S and between longitudes 69.0° and 69.4°W. This area is generally flat, with detectors placed at altitudes between 1340 m and 1610 m. The mean altitude of the observatory is 1400 m, corresponding to an atmospheric overburden of $\simeq 875$ g/cm^2.
The Auger Observatory is a hybrid detector, since it is a combination of a Surface Detector (SD) and a Fluorescence Detector (FD). The SD is spread over an area of 3000 km^2 and it is composed by a ground array of 1600 water Cherenkov stations placed in triangular grids, with nearest neighbors separated by 1500 m. The FD consists of four air fluorescence sites on the perimeter of the array, each with six telescopes, for a total of 24 telescopes. In Fig. 3.1 the ground array together with the four fluorescence detector enclosures is depicted. Figure 3.2 shows examples of FD (top panel) and SD (bottom panel) detector elements.
The Cherenkov stations of SD record the charged particles from air showers striking the ground. Making use of well-established methods, it is possible to determine arrival directions and estimate the primary energy. Above 3×10^{18} eV, the detection efficiency is 100%, independently of the mass of the primary particle that initiated the shower. The quality of the measurements improves with the shower energy. The SD operates 24 hours per day and thus provides uniform coverage in right ascension.
The FD instead can operate only during moonless nights with good weather conditions, so that the duty cycle is much smaller than that of SD, i.e. about 15%. During dark nights, it detects the nitrogen fluorescence light produced by the passage of the air shower in the atmosphere. Since fluorescence light is proportional to the energy deposit in the atmosphere, as described in Sec. (2.2.2), the technique provides a nearly calorimetric method for determining the primary cosmic ray energy. The other fundamental observable is the

Figure 3.2: The fluorescence detector enclosure Los Leones (top panel) and a surface detector station (bottom panel).

depth at which a shower reaches its maximum size, which can be accessed in the most direct way. The FD provides also valuable cross-checks with SD measurements. As can be easily understood, the essential feature of the Auger hybrid design is the capability of observing air showers simultaneously by two different but complementary techniques, with very different systematic uncertainties.
After completing the Observatory, two enhancements have been incorporated into the baseline detectors that significantly increase the scientific potential. The HEAT fluorescence detectors and a 750 m array of 60 Surface Detector stations, called Infill Array, extend the sensitivity down to 10^{17} eV.

3.3 The Surface Detector

As anticipated, the SD consists of many stations placed over a very wide area of about 3000 km^2. The spacing between the detector stations is the result of a compromise between cost considerations and the energy threshold. In order to have full efficiency for events above $\simeq 3\times10^{18}$ eV, a maximum spacing of 1500 m is allowed. Other evaluations played also an important role in the choice: firstly the need for sufficient sampling of the particle density away from the shower core and secondly the need for shower front timing in several locations. At the spacing of 1500 m, approximately 10 stations are triggered by a nearly vertical shower with an energy of 10^{20} eV. For inclined events ($\theta \gtrsim 60^\circ$) the number of triggered stations is higher, more than 20.
Fig. 3.3 shows a schematic view of the components of a single SD station. It consists of a tank, of diameter 3.6 m and height 1.2 m, containing a sealed liner with a reflective inner surface. The liner contains 12,000 liters of ultra-pure water. Cherenkov light produced by the passage of charged relativistic particles through the water is collected by three nine-inch-diameter Photonis XP1805/D1 photomultiplier tubes (PMTs). These are symmetrically distributed at a distance of 1.20 m from the center of the tank and look downwards through windows of clear polyethylene into the water. The signal registered by the PMTs, both in the anode and last dynode, are digitised using FADCs, with a sampling rate of 40 MHz. Each SD station contains a GPS receiver with its corresponding antenna mounted at the top. This transmits signals to the closest FD site, where a communication tower sends the data to the CDAS (Central Data Acquisition System). Signals are previously calibrated locally and then selected by a hierarchical trigger system. Each station is autonomous, in fact a solar power system provides an average of 10 W for the PMTs and electronics. Electronics consist of a processor, GPS receiver, radio transceiver and power controller. More details about calibration, trigger and reconstruction are given in the following subsections. A more detailed description of the SD system can be found in [77].

SD Calibration

The Cherenkov light recorded by SD stations is measured in units of the signal produced by a muon traversing vertically the tank. This unit is named *Vertical Equivalent Muon* (VEM). The conversion to units of VEM is done both to provide a common reference level between tanks and to calibrate against the detector simulations for other Monte Carlo-based studies. Therefore, the goal of the SD calibration is to measure the value of 1 VEM in term of integrated FADC channels. In particular, two quantities are used for this scope: Q^{peak}_{VEM} and I^{peak}_{VEM}, which are respectively the peaks of the charge deposit and the pulse height distributions. The calibration procedure follows three main steps:

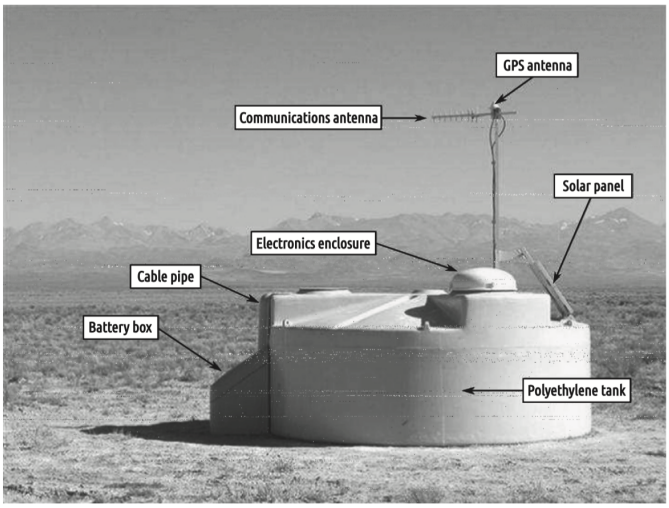

Figure 3.3: View of a single SD station. Its main components are indicated.

1. Set up the end-to-end gains of each of the three PMTs to have I_{VEM}^{peak} at 50 channels. This choice results in a mean gain of $\simeq 3.4\times10^5$ for a mean of 94 photoelectrons.

2. Adjust the electronics level trigger by continually performing a local calibration to determine I_{VEM}^{peak} in channels.

3. Determine the value of Q_{VEM}^{peak} to high accuracy using charge histograms, and use the known conversion from Q_{VEM}^{peak} to 1.0 VEM to obtain a conversion from the integrated signal of the PMT to VEM units.

The SD can not select vertical muons, but dedicated measurements using scintillators above and below test tanks to select vertical muons proved that Q_{VEM}^{peak} and I_{VEM}^{peak} for omni-directional atmospheric muons are proportional to the values for a vertical through-going muon [78].

SD trigger

The SD trigger has a hierarchic structure. The local trigger at each SD station level has two levels of selection. The first-level (T1) is realised if one of the two conditions is verified: a simple threshold trigger (TH) requiring 3-fold coincidence of $1.75I_{VEM}^{peak}$ on each PMT or a Time-over-Threshold (ToT), i.e. 13 time bins (one bin of FADC corresponds to 25 ns) at $0.2I_{VEM}^{peak}$ within a 3 μs window in coincidence for two out of the three PMTs. The total rate is $\simeq$100 Hz, dominated by the TH (100 Hz) over the ToT ($\simeq$ 1-2 Hz). At this level the local station is "passive".
The second-level trigger (T2) occurs again locally. This trigger condition requires either the station satisfies the ToT condition (i.e., the T1 as a ToT is always promoted to T2), or a 3-fold coincidence of $3.2I_{VEM}^{peak}$. The total rate is $\simeq$ 20 Hz, dominated again by the TH mode. At this level the station is "active", that is, it can contribute to form the central trigger.
The third-level (T3) central trigger is generated either by SD alone, or by an external

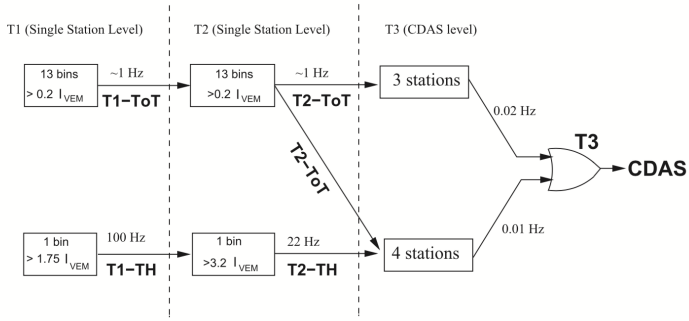

Figure 3.4: Schematics of the hierarchy of the trigger system of the Auger surface detector.

trigger, coming from the FD. This trigger can have two different configurations: a 3-fold coincidence of T2 stations having passed the ToT and a 4-fold coincidence of any T2 stations, provided that they satisfy defined geometrical and timing criteria. A schematic picture of the trigger system can be seen in Fig. 3.4. In June 2013, the Observatory installed across the entire array two additional SD T1 triggers: time-over-threshold-deconvolved (ToTd) trigger and the multiplicity-of-positive-steps trigger (MoPS). These triggers are based the ToT trigger, applying more sophisticated analysis to the FADC traces. A detailed description of the trigger system can be found in [79].
There are also other independent trigger functions, in addition to the local trigger: the scaler trigger and the calibration trigger. The scaler trigger records pulses with a very low threshold for auxiliary physics purposes such as space weather. The calibration trigger collects low threshold pulses using a small number of bins (20), which is one bin above $0.1 I_{VEM}^{peak}$, thus providing high rate cosmic ray data. These data are used to build calibration histograms and are also used to convert offline the FADC traces into VEM units. There are further trigger levels, T4 and T5, which are however applied offline to recorded data in order to select physics events (see next section).

SD event reconstruction

The first step for the reconstruction is selecting data of good quality. For this purpose, there are two additional offline requests. The "physics trigger", called T4, is needed to select real showers from the set of stored T3 data, that also contain background signals from low energy air showers. T4 trigger is mainly based on a coincidence between adjacent detector stations within the propagation time of the shower front. It is required that one of the following two conditions is verified: the first condition is the so-called 3ToT, which consists in the presence of 3 nearby ToT stations in a triangular pattern. The second condition is the 4C1 with 4 nearby stations required and no specific T2 trigger request. In selected events, random stations are identified by their time incompatibility with the estimated shower front. To guarantee the selection of well-contained events, a fiducial cut, called 6T5 trigger, can be applied, so that only events in which the station with the highest signal is surrounded by all 6 operating neighbors (i.e. a working hexagon) are accepted. In addition, for a correct event selection, malfunctioning stations, accidental timing stations or phenomena like lightnings must be excluded. Lightnings are seen in a station as a series of oscillations in the FADC traces of all three PMTs. In particular, if the total SD station signal is below 1000 FADC counts and becomes 0 (after

baseline removal) more than tree times, it is considered as originating from a lightning and the station is removed. Finally, to reject accidental stations, a criterion based on time compatibility is used.
Once the selection criteria have been applied, the reconstruction can be performed. For this purpose a dedicated software, called Offline, is used [75]. It is a framework divided in various modules, containing all the tools required for the event simulation and reconstruction.
The SD measures several UHECR characteristics: the arrival direction (zenith θ and azimuth angle ϕ), the position of the impact on the array (core) and the energy. The reconstruction of these quantities is performed following different steps.

- The timings of SD signals can be approximated as those expected if the shower started expanding spherically at the speed of light at time t_0 from a point $\vec{x}_{sh}$, which represents the shower origin:

$$c(t_i - t_0) = |\vec{x}_{sh} - \vec{x}_i| \tag{3.1}$$

  This is a 4-parameter function, where $\vec{x}_i$ and t_i are ground positions and signal start times of the stations (see Fig. 3.5). Using this 4-parameter fit, the radius of curvature of the shower front is determined from the time at which the core of the shower is inferred to hit the ground.

- The position of the core, $\vec{x}_{gr}$, is obtained from a maximum likelihood fit of the *Lateral Distribution Function* (LDF) of the signals in SD stations. Fig. 3.6 shows an example of an EAS footprint on the array (panel a) and its corresponding LDF (panel b), for a cosmic ray with energy 104±11 EeV and zenith angle (25.1±0.1)°.
  The LDF is fitted to a modified Nishimura-Kamata-Greisen function [80, 81]:

$$S(r) = S(r_{opt}) \left(\frac{r}{r_{opt}}\right)^{\beta} \left(\frac{r + 700\text{m}}{r_{opt} + 700\text{m}}\right)^{\beta+\gamma} \tag{3.2}$$

  r_{opt} is an optimal distance, being the distance at which the sum of shower-to-shower fluctuations and statistical fluctuations is minimum [82]. It depends on the energy range and on the array spacing. For the Pierre Auger SD, r_{opt} is 1000 m [83]. S(1000) is an estimator of the shower size. The exponent β is adjusted to the data and it depends on the zenith angle and on the shower size. The exponent γ is very close to 0.
  The reconstruction accuracy of S(1000) and $\sigma_{\mathrm{S}(1000)}$ has different contributions: a statistical one and a systematic error for the assumptions on the shape of the lateral distribution function; an additional contribution to the uncertainty is due to shower-to- shower fluctuations. The last term contributes a factor of about 10%, while the contribution of the first two terms depends on the energy and varies from 20% (at low energies) to 6% (at the highest energies).

- Shower axis $\hat{a}$ is obtained from the virtual shower origin (of the geometrical reconstruction) and the core (from the LDF reconstruction):

$$\hat{a} = \frac{\vec{x}_{sh} - \vec{x}_{gr}}{|\vec{x}_{sh} - \vec{x}_{gr}|} \tag{3.3}$$

  The angular resolution achieved after the reconstruction procedure is better than 1.61°, for events with more than three stations, and better than 0.91° for events

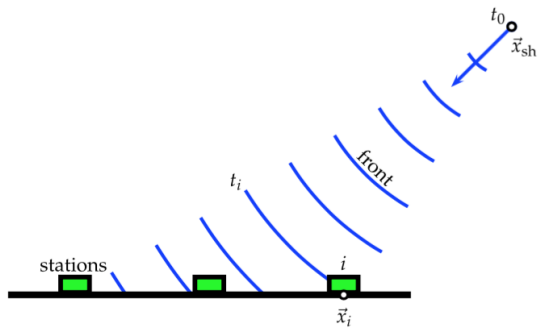

(a)

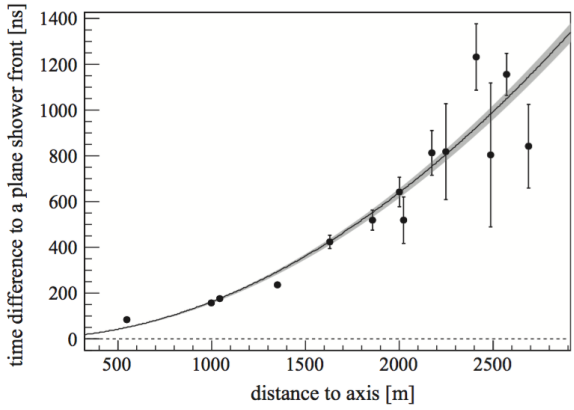

(b)

Figure 3.5: (Panel a) Schematic representation of the evolution of the shower front. (Panel b) Dependence of signal start times (relative to the timing of a plane shower front) on perpendicular distance to the shower axis. The shaded line is the resulting fit of the evolution model and its uncertainty.

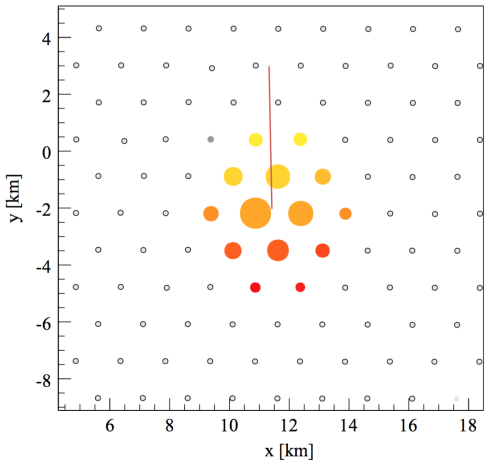

(a)

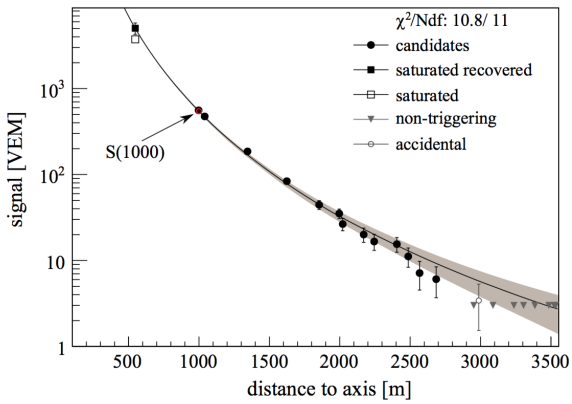

(b)

Figure 3.6: (Panel a) Air shower SD footprint for a cosmic ray of energy 104±11 EeV and zenith angle (25.1±0.1)°. The line represents the shower arrival direction, the size of the circles is proportional to the logarithm of the signal and the scale of color means the arrival time of the shower front from early (yellow) to late (red). (Panel b) Lateral distribution function for the same event.

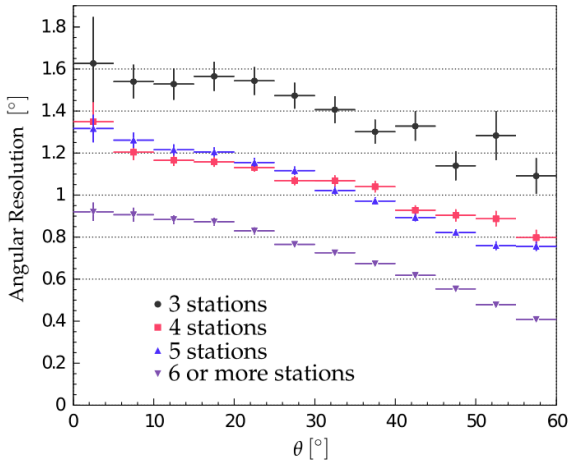

Figure 3.7: Angular resolution for different station multiplicities as a function of the zenith angle θ for events with energies above 3 EeV [86].

with more than six stations (see Fig. 3.7). The angular resolution is obtained taking into account the size of the total signal and the time evolution of the signal trace. A single station time variance is modeled for this purpose [84].

- The primary energy can be obtained by S(1000). For a given energy, the value of S(1000) decreases with the zenith angle due to the attenuation of the shower particles and geometrical effects. For this reason, S(1000) is corrected using the attenuation curve extracted from the *Costant Intensity Cut* (CIC) method [85]. The median angle, θ=38°, is taken as a reference point and it is used for the conversion of S(1000) to $S_{38} \equiv S(1000)/f_{CIC}(\theta)$. The absolute energy is then estimated exploiting a set of high quality hybrid events with zenith angles < 60° that have triggered independently the FD and SD. 1475 is the number of these air showers used in the calibration. They have been recorded between January 2004 and December 2012. The correlation between the energy by FD, E_{FD}, and the shower size S_{38} is obtained from a maximum likelihood method and the relation is well described by a single power-law function, as it can be seen in Fig. 3.8. Using the FD energy resolution of 7.6%, the resulting SD energy resolution with its statistical uncertainty is $\sigma_{E_{SD}}/E_{SD}$=(16±0.1)% at the lower energy edge in Fig. 3.8 and (12±1)% at the highest energies. The absolute energy scale is determined by the FD and it has a systematic uncertainty of 14% [89].
  The described procedure is applied to standard events. For lower energy events, which are measured by the infill array (see description in the Sec. 3.6), an analogous energy estimator is defined and it is called S_{35} [90].
  For very inclined events (zenith angle > 60°), the reconstruction is performed with a different method, as the shower is dominated by muons and the electromagnetic component is largely absorbed. The energy estimator is called N_{19} and it is defined as the normalisation of the muon content of a particular event relative to a reference 2D muon distribution at ground, derived from simulated proton showers with an energy of 10^{19} eV for a given arrival direction [91]. N_{19} is thus independent of the zenith angle.

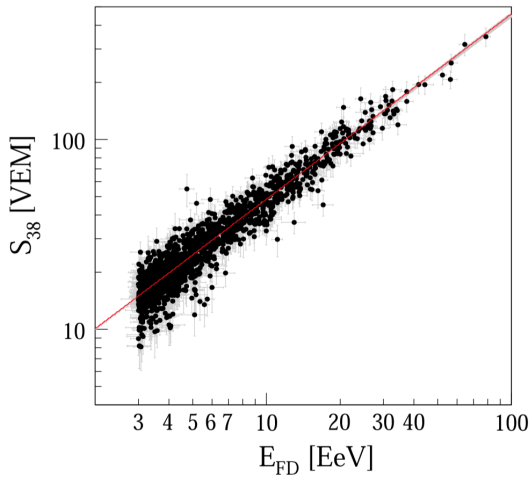

Figure 3.8: Correlation between S_{38} and E_{FD} [87, 88].

3.4 The Fluorescence Detector

In Fig. 3.1, the four sites of the FD are depicted: Los Leones, Los Morados, Loma Amarilla and Coihueco. Six independent telescopes are located at each FD site in a clean climate controlled building. A schematic view of such a building is reported in Fig. 3.9 (panel a). The telescopes look towards the array interior and the combination of a $30^\circ \times 30^\circ$ field of view in azimuth and elevation guarantees 180° azimuthal coverage. The minimum elevation above the horizon is 1.5°.
A sketch of the different components of a telescope is reported in Fig. 3.9 (panel b). Each telescope is designed with Schmidt optics in order to reduce the coma aberration, present in large optical systems. Fluorescence light by air showers passes through a circular diaphragm of 1.1 m radius covered with a Schott MUG-6 filter glass window. The filter transmission is above 50% (80%) between 310 and 390 nm (330 and 380 nm). The primary mirror has a very large area of 13 m^2, thus it is segmented to reduce cost and weight. The light is focused by it onto the camera, which is composed of a matrix of 440 pixels located on the focal surface of the telescope. The pixel field of view corresponds to an angular size of 1.5°. Hexagonal XP3062 Photonis photomultiplier tubes are positioned inside 40mm diameter holes drilled through the camera block at the locations of the pixel centers. PMTs are connected to a distribution board located just behind the camera body. Each board serves 44 PMTs, providing high and low voltage and receiving the output signals. The signal is then shaped and digitized in the front-end electronics unit, where threshold and geometry triggers are also generated. Analog boards in the front-end electronics unit are designed to handle the large dynamic range required for air fluorescence measurements; this means a range of 15 bits and 100 ns timing.
The telescopes are protected against daylight, rain and wind by automatic shutters. In addition, a fail-safe curtain is mounted behind the diaphragm to prevent daylight from illuminating a camera in case of a malfunction of the shutter or a failure of the slow control system. An extensive description of the FD can be found in [92].

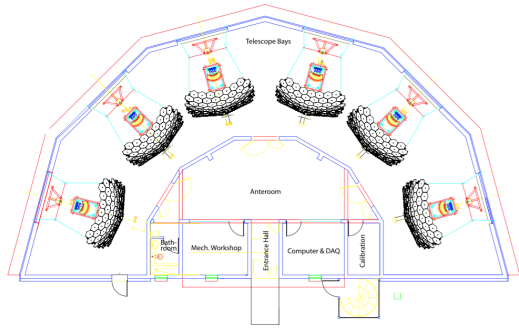

(a)

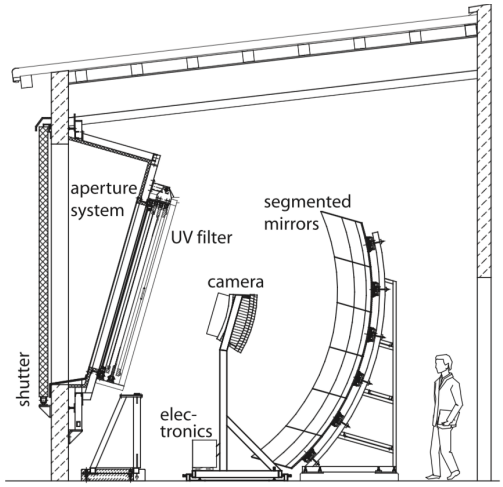

(b)

Figure 3.9: Schematic layout of the building with six fluorescence telescopes (panel a). A sketch of the different components of a Pierre Auger fluorescence telescope (panel b).

FD calibration

An absolute, end-to-end calibration for each pixel of the fluorescence telescopes is performed in order to convert ADC counts to light flux. For this scope, a pulsed and calibrated UV LED drum-shaped light source is used. Absolute calibration constants are obtained from the ratio of the known pulsed flux of photons emitted by the drum and the corresponding ADC pulse integrals of the camera pixels. The average response of the FD is approximately 4.5 photons/ADC bin.
In addition to the drum calibration, other calibration tools are used as well. Periodically, a Rayleigh calibration system consisting of remote laser shots at 337 and 355 nm is used as an independent check on the drum light source calibration. Besides, in order to track both short and long term changes in detector response, before and after each night of data taking a relative calibration of the PMTs is performed. The relative FD response has been measured using a monochromator-based drum light source with a xenon flasher. The measurement is done in steps of 5 nm from 270 nm to 430 nm.

FD trigger

As the PMT data are processed, they are passed through a flexible three-stage trigger system implemented in firmware and software. The trigger rate of each pixel in a camera (first level trigger) is kept around 100 Hz by adjusting the pixel threshold level. The algorithm of the second level trigger searches for track segments at least five pixels in length within a camera. The typical trigger rate per camera fluctuates between 0.1 and 10 Hz. The third level trigger is a software algorithm designed to clean the air shower data stream of noise events that survive the low-level hardware triggers. It is optimised for the fast rejection of triggers caused by lightnings, triggers caused by cosmic ray muon impacts on the camera and randomly triggered pixels.

FD event reconstruction

In the FD, cosmic ray showers are detected as a sequence of triggered pixels in the camera. Fig. 3.10 is an example of an event seen by the FD. This image maps the shower longitudinal development, from which the energy and the mass of the primary CR are measured, as briefly outlined in Sec. 2.2.2. The main steps for the reconstruction of these physical quantities are the following.

- The first step is the geometry reconstruction, by the determination of the *Shower-Detector Plane* (SDP). This is sketched in Fig. 3.11. Experimentally, it is the plane containing the shower axis and the triggered fluorescence telescope. Each pulse pixel can be associated with an angle χ_i along the SDP with respect to the horizontal axis at the telescope. The angular movement of the shower within the SDP is represented by a three-parameter equation:

$$t(\chi_i) = t_0 + \frac{R_p}{c} \tan\left(\frac{\chi_0 - \chi_i}{2}\right) \tag{3.4}$$

  t_0 is the time when the shower front on the axis passes the point of closest approach R_p to the camera. χ_0 is the angle between the ground plane and the shower axis. These three parameters, t_0, R_p and χ_0, can be determined by fitting the data points to this functional form. However, it displays a degeneracy between the impact parameter R_p and the angle χ_0, leading to a poor pointing resolution. This can be improved by performing the *stereo reconstruction* (a second telescope that

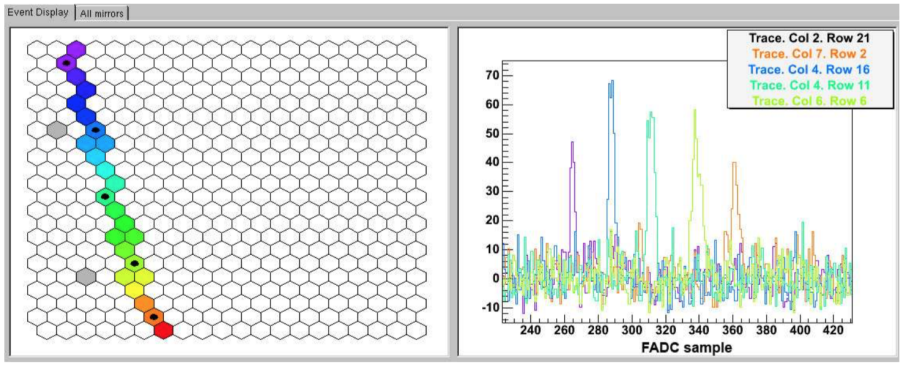

Figure 3.10: Example of a cosmic ray shower as seen in the FD event display. The pattern of the activated pixels is shown in the left panel while the right panel exhibits the response of the selected pixels as a function of time for the pixels marked by a black dot. The bin size is 100 ns.

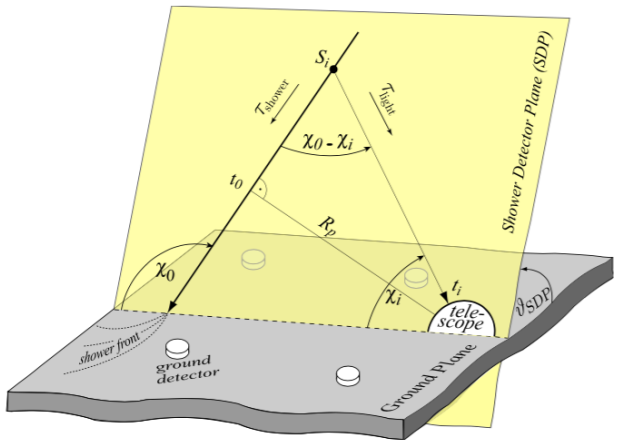

Figure 3.11: Shower geometry seen by a fluorescence detector.

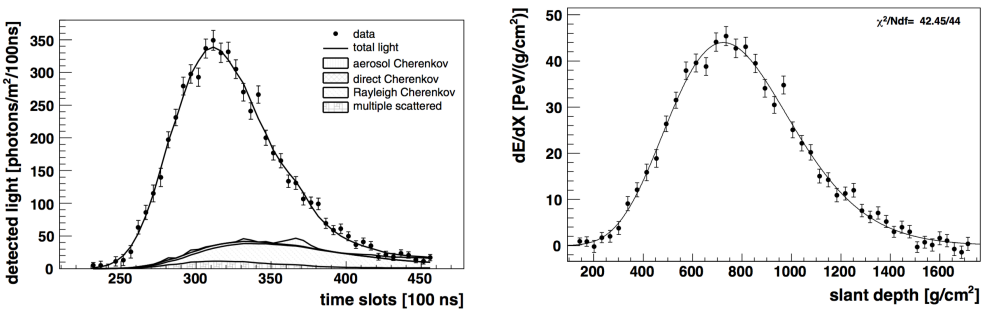

(a) (b)

Figure 3.12: (Panel a) Example of a light-at-aperture measurement (dots) and reconstructed light sources (hatched areas). (Panel b) Its corresponding energy deposit profile. The line shows a Gaisser-Hillas fit of the profile. The reconstructed energy for this shower is $3.0\pm0.2\times10^{19}$ eV.

views the shower from a different position). Alternatively, the so-called *hybrid detection* can be exploited, i.e. the t_0 parameter can be constrained by a direct SD measurement.

- Once the geometry of the shower is known, the light collected at the aperture as a function of time can be converted to energy deposit at the shower as a function of slant depth. The delicate point is disentangling of different contributions to the collected light: fluorescence light [93], direct and scattered Cherenkov light [94, 95] as well as multiple-scattered light [96, 97, 98]. The calorimetric energy of a shower is then estimated by fitting a Gaisser-Hillas function [99] to the reconstructed energy deposit profile. The Gaisser-Hillas function is given by the equation:

$$f_{GH}(X) = \left(\frac{\mathrm{d}E}{\mathrm{d}X_{max}}\right)\left(\frac{X - X_0}{X_{max} - X_0}\right)^{X_{max}-X_0/\lambda} e^{X_{max}-X/\lambda} \tag{3.5}$$

X_0 is the first interaction point, X_{max} is the depth at which the maximum shower development is reached, λ is the radiation length. The integral of this function is proportional to the total energy of the shower, which is finally obtained by correcting for the "invisible energy" carried away by neutrinos and high energy muons [100]. In Fig. 3.12 an example of the measured light at the telescope aperture together with the reconstructed light contributions (panel a) and its corresponding energy deposit profile (panel b) are shown. The shower energy estimated with the FD has a total systematic uncertainty of 14% [89]. Together with energy determination, the FD reconstruction allows an estimate of the UHECR composition through the depth of shower maximum X_{max}.

3.5 Atmospheric monitoring

The knowledge of the properties and conditions of the atmosphere is fundamental for the accurate reconstruction of an air shower observed by the FD and for the estimation of the exposure of the detectors. To characterise the behaviour of the atmosphere at the Pierre Auger Observatory, extensive atmospheric monitoring is performed during and

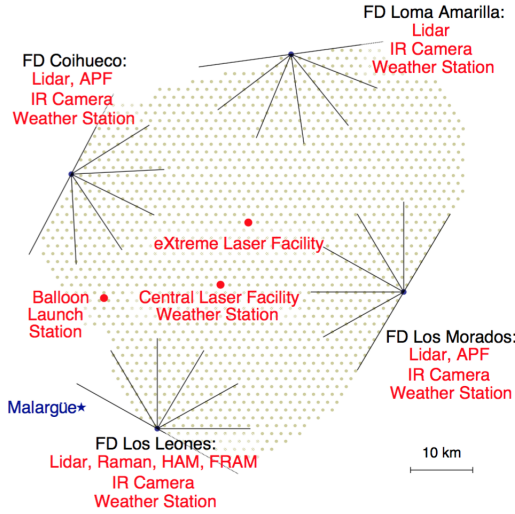

Figure 3.13: Atmospheric monitors at the Pierre Auger Observatory include two central lasers, four elastic lidar stations, one Raman lidar, four IR cameras, five weather stations, a balloon launch facility, two aerosol phase function (APF) monitors, and two optical telescopes (HAM, FRAM).

between FD shifts. A list of monitors and their locations relative to the FD buildings and SD array are shown Fig. 3.13. Atmospheric conditions at ground level are measured by a network of weather stations at each FD site and in the center of the SD; these provide updates on ground-level conditions every five minutes. In addition, regular meteorological radiosonde flights (one or two per week) are used to measure the altitude profiles of atmospheric pressure, temperature and other bulk properties of the air. The weather station monitoring and radiosonde flights are performed day or night, independently of the FD data acquisition. During the dark periods, suitable for FD data-taking, hourly measurements of aerosols are made using the FD telescopes, which record vertical UV laser tracks produced by a Central Laser Facility (CLF) deployed on site since 2003. These measurements are complemented by data from lidar stations located near each FD building, a Raman lidar at one FD site, and the eXtreme Laser Facility (or XLF, named for its remote location) deployed in November 2008. Two Aerosol Phase Function Monitors (APFs) are used to determine the aerosol scattering properties of the atmosphere, exploiting collimated horizontal light beams produced by Xenon flashers. Two optical telescopes, the Horizontal Attenuation Monitor (HAM) and the (F/ph)otometric Robotic Telescope for Atmospheric Monitoring (FRAM) record data used to determine the wavelength dependence of the aerosol attenuation. Finally, clouds are measured hourly by the lidar stations and infrared cameras on the roof of each FD building are used to record the cloud coverage in the FD field of view every five minutes. An extensive description of these facilities and their role in the event reconstruction can be found in [101].

3.6 Enhancements to the Observatory

The Pierre Auger Observatory includes other facilities designed to extend its scientific potential. A schematic list about these different components is here reported and a more

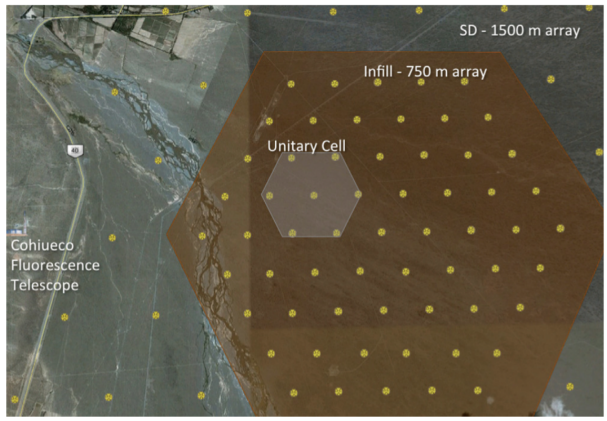

Figure 3.14: AMIGA layout: an infill of surface stations with a detector spacing of 750 m, plus plastic scintillators of 30 m^2, buried under $\simeq$ 540 g/cm^2 of vertical mass to measure the muon component of the showers. The small shaded area indicates the prototype hexagon (Unitary Cell) of the muon detector.

in-depth discussion can be found in [102].

- AMIGA (Auger Muons and Infill for the Ground Array) is the SD enhancement for low energy studies. It is located around the Coihueco FD building and it consists of a denser sub-array of 60 additional stations with spacing of 750 m, for an overall area of 23.5 km^2. The smaller spacing allows for a full efficiency detection of events above 3×10^{17} eV. The reconstruction of infill events is performed following about the same steps of the standard array, except for some differences in the trigger implementation and in the choice of the energy estimator, as outlined in Sec. 3.3. In addition to the array, the AMIGA enhancement includes muon detectors, consisting of 30 m^2 plastic scintillators buried at a depth of 2.3 m aside the SD stations. The aim is the measurement of GeV muons to extract relevant information on the mass composition of cosmic rays. The SD 750 m array was completed in September 2011, while the first prototype hexagon of buried scintillators, the so-called *Unitary Cell*, has been fully operational since March 2015. AMIGA array is depicted in Fig. 3.14.

- HEAT (High Elevation Auger Telescopes) consists of three additional fluorescence telescopes with an elevated field of view. They were built about 180 m in front of the FD site at Coihueco and they were designed to cover the elevation range from 30° to 58°, which lies above the field of view of the other FD telescopes. The HEAT telescopes allow a determination of the cosmic ray spectrum and X_{max} distributions in the energy range from below the second knee ($\simeq 10^{17}$ eV) up to the ankle ($\simeq 5\times10^{18}$ eV). A picture of HEAT is reported in Fig. 3.15.

- AERA (Auger Engineering Radio Array) is used to detect radio emission from EAS with energies beyond 10^{17} eV in the 30 - 80 MHz frequency band. After three phases of deployment, AERA now consists of more than 150 autonomous radio stations with different spacings, covering an area of about 17 km^2. It is located at the same site as other low-energy detector extensions, enabling combinations with various other measurement techniques. The radio array allows different techni-

Figure 3.15: Picture of the three HEAT telescopes in tilted mode. The container for DAQ, slow control, and calibration hardware is behind the enclosure of the second telescope.

cal schemes to be explored, as well as cross-calibration of measurements with the established baseline detectors of the Auger Observatory.

- Several microwave detectors have been deployed to operate in conjunction with the Pierre Auger Observatory. Two complementary techniques are currently being pursued. AMBER (Air-shower Microwave Bremsstrahlung Experimental Radiometer), MIDAS (Microwave Detection of Air Showers) and FDWave are prototypes for a large imaging dish antenna. In EASIER (Extensive Air Shower Identification using Electron Radiometer), the microwave emission is detected by antenna horns located on each SD station of the Auger Observatory. MIDAS is a self-triggering system while AMBER, FDWave, and EASIER use the trigger from the Auger detectors to record the emission.

3.7 Upgrade of the Observatory

The Pierre Auger Observatory was planned to operate until the year 2015, but it has been decided to extend its operation until the end of 2024. The motivation of the upgrade, known as *AugerPrime*, is to provide additional measurements in order to address further fundamental questions about UHECR. First of all, one of the scopes is to shed light on the origin of the flux suppression and the mass composition at the highest energies. In addition, the determination of the mass composition is closely related to our understanding of hadronic interactions at those energies which are inaccessible to man-made accelerators.
The key element of the upgrade will be the installation of a new detector consisting of a plastic scintillator plane above each of the existing water-Cherenkov detectors. This detector will provide a complementary measurement of the shower particles: they will be sampled with two detectors having different responses to muons and electromagnetic particles, allowing the reconstruction of the different components.
In addition, the SD stations will be upgraded with new electronics that will process both water Cherenkov and surface scintillator detector signals. Use of the new electronics also aims to increase the data quality (with faster sampling of ADC traces, better timing accuracy, increased dynamic range), to enhance the local trigger and processing capa-

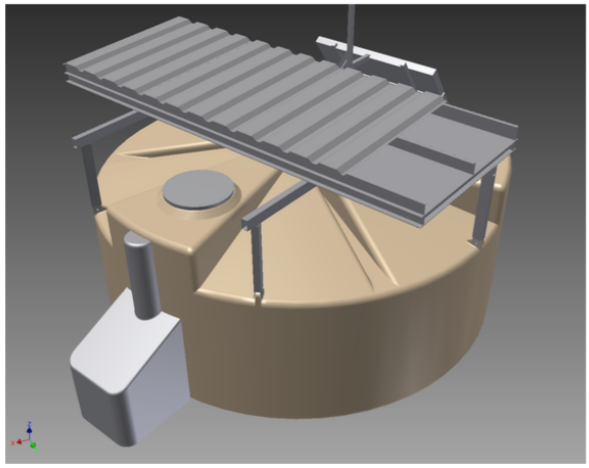

Figure 3.16: 3D view of a plastic scintillator mounted on a water Cherenkov detector. A double roof, with the upper layer being corrugated aluminum (here shown partially cut away for clarity), is used to reduce the temperature variations.

bilities and to improve calibration and monitoring capabilities of the SD stations. The signals of both detectors will be sampled synchronously at a rate of 120MHz (previously 40MHz) and the GPS timing accuracy will be better than 5 ns. The dynamic range of the SD stations will be enhanced by a factor of 32, due to the new electronics and an additional small 1″ PMT that will be inserted in one of the filling ports. More details about AugerPrime can be found in [103].

3.8 Scientific achievements

The data taken with the Pierre Auger Observatory have led to a number of major breakthroughs in the field of UHECRs. In this section, a brief description of the main scientific achievements can be found, together with some comparisons with past and present UHECR experiments. Results regarding mass measurements and corresponding implications on hadronic interaction models will be better described in Chapter 4. In fact, they constitute the context in which the work of this thesis is inserted.

3.8.1 All-particle flux

The all-particle energy spectrum is perhaps the most prominent observable of cosmic rays being investigated. As discussed earlier, it is related both to the UHECR sources and to the galactic and/or intergalactic media in which CRs propagate.
The precise measurement of the UHECR spectrum was one of the main reason for the construction of the Pierre Auger Observatory. In fact, in the past, the data from AGASA and HiRes experiments led to controversial conclusions on the presence of a suppression at the highest energies. This problem has now been solved, thanks to the large statistics collected for more than ten years of observation at the Pierre Auger Observatory: the measurements confirm the presence of a flux suppression without any doubt.
In Fig. 3.17, the updated all-particle spectrum above 3×10^{17} eV is shown. It is obtained by combining four independent data sets, as reported on the left panel: the data from

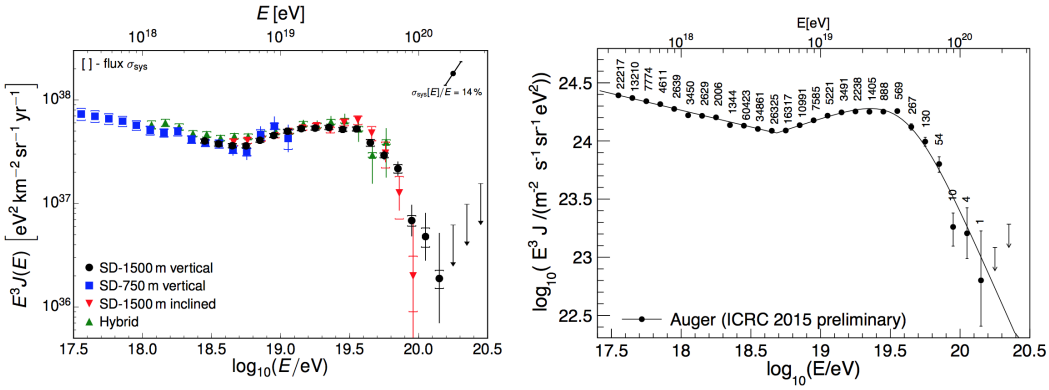

Figure 3.17: Energy spectrum of cosmic rays above 3×10^{17} eV measured with the Auger Observatory [104]. Left panel: the four energy spectra derived from SD and hybrid data. Right panel: the combined energy spectrum. Data are shown with an empirical fit and numbers indicate the statistics of events for each energy bin. Only statistical uncertainties are shown and the upper limits correspond to 84% C.L.

the standard array (i.e. 1500 m spacing), using vertical (θ<60°) and horizontal (60° < θ < 80°) events, the smaller array of 750 m station separation and the hybrid data set (events detected simultaneously by the standard array and the FD) [104]. The four types of measurements are complementary: data from SD-750 m array allow to determine the energy spectrum down to 3×10^{17} eV; data from vertical events obtained with the standard array are fundamental above 3×10^{18} eV up the highest energies; horizontal events provide an independent measurement for the same energy range. These four measurements are then combined using a method that takes into account the systematic uncertainties of the individual measurements. The combined energy spectrum is displayed on the right panel of Fig. 3.17. Its features are quantified by fitting the data with a model that describes the flux by a power-law below the ankle:

$$J(E) = J_0(E/E_{\rm ankle})^{-\gamma_1} \tag{3.6}$$

and a power-law with a smooth suppression at the highest energies:

$$J(E) = J_0 \frac{E}{E_{\rm ankle}}^{-\gamma_2} \left[1+\left(\frac{E_{\rm ankle}}{E_s}\right)^{\Delta\gamma}\right] \left[1+\left(\frac{E}{E_s}\right)^{\Delta\gamma}\right]^{-1} \tag{3.7}$$

γ_1 and γ_2 are the spectral indices respectively below and above the ankle energy $E_{\rm ankle}$. E_s is the energy at which the differential flux falls to one-half of the value of the power-law extrapolation from the intermediate region. $\Delta\gamma$ gives the increment of the spectral index beyond the suppression region. J_0 is the normalisation of the flux, taken as the value of the flux at E = $E_{\rm ankle}$.
The best fit is shown in Fig. 3.17 and the corresponding parameters are reported in table 3.1. The results are described by a power-law spectrum with spectral index 2.6 above 4.8×10^{18} eV and clearly show a steepening of the cosmic-ray flux above an energy $\simeq$ 4.2×10^{19} eV. This suppression has been clearly established with a significance of more than 20σ. The dominant systematic uncertainty of the spectrum stems from the overall uncertainty in the energy scale of 14%.

$J_0[\mathrm{eV}^{-1}\mathrm{km}^{-2}\mathrm{sr}^{-1}\mathrm{yr}^{-1}]$	E_{ankle} [EeV]	E_s [EeV]	γ_1	γ_2	$\Delta\gamma$
$(3.30 \pm 0.15 \pm 0.20) \times 10^{-19}$	$4.82 \pm 0.07 \pm 0.8$	$42.09 \pm 1.7 \pm 7.61$	$3.29 \pm 0.02 \pm 0.05$	$2.60 \pm 0.02 \pm 0.1$	$3.14 \pm 0.2 \pm 0.4$

Table 3.1: Best-fit parameters, with statistical and systematic uncertainties, for the combined energy spectrum measured at the Pierre Auger Observatory [104].

A spectral observable in the flux suppression region that can be used to discriminate between different scenarios of UHECR source-composition is the energy $E_{1/2}$ at which the integral spectrum drops by a factor of two below what would be expected with no cutoff. The value derived from Auger data in Fig. 3.17 is $E_{1/2}$ = 2.47×10^{19} eV. This results differs of 3.4σ from the value predicted under the assumption of homogeneously distributed sources injecting only protons.
All recent UHECR experiments are in good agreement about the position of the ankle and the spectral indices above and below it, but the cut-off is measured by Auger Observatory at a significantly lower energy than TA experiment. In principle, this difference might be due to the different sky regions covered by the two observatories, but no significant flux variation has been found as a function of the declination, that can account for this cut-off shift between spectra from different hemispheres. Therefore, there's currently a work in progress to understand this discrepancy.

3.8.2 Chemical composition

Despite the high precision in the spectrum measurement, its interpretation is hampered by the poor knowledge about the mass of the incoming particles. Determining the chemical composition of UHECRs is in fact the most difficult task in air shower physics. This is essentially due to the dependence of the results on the hadronic interaction models, which constitute at the moment the major source of systematic uncertainty.
The mass composition is usually determined statistically by comparing the first two moments of the X_{max} distributions, $\langle X_{max} \rangle$ and $\sigma(X_{max})$, with the expectations from the EAS simulations. X_{max} is measured by imaging the shower development in the atmosphere using the FD, following the method explained in Sec. 3.4. The average X_{max} is reported on the left panel of Fig. 3.18 as a function of the logarithmic primary energy. Measurements (black points) are displayed together with MC predictions (blue and red lines) in energy bins of $\Delta\log(\mathrm{E/eV})$=0.1. Above $10^{19.5}$ eV an integral bin is used. The hadronic interaction models used for simulating proton and iron-induced air showers are EPOS-LHC, QGSJetII-04 and Sybill2.1. As explained in Sec. 2.1.2, the change of X_{max} with energy is usually referred to as *elongation rate*:

$$D_{10} = \frac{\mathrm{d}\langle X_{max} \rangle}{\mathrm{dlog(E/eV)}} \tag{3.8}$$

The elongation rates predicted by proton and iron air-shower simulations range from 54 to 64 g/cm^2/decade. Any change in the data from these expectations can be therefore attributed to a variation of the primary composition. In particular, the data exhibit a visible change of the slope around 3×10^{18} eV and the best fit on the measurements gives the following results:

$$D_{10} = 86.4 \pm 5.0\ (\mathrm{stat})^{+3.8}_{-3.2}\ (\mathrm{sys})\ \mathrm{g/cm^2/decade} \tag{3.9}$$

below $\log(E_0/\mathrm{eV}) = 18.27 \pm 0.04\ (\mathrm{stat})^{+0.06}_{-0.07}\ (\mathrm{sys})$ and

$$D_{10} = 26.4 \pm 2.5\ (\mathrm{stat})^{+7.0}_{-1.9}\ (\mathrm{sys})\ \mathrm{g/cm^2/decade} \tag{3.10}$$

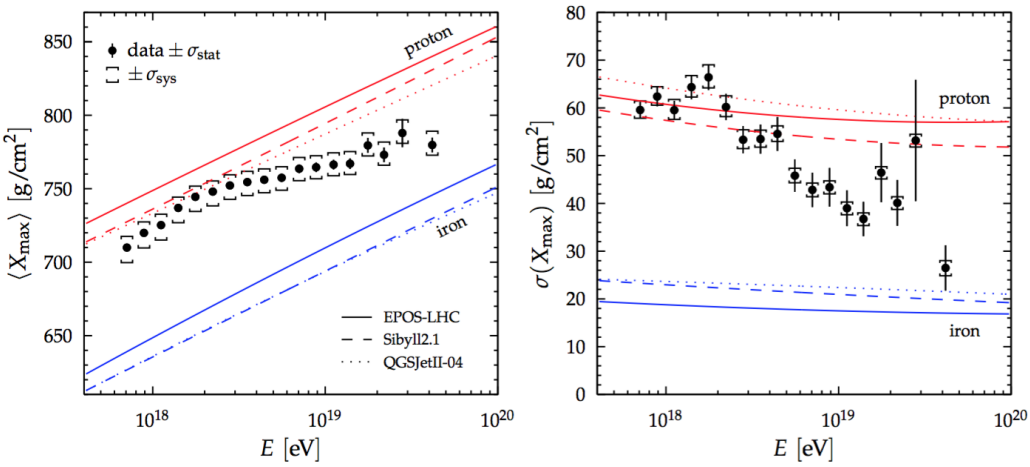

Figure 3.18: Depth of shower maximum, X_{max}, as measured with the Pierre Auger Observatory [105]. Left panel: average X_{max}; right panel: the dispersion of X_{max} after correcting for the reconstruction resolution. The comparison with hadronic model predictions for proton and iron primaries is shown.

above this energy. The trend toward heavier elements is confirmed looking at the width of the X_{max} distribution in the right panel of Fig. 3.18. It can be seen that the $\sigma(X_{max})$ gets narrower towards high energies, as it would be expected for showers induced by heavy nuclei [105].
A careful analysis of composition data of X_{max} from modern and past experiments has been performed and reviewed in [107, 108]. All experiments agree that the light component (proton) dominates in the energy region below the ankle energy region. It is interesting to note that TA observations are consistent with predictions for a pure proton flux in the whole energy range, from the lowest energies 10^{18} eV up to the highest. On the other hand, one should consider that TA measurements have wider error bars. Updated results from the Telescope Array (TA) and Auger Observatories as well as a comparison of the two were presented at the ICRC 2015. An adequate comparison between the two experiments is achieved by taking into account that $\langle X_{max} \rangle$ by Auger is corrected for detector effects, whereas results published by TA include them. In particular, the mass abundances (four mass groups: proton, helium, nitrogen and iron), which best fit the Auger X_{max} data distribution in each energy bin, have been simulated through the Middle Drum (MD) FD of TA and then analysed by the TA Collaboration using the same procedure as applied to their data. This procedure results in the Auger data folded into the TA-MD detector. Results from this comparison are shown in Fig. 3.19. From this preliminary analysis presented in [106] , the conclusion is that the data of the two observatories are in good agreement.
Further details about mass composition studies performed at the Pierre Auger Observatory will be given in Chapter 4.

3.8.3 Arrival direction distribution

Further information about UHECR nature and origin is contained in their arrival direction distribution. This is a very broad field of study that can be summarised as follows:

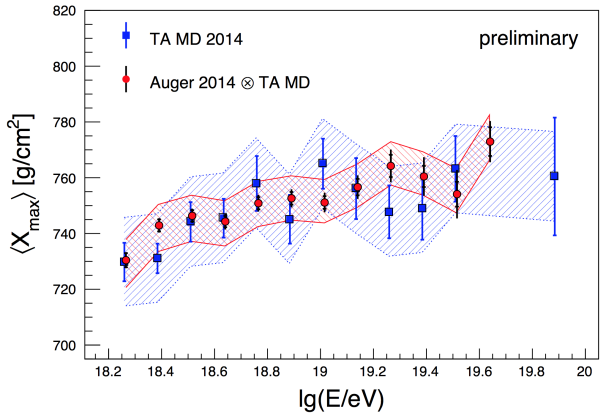

Figure 3.19: Results about the comparison between Pierre Auger Observatory and TA mass measurements. $\langle X_{max} \rangle$ as measured with the MD detector of TA (blue squares) and $\langle X_{max} \rangle$ of the Auger data folded with the MD acceptance (red circles). Considering Auger points, the inner error bars represent the statistical uncertainty and the total error bar also includes contributions from the limited statistics of simulated events used for the folding. The colored bands show the systematic uncertainties of each experiment [106].

searches for large scale anisotropy, searches for localised excesses of the UHECR flux and searches for point sources.

Large-scale anisotropies are possible signatures of the global distribution of cosmic ray sources at all energies. A remarkable result about this topic has been obtained by combining data sets recorded at the Pierre Auger Observatory and TA. In particular, an entire mapping of the celestial sphere above 10^{19} eV has been achieved. This study indicates that the large-scale distribution of UHECR arrival directions is nearly isotropic, except for a dipole moment of amplitude (6.5$\pm$1.9)% measured with a chance probability for an isotropic distribution of 5×10^{-3} and pointing to (93°$\pm$24°) in right ascension and (-46°$\pm$18°) in declination. The distribution of the arrival directions of UHECRs above 10^{19} eV, smoothed by 60° in order to highlight the dipole structure, is shown in Fig.3.20. For what concerns higher multipole moments, these are of the order of 10^{-3} and compatible with the statistical fluctuations expected from an isotropic distribution [109].

As regards the search for anisotropy at small and intermediate angular scale at the highest energies, it is a powerful tool to infer the sources of UHECRs, because it should map (for small magnetic deflections) the inhomogeneous distribution of nearby extra-galactic matter. Comprehensive anisotropy searches have been performed, for different energy thresholds and different angular windows (between 4×10^{19} eV and 8×10^{19} eV, and between 1° and 30°) and by looking for correlations with known astrophysical objects [110]. None of the analyses provides any statistically significant evidence of anisotropy. The two strongest deviations (post-trial probability $\simeq$1.4%) are seen for E>5.8$\times10^{19}$ eV: one points within 15° of the direction of Centaurus A (a close AGN at a distance of about 3.5 Mpc), the other is around 18° of the AGNs observed in X-rays and collected in the Swift-BAT-70 catalogue [111], which are closer than 130 Mpc and brighter than 10^{44} erg/s.

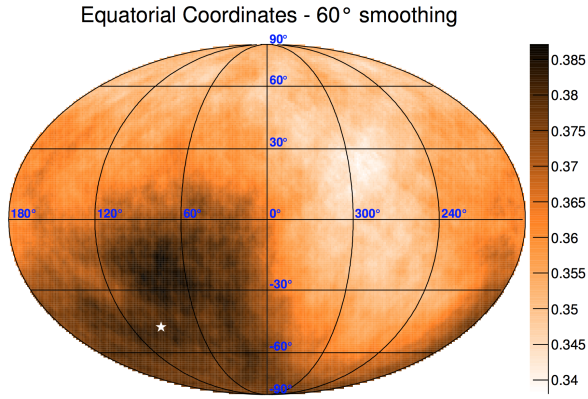

Figure 3.20: Sky map in equatorial coordinates of the average flux smoothed out at a 60° angular scale above 10^{19} eV in km^2 yr^{-1} sr^{-1} units. The direction of the reconstructed dipole is shown as the white star [109].

3.8.4 Photon and neutrino limits

The Pierre Auger Observatory data brought also to placing the best limits on the photon and neutrino components of the flux.
UHE photons can be generated by cosmic rays both by GZK effect and by pion photoproduction or inelastic nuclear collisions near their sources. In addition, a substantial photon flux could be interpreted as a signature of "top-dow" models, which predict that UHECRs come from the decay of exotic particles at the observed energies. As regards UHE neutrinos, they can be produced both by GZK effect and in the decay of charged pions created in the interactions of cosmic rays with matter and/or radiation at their potential sources. Up to now no UHE photons nor neutrinos have been observed by the Auger Observatory, resulting in strong limits on their flux. They are shown in Fig. 3.21 and imply that top-down processes [18] can not account for a significant part of the observed particle flux. In contrast, models in which the production of photons and neutrinos originates from secondaries generated by the propagation in the cosmic background (GZK effect) lead to much lower fluxes. Some representative examples of predicted secondary fluxes of such models are shown in Fig. 3.21, together with measurements by Auger Observatory and other experiments (for more details see [112]). The bounds are reliable as the photon flux limit depend only on the simulation of electromagnetic showers and, hence, are very robust against assumptions about hadronic interactions at very high energy. Besides, the flux limits are approaching the predicted secondary fluxes for models in which the suppression of the CR flux originate completely from GZK process for a proton dominated composition.

3.8.5 Air shower and hadronic interaction physics

Besides the study of UHECRs, the data from the Pierre Auger Observatory are used to extract information about particle interactions at extreme energies. The most significative results in this field can be summarised as follows:

- measurement of the proton-air cross-section σ_{p-Air};
- measurement of the muon deficit of current air shower simulations.

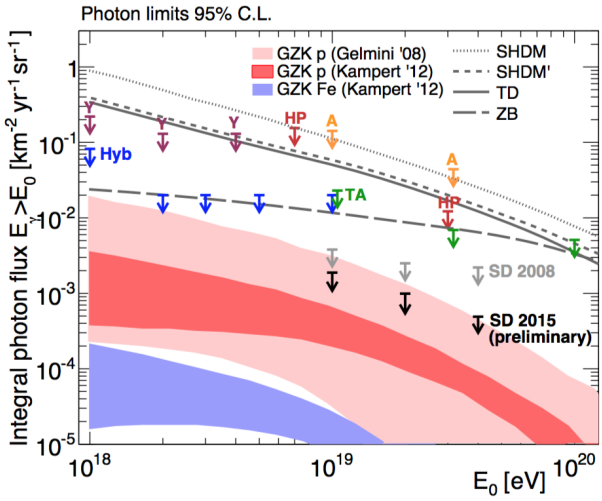

(a)

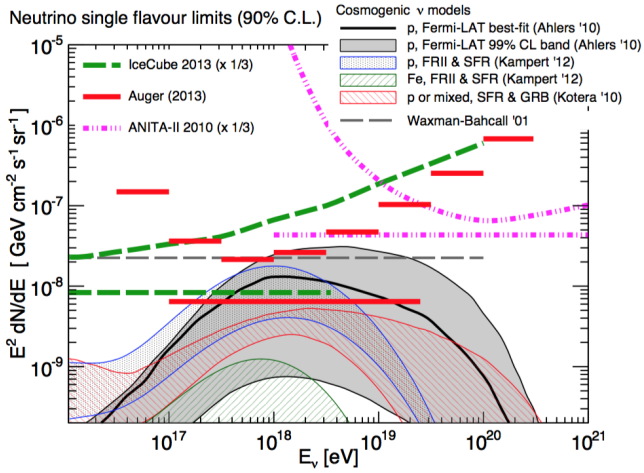

(b)

Figure 3.21: Updated limits on the flux of UHE neutrinos and photons [112]. (Panel a) Upper limits (black) at 95% C.L. to the diffuse flux of photons shown together with previous results from the Pierre Auger Observatory with hybrid (Hyb) and SD data, Telescope Array (TA), Yakutsk (Y), Haverah Park (HP), AGASA (A) and predictions from several top-down and cosmogenic photon models. (Panel b) Upper limits (red lines) to the diffuse flux of neutrinos at 90% C.L. in integrated (horizontal lines) and differential form. Limits are compared with cosmogenic neutrino models, the Waxman-Bahcall bound and limits from IceCube and ANITA experiments. All neutrino limits and fluxes are converted to single-flavour.

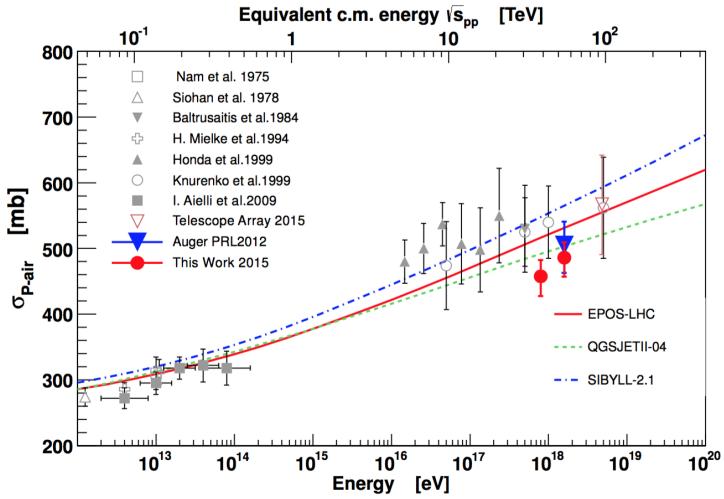

Figure 3.22: Proton-air cross section measured with the Pierre Auger Observatory [113], compared to previous data and model predictions.

As also outlined in Sec. 2.1.4, σ_{p-Air} is one of the main parameters of hadronic interaction models used for predicting EAS properties. In particular, this measurement relies on the depth of the shower maximum, which is directly related to the depth of the first interaction of the cosmic ray in the atmosphere. Based on this correlation, the proton-air cross section has been measured at 57 TeV c.m.s. energy, using hybrid data of the Auger Observatory [113] (see Fig. 3.22). Applying the Glauber approximation, it is possible to convert it to an equivalent inelastic proton-proton cross section. It was found that there's a good agreement between this cross-section and the extrapolation by recent LHC measurements. Data are split in two energy intervals and are consistent with a rising cross section with energy. However, the statistical precision is not yet sufficient to make a statement on the functional form.

As anticipated, another fundamental finding for the hadronic interaction physics concerns current air shower simulations. For many years there have been hints that the number of muons in UHECR showers is larger than predicted by hadronic simulations. The muon deficit in simulations has been recently measured by Pierre Auger Collaboration for events with θ<60° [47]. In particular, in order to quantify a possible discrepancy between simulated and observed air shower properties, two parameters are introduced. R_E is an energy rescaling parameter to allow for a possible shift in the FD energy calibration; R_{had} is a multiplicative rescaling of the hadronic shower component. R_E rescales the total ground signal of the event approximately uniformly, while R_{had} rescales only the contribution to the ground signal of hadronic origin, which consists mostly of muons. The data used for this study are hybrid events with $10^{18.8}$<E<$10^{19.2}$ eV. A set of simulated proton-induced and iron-induced showers matching the longitudinal profile in data is produced using different hadronic interaction models. The ground signal of these data are compared to the simulations and rescaled by using R_E and R_{had}. The results are shown in Fig. 3.23, for mixed and pure proton compositions. The one-sigma statistical uncertainty ellipses are reported, together with the systematic errors displayed by the gray rectangles. The R_E is always compatible with 1 within the uncertainties. For the best case of mixed composition, R_{had} is 1.33±0.16 (1.61±0.21) times larger than predicted

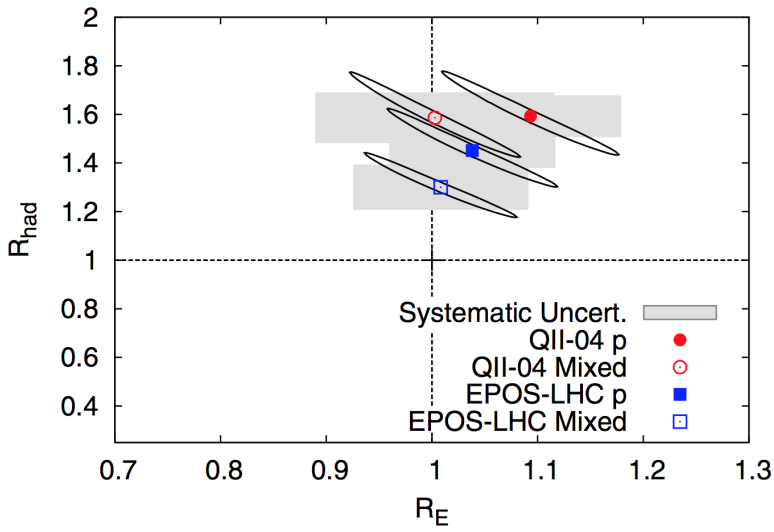

Figure 3.23: Best fit values of parameters R_E and R_{had} for QGSJetII-04 and EPOS-LHC for pure proton and mixed composition. Statistical and systematic uncertainties are reported respectively with the ellipses and gray rectangles [47].

using EPOS-LHC (QGSJetII-04), with a corresponding excess of muons . The significance of this result is between 2.1 and 2.9σ, depending on the hadronic model.
A compatible (but less robust) result had been already found by the Auger Collaboration by means of the analysis of the number of muons of inclined events. This analysis will be discussed in Sec. 4.2.2 in the context of the mass composition measurements.

CHAPTER 4

Mass composition measurements

As already outlined in the previous chapter, the composition of UHECRs is an important ingredient for understanding their origin. The data taken at the Pierre Auger Observatory are well suited to these kind of studies. The Fluorescence Detector (FD) measures the atmospheric depth where the longitudinal development of an air shower reaches the maximum number of particles, i.e. X_{max}. The mean and dispersion of X_{max} are mass-sensitive observables and the corresponding results have been shown in Sec. 3.8.2. UHECRs are described by a predominantly lighter composition up to $3{\times}10^{18}$ eV. For higher energies a trend towards heavier elements is observed. In the following sections, further information obtained from X_{max} will be explained, together with their possible interpretation in terms of astrophysical models (Sec. 4.1). This interpretation depends on the hadronic models used for the MC simulations, which rely on extrapolations of LHC measurements to the ultra-high energies. This is causing the dominating systematic uncertainty in the determination of the primary composition. A key question is whether the underlying physics, as determined at the LHC, is the same at higher energies. In this respect, new additional information comes from the measurements performed at the Pierre Auger Observatory by means of the SD and in the following I will focus on the most significative results, recently published (Sec. 4.2). Among the different observables, muon properties represent a direct handle to explore the hadronic interactions, as muons are products of charged mesons, mostly pions, decaying when their energy becomes is low enough, $\mathcal{O}(100\ \mathrm{GeV})$. A significant discrepancy between observed and predicted muon-related observables can thus be interpreted as a possible hint for an incorrect description of hadronic interactions. As outlined in Sec. 3.8.5, the average hadronic shower is 33% to 60% larger than predicted, with a corresponding deficit of muons in simulations.
The UHECR showers collected and analysed at the Pierre Auger Observatory thus offer the possibility to measure the UHECR composition and, at the same time, to test the simulation models, providing valuable and unique information about hadronic interactions at center-of-mass energies at least a factor of 10 higher than that at the collisions produced at the LHC.

4.1 Estimate of the composition of UHECRs with FD

For a more quantitative study of the evolution of the composition, $\langle X_{max}\rangle$ and $\sigma(X_{max})$ are converted to the first two moments of the logarithmic mass distribution $\ln A$, where A is the mass number. In fact $\langle X_{max}\rangle$ and $\sigma(X_{max})$ are to a good approximation linearly related to $\langle \ln A\rangle$ and its variance V($\ln A$) respectively:

$$\langle X_{max}\rangle = \langle X_{max}\rangle_p + f_E\langle \ln A\rangle \tag{4.1}$$

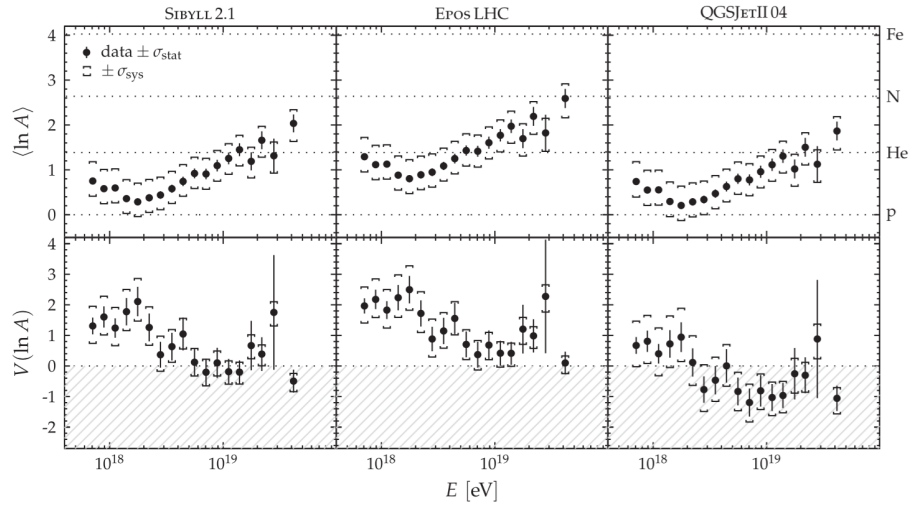

Figure 4.1: Average of the logarithmic mass (top panels) and its variance (bottom panels) estimated from Auger hybrid data using different interaction models. The non-physical region of negative variance is indicated as the gray dashed region [105].

$$\sigma^2(X_{max}) = \langle\sigma^2_{sh}\rangle + f_E^2\sigma^2_{\ln A} \tag{4.2}$$

f_E is a parameter dependent on the energy and on the hadronic interaction model. In the simplified superposition model $f_E = -D/\ln 10$, with D the elongation rate. As regards the dispersion of X_{max} in Eq. (4.2), the first term denotes the shower-to-shower fluctuation, the second term reflects the dispersion in lnA arising from the mass distribution of the composition. Eq. (4.1) and (4.2) can be inverted to obtain $\langle\ln A\rangle$ and its variance V($\ln A$) [114]. The corresponding results obtained by FD data (Fig. 3.18) are shown in Fig. 4.1. From left to right, the three panels refer to Sybill2.1, EPOS-LHC and QGSJetII-04 hadronic interaction models. In the top panels, $\langle\ln A\rangle$=0 and $\langle\ln A\rangle$=4 correspond respectively to proton and iron composition. Intermediate values of $\langle\ln A\rangle$ indicates intermediate elements, like helium and nitrogen.
For all the three models the composition is lightest at around $10^{18.3}$ (2×10^{18}) eV, but there are difference in the absolute value of $\langle\ln A\rangle$ of about ±0.3 considering the different hadronic models. In particular, the interpretation with EPOS-LHC leads to the heaviest average composition, which is compatible with $\langle\ln A\rangle$ of nitrogen at the highest energies.
Considering the variance of lnA, it can give information about the spread in the mass of the primaries. V($\ln A$)=0 indicates a pure composition, V($\ln A$)=4 represents a mixed composition of 50% proton and 50% iron. In Fig. 4.1 (bottom panels) the gray dashed area is the unphysical region of negative values of V($\ln A$). The interpretation with QGSJetII-04 gives unphysical variances above $10^{18.4}$ (2.5×10^{18}) eV and therefore this analysis disfavours this model. As regards EPOS-LHC and Sibyll2.1, the interpretation suggests that the flux of cosmic rays is composed of different nuclei at low energies and that it is dominated by a single type of nucleus at $10^{18.7}$ (5×10^{18}) eV where V($\ln A$) values are close to zero.
A further step in mass composition interpretation can be made by exploiting the full X_{max} distributions. In particular, the shape of the X_{max} distribution in the different

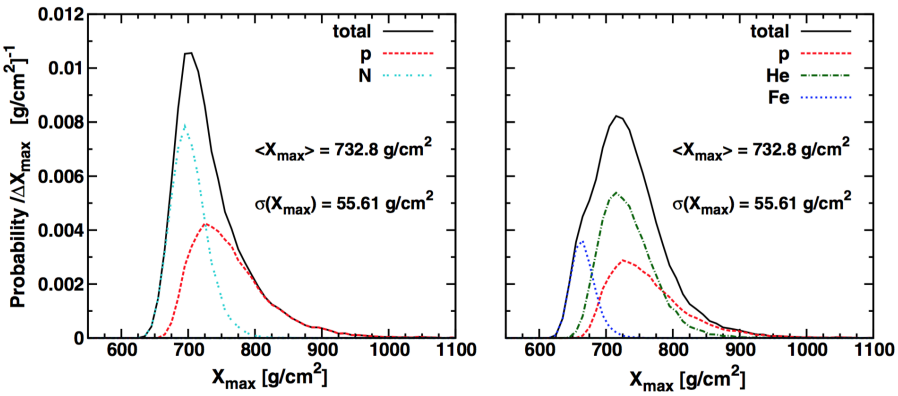

Figure 4.2: Two X_{max} distributions generated with identical mean and dispersion, but with different compositions. The hadronic interaction model EPOS-LHC was used to generate 10^4 events in the range E=$10^{18.2-18.3}$ eV [115].

energy bins reduces degeneracies that can occur when only the first two moments are considered. Fig. 4.2 clearly represents this problem. In fact, two distributions are simulated with different mixes of composition, but with identical means and dispersions. The difference is given by the shapes of the distributions. The shapes give information about mass composition, beyond the mean and dispersion of $\ln A$. In particular, for a given hadronic interaction model, the X_{max} distributions can be compared to predictions obtained with MC simulations of varying nuclear fractions. A binned maximum-likelihood discriminator is used to choose the best-fit fractions. A mixture of the two most stable types of particles, protons and iron nuclei, are first considered. The fits are then extended to include extra components. Specifically, helium and nitrogen nuclei are used as representatives of the intermediate range of nuclear masses. The details of this study are described in [115] and here the results of such analysis, fitting the four mass groups (p, He, N, Fe) to the measured X_{max} distributions, are shown in Fig. 4.3. The hadronic interaction models used for the mass composition interpretation are EPOS-LHC, QGSJetII-04 and Sybill 2.1.
By inspecting the figure, one can make the following considerations:

- in the whole energy range a substantial change in the proton fraction is observed, rising to over 60% around the ankle region. The proton component disappears just below 10^{19} eV.
- At the point of proton disappearance, the fraction of heavier elements starts to rise. There is also indication of a possible proton reappearance at the highest energies, but the low statistics of the FD data does not allow a conclusive statement.
- Looking at the differences among hadronic interaction models, EPOS-LHC indicates that the transition toward heavier elements is mostly due to the rise of the nitrogen fraction, while the two other models favour helium nuclei.
- All models predict neither proton nor iron at the highest energies.

Considering only the ankle energy region, a less model-dependent test about mass composition is given by the rank correlation coefficient r_G between the SD energy estimator S(1000) and X_{max}. The predicted coefficient is shown in Fig.4.4 (left panel), for a set

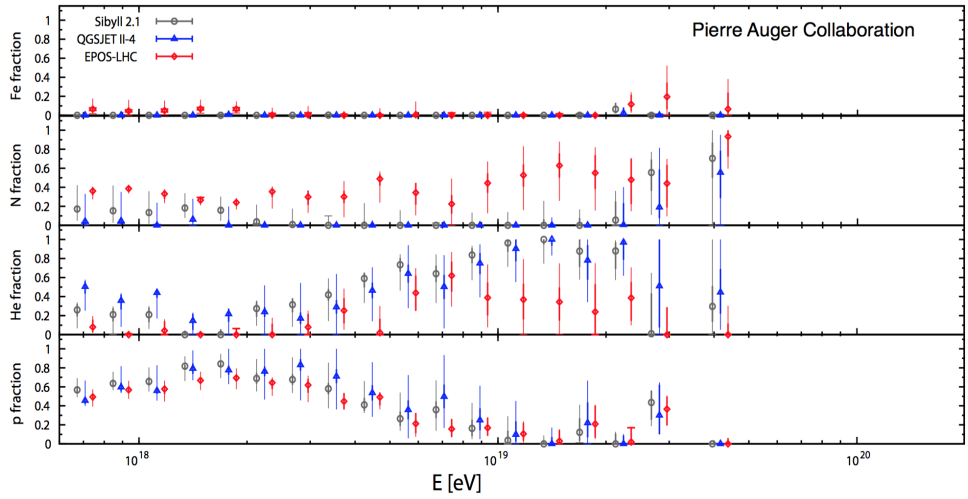

Figure 4.3: Estimate of the composition of UHECRs at the top of the atmosphere. From the bottom to the top, proton, helium, nitrogen and iron fractions are shown for EPOS-LHC, QGSJetII-04 and Sybill2.1 hadronic interaction models. The error bars show the combined statistical and systematic uncertainties of the mass estimates [115].

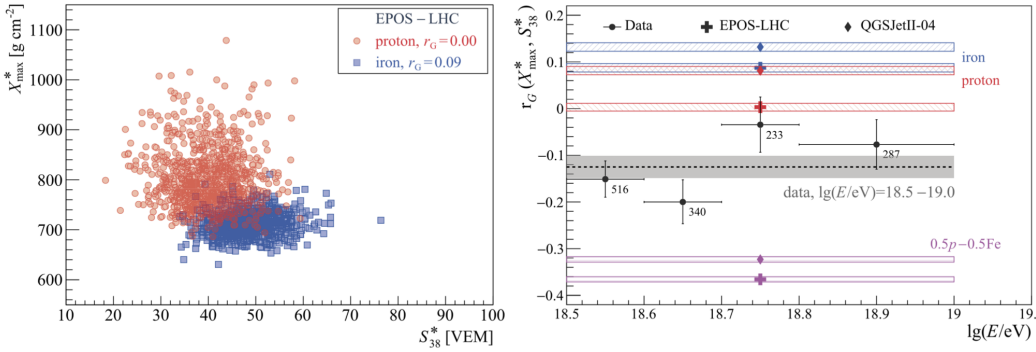

Figure 4.4: (Left panel) X^*_{max} vs. S^*_{38} for log(E/eV) in the range [18.5-19.0] for 1000 proton and 1000 iron showers simulated with EPOS-LHC. X^*_{max} vs. S^*_{38} are respectively the values of X_{max} and S(1000) that one would have observed if the shower had arrived at 38° and 10 EeV (the correlation coefficient is invariant for the specific choice of the reference values). (Right panel) Measurement of r_G in four energy bins between $10^{18.5}$ and 10^{19} eV (numbers of events in each bin are given next to the data points), compared to predictions for pure and mixed composition from different models [116]. See text for more details

of proton and iron showers simulated using EPOS-LHC. It is therefore expected to be zero or slightly positive for a pure mass composition. As reported in Fig. 4.4 (right panel), this coefficient has been measured on data for 4 bins of primary energies, between $10^{18.5}$ and 10^{19} eV. The gray band shows the measured average value for data which is r_G = -0.125$\pm$0.024(stat). Predictions for the correlations r_G in this range for pure proton and iron compositions, and for the extreme mix 50% proton plus 50% iron from EPOS-LHC and QGSJetII-04 models are shown (hatched bands), together with statistical errors. Using the measured value of r_G, the variance V($\ln A$) has been evaluated and it is $\simeq$ 1.35$\pm$0.35, which means a mixed composition in the ankle region, with nuclei heavier than helium A > 4 [116]. These observations are at odds with the values of V($\ln A$) inferred from X_{max} distributions, when using QGSJetII-04 or Sibyll 2.1. Considering instead EPOS-LHC, the composition is close to $\simeq$ 0.35 p - 0.30 He - 0.35 O mix (V($\ln A$) around 1.2, see Fig. 4.1 - central panel). In this case, the corresponding predicted correlation r_G = -0.084 has a better agreement with data: it is within 2σ from the measured value.
Combining the chemical composition information with that coming from anisotropy studies, the interpretation about the origin of UHECRs is not simple. If the ankle feature is interpreted as a transition from galactic to extragalactic cosmic rays, we should expect a certain level of anisotropy in the energy region where the proton fraction is large (if our current knowledge of propagation in galactic magnetic fields is correct). On the contrary as shown in Sec. 3.8, the anisotropy of the Auger data is not larger than a few percent. Thus, the large observed proton fraction is most likely of extragalactic origin (or alternatively we have to accept different assumptions about propagation in galactic magnetic field). As regards the possible reappearance of the proton fraction above 10^{19} eV, it might be related to the anisotropy observed on small angular scales above 5.5×10^{19}eV, but a conclusive statement can not be made given the low statistics of FD data above 10^{19} eV. For this reason, independent methods have been developed by the Pierre Auger Collaboration exploiting the SD data, which do not suffer the lack of statistics at the highest energies, given the almost full detector duty cycle. In addition, the data collected in the suppression region by the AugerPrime upgrade of the Observatory will allow to shed light on this important issue.

4.1.1 Possible data interpretation and astrophysical scenarios

Combining the information from the all-particle spectrum and from X_{max}, different scenarios of UHECR models can be developed. Some key ingredients for these models are the distribution of the sources, the injection energy spectrum, the maximum energy to which a particle can be accelerated, i.e. a cut-off energy, and the chemical composition of UHECR at the source (some of them have been addressed in Chapter 1). In the following, I will summarise the main simplified scenarios used for interpreting UHECR data.

- **Maximum-energy scenario.** As explained in Chapter 1 (Sec. 1.2), the maximum energy to which a particle can be accelerated is also related to its charge. According to this scenario, one obtains a model in which the proton component around the ankle is related to similar components of heavier elements, each shifted in energy by the charge value Z. The end of the spectrum should thus be dominated by heavy elements of the iron group and the observed suppression would be interpreted as a cut-off in the source spectrum. Another important characteristic of this scenario is that protons in the energy region of the ankle are injected by the same extra-galactic sources that produce the flux of heavier elements at the highest energies.

- **Photo-disintegration scenario.** In Sec. 1.3, the UHE nuclei photo-disintegration on CMB photons has been described. Assuming that sources accelerate nuclei above the energy threshold for this reaction, then the light elements could be the secondary fragments of the photo-disintegration of heavier nuclei. In this scenario the suppression of the flux comes mainly from energy losses caused by interactions among heavy elements and the CMB. Lighter elements appear in the spectrum at energies shifted by the ratio of the daughter to parent mass numbers. Once again, as for the maximum-energy scenario, protons in the ankle energy region originate from extra-galactic sources and they are naturally linked to heavy elements at the highest energies of the spectrum.

- **Dip model.** In this picture, the ankle is explained as the imprint of the e^+e^- pair production and the all-particle flux mainly consists of extra-galactic protons at energies higher than 10^{18} eV. The suppression of the spectrum is related only to the photo-pion production. In this scenario, potentially observable fluxes of EeV gamma rays and cosmogenic neutrinos are predicted [117]. Given the results from Auger Observatory on both composition [105, 115, 116] and fluxes from neutrinos and photons [112], this model is strongly disfavoured.

For what concerns the ankle, the analysis about the correlation coefficient between X_{max} and S(1000) (see Fig. 4.4) favours a mixed composition at the ankle, such as is expected from the maximum-energy scenario. In addition, a recent study on the combined fit on both flux and composition measured at the Pierre Auger Observatory seems to favour the same model. The results are shown in Fig. 4.5 [118], where the simulated spectra and the mean and variance of X_{max} corresponding to the best fit on data are reported respectively on the three panels. The fit has been performed for energies above the ankle, where UHECRs are presumably of extragalactic origin. A simple astrophysical model has been adopted, where identical sources are homogeneously distributed in a comoving volume. These inject nuclei of four mass groups (p,He,N,Fe) with a rigidity dependent mechanism and for each species a power-law spectrum is assumed with a broken exponential rigidity cut-off. CRs are propagated from the sources to the observer, taking into account the possible interactions with photon backgrounds. The best fit corresponds to a very hard injection spectrum ($\gamma \simeq 1$) and the spectrum is best fitted by a succession of cut-off of the different groups of elements, thus interestingly indicating that the measured UHECR flux is mostly limited by the maximum energy at the sources.
Despite this interesting result, precise measurements of the composition at the highest energies would further help for interpreting the observations.
In the following sections some alternative methods developed for composition studies will be shown. It has to be underlined that our conclusions about mass composition rely on the accuracy of modeling air showers. A change in the hadronic model predictions would lead to a different interpretation of our mass-sensitive data. On the other hand, the methods that will be described are also an important tool for testing the accuracy of such models.

4.2 Mass composition studies with SD

The first clear advantage of using the SD for mass composition studies relies on its almost full duty cycle, therefore allowing to analyse data at the highest energies of the cosmic ray spectrum, up to the cut-off energy region. In addition, it is possible to gain further insights on UHECR composition and on hadronic interaction models . For example,

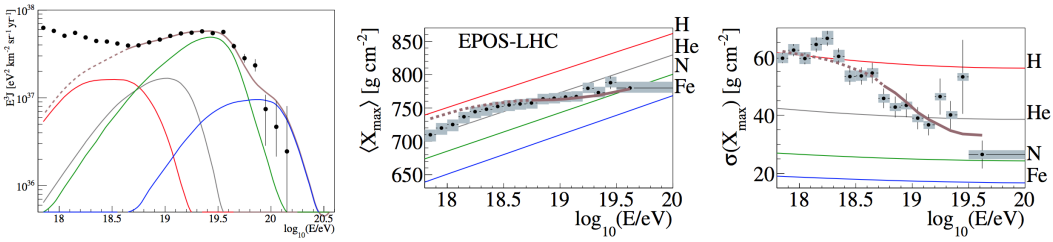

Figure 4.5: (Left panel) Energy spectrum of UHECRs with the best-fit elemental contributions. (Center and right panels) Resulting mean and dispersion of X_{max} distributions (assuming EPOS-LHC for the interactions) for the model prediction (brown), pure p (red), He (grey), N (green) and Fe (blue). Only the energy range where the brown lines are solid is included in the fit. Data are shown by the black points [118].

as already claimed, observations based on the muonic shower component are sensitive to the hadronic particle interactions at all stages of the air shower development, and to several properties of hadronic interactions such as the multiplicity, the elasticity, the production ratio of neutral to charged particles and the baryon-to-pion ratio. For this reason, unique hints can come from the independent studies performed with the SD.
In the following, I will therefore focus on the most significative results obtained by the Pierre Auger Collaboration by means of the SD: the azimuthal asymmetry of rise time in the station signals [119], the muon content at ground for inclined events [120] and the Muon Production Depth [121].

4.2.1 Risetime asymmetry

The water-Cherenkov stations of the SD are used to measure the signal size and the spread in arrival times of the signals produced by the different components of an EAS. A parameter usually employed to characterise the recorded signal is the risetime $t_{1/2}$, i.e. the time of increase from 10% to 50% of the total integrated signal. This quantity indirectly provides a mass-sensitive observable, as will be shown below.
Fig. 4.6 represents three events arriving with different zenith angles. For vertical showers with $\theta \lesssim 30°$ (case a) the signals display a circular symmetry around the angle ζ. This is the azimuthal angle defined on the shower plane, i.e. the plane perpendicular to the shower axis. For more inclined events with $\theta \gtrsim 30°$ (case b), shower particles arriving in the "late" detectors, i.e. in the region defined by $\pi/2 < \zeta < -\pi/2$, will traverse a longer path than particles arriving in the "early" detectors with $-\pi/2 < \zeta < \pi/2$. This generates the so-called *azimuthal asymmetry*, which means that both the signal magnitude and $t_{1/2}$ will depend on ζ. This is due to two effects: the quenching of the electromagnetic signal, plus a geometrical effect. The first one is related to the fact that a larger attenuation of electrons and photons is expected in detectors placed in the late region with respect to early ones, given the different traversed path. The second effect is more related to the muons: the angular distributions of muons impinging on the detectors are different, as late detectors record more muons emitted closer to the shower axis. For very inclined events approaching 90° (case c), muons are the dominant shower component and the asymmetry starts to decrease with the zenith angle. According to these arguments, it is easy to understand how it is expected to have a zenith angle, that we call θ_{max}, where the asymmetry is maximum. This is correlated with the longitudinal shower development [122] and therefore it is a mass-sensitive quantity: it is expected to be smaller for iron

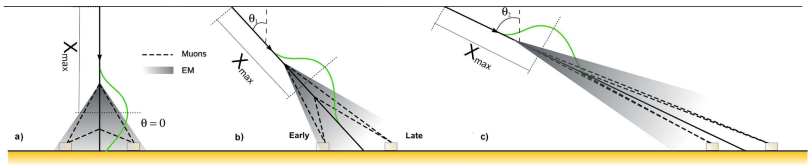

Figure 4.6: Schematic view of the shower development for three different zenith angles [122].

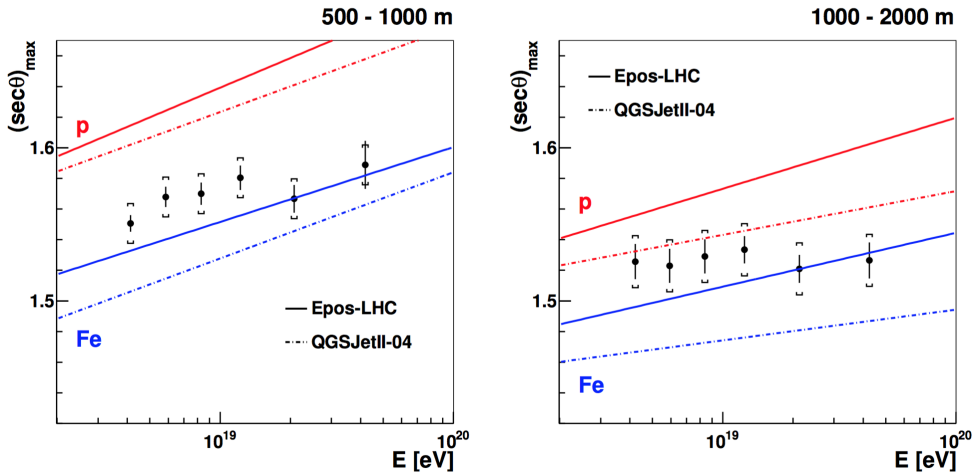

Figure 4.7: $\sec(\theta)_{max}$ evaluated from data above 3×10^{18} eV (black points) (collected from January 2004 to October 2014). The results in the two r-intervals are compared with MC simulations done with EPOS-LHC and QGSJetII04 hadronic models. Brackets on the data are the systematic uncertainties.

than proton for a fixed energy.
On this basis, a study has been published by the Pierre Auger Collaboration [119]. According to this work, instead of θ_{max}, its secant is used: $\sec\theta_{max}$. In order to ensure full detection efficiency, the analysis has been carried out for events with energy above 3×10^{18} eV and for zenith angles $30^\circ < \theta < 62^\circ$. In addition, it has been repeated for two distance intervals, [500-1000 m] and [1000-2000 m], each containing a similar number of signals and events. In fact, $\sec\theta_{max}$ changes with the distance r of the detector to the shower core: near the core the asymmetry is smaller, and thus, the zenith angle at which the muon component starts to dominate (and the asymmetry starts to decrease) is higher. The results of this analysis are shown in Fig. 4.7 and compared to MC predictions for proton and iron-induced showers. The systematic uncertainty on the measured $\sec\theta_{max}$ is 16% at [500-1000 m] and 21% at [1000-2000 m] of the predicted separation between proton and iron for both models. Inspecting Fig. 4.7, it is clear that the Auger data are bracketed by proton and iron for both models, independently of the core distance interval studied. The predicted $\sec\theta_{max}$ has a rather small dependence on energy, but a strong dependence on the hadronic models. For this reason it is difficult to make conclusive statements about mass composition. However, there is an indication of a trend towards heavier nuclei with energy.
The measurements can be converted to the logarithmic mass for a given hadronic model:

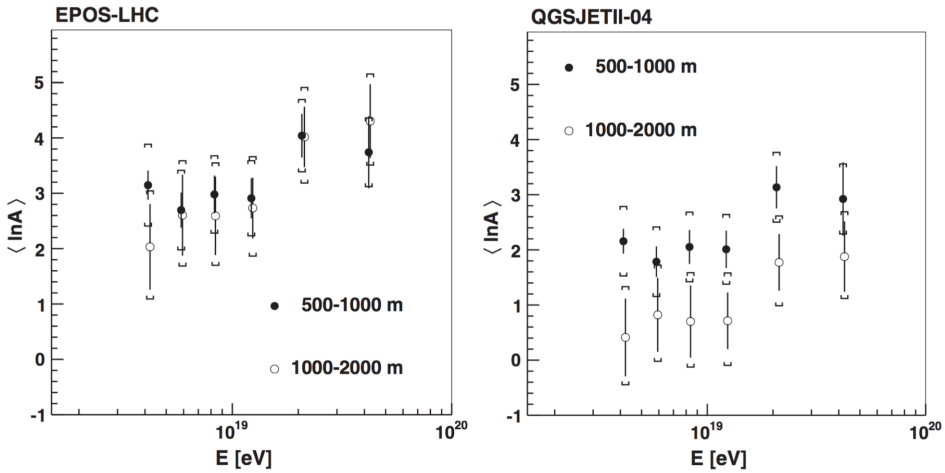

Figure 4.8: Logarithm of the mass derived from $\sec\theta_{max}$ data for the hadronic interaction models EPOS-LHC (left panel) and QGSJetII-04 (right panel) and for the two distance intervals of the analysis.

$$\langle \ln A \rangle = \ln 56 \frac{\sec\theta_{max,p} - \sec\theta_{max,data}}{\sec\theta_{max,p} - \sec\theta_{max,Fe}} \tag{4.3}$$

The results are shown in Fig. 4.8 for the hadronic interaction models EPOS-LHC (left panel) and QGSJetII-04 (right panel) and the two core distance intervals. It is clear that the average $\ln A$ for EPOS-LHC does not depend on the distance range used in the analysis, as expected. Instead the comparison between data and predictions from QGSJetII-04 suggests unphysical conclusions, because the mass seems to depend on the distance of the stations from the core. As a consequence, we can not make inferences about mass composition with the study of $\sec\theta_{max}$, although it can be used to probe the validity of hadronic interaction models. In particular, this analysis disfavours QGSJetII-04 model.

4.2.2 Number of muons in inclined events

The number of muons in an air shower is in principle another mass-sensitive observable. Simulations show that the produced number of muons, N_μ, rises almost linearly with the cosmic-ray energy E, and increases with a small power of the cosmic-ray mass A. This behaviour was already outlined in Sec. 2.1.2, using the simple arguments of the Heitler model for hadronic air showers. Combining Eq. (2.12) and Eq. (2.7), one obtains:

$$N_\mu = A \left(\frac{E/A}{E_c^\pi} \right)^\beta \tag{4.4}$$

where, as before, E_c^π is the pion critical energy.
A very significative result about the number of muons measured on hybrid events has been already discussed in Sec. 3.8.5. Another interesting study about N_μ has been performed at the Pierre Auger Observatory, exploiting very inclined showers with zenith angle θ>62° [120]. Indeed, showers induced by these events traverse a longer path and

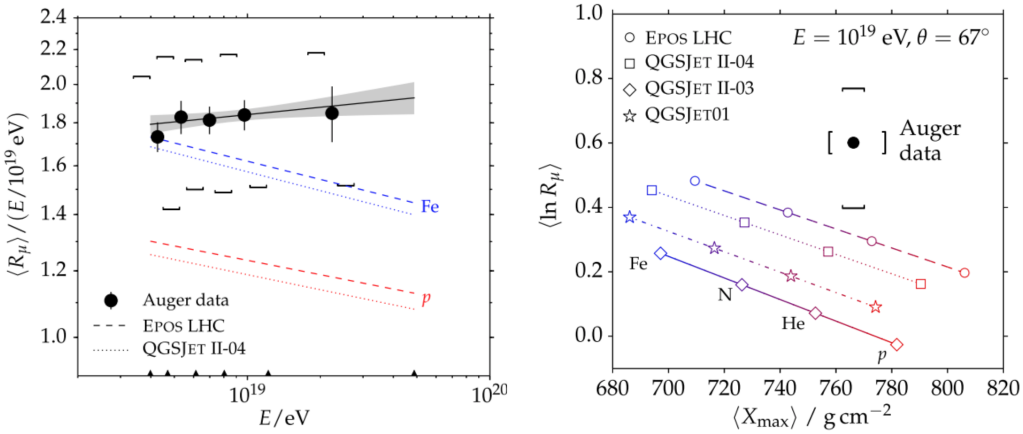

Figure 4.9: (Left panel) Average muon content R_μ per shower energy E as a function of the shower energy E in double logarithmic scale. Black points are the data (collected from 1 January 2004 to 1 January 2013), shown together with the systematic uncertainty. The grey band indicates the statistical uncertainty of the fitted line. (Right panel) Average logarithmic muon content $\langle \ln R\mu \rangle$ as a function of average $\langle X_{max} \rangle$ for data and models [120]

the electromagnetic component is greatly absorbed. This ensures that the signals measured by SD stations are produced by muons.
The muon density at a ground point $\vec{r}$ is factorised in the following way:

$$\rho_\mu(\vec{r}) = N_{19}\rho_{\mu,19}(\vec{r},\theta,\phi) \tag{4.5}$$

where $\rho_{\mu,19}$ is the parametrised ground density for a proton shower simulated at 10^{19} eV with the hadronic interaction model QGSJetII-03 and it is a universal reference distribution for the muon density, because it is mostly independent on the energy of the primary and on the hadronic model used for simulating air shower. The scale factor N_{19} is a relative measurement of the produced number of muons.
The factorisation hypothesis of Eq. (4.5) is tested and confirmed within 5% by comparing the reconstructed muon content N_{19} with the MC simulated muon content. By combining the uncertainty of the reference model with that of the simulated response of the SD stations to muons, the total systematic uncertainty on N_{19} is estimated to be 11%.
The results on data are shown on the left panel of Fig. 4.9, in terms of a quantity called R_μ, which is the measured value N_{19} corrected for its reconstruction bias evaluated on simulations. Since the the muon number increases very rapidly with energy, the scaled quantity $R_\mu/(E_{FD}/10^{19}$ eV) is displayed. The data set consists of hybrid events with zenith angles $62° < \theta < 80°$. There are 5 energy bins, from $10^{18.6}$ eV to $10^{19.3}$ eV and predictions from EAS simulated at θ=67° with EPOS-LHC and QGSJetII-04 are shown together with the data.
As already pointed out in Sec. 3.8.5, there is a large discrepancy between the measured and the predicted number of muons and this is confirmed also by this analysis. If one tries to interpret the data in terms of MC predictions, one can see that there is a small increase with the energy, whereas a decrease is expected from simulations for a pure composition. This suggests a transition from lighter to heavier elements, which is in disagreement with the observations of X_{max}. However, it is clear that conclusions about mass composition can not be drawn from this study.

The disagreement between model predictions and data has been quantified exploiting the X_{max} measurements. In the Heitler approximation, using Eq. (4.4), it is possible to write the logarithm of the number of muons as a function the logarithm of the mass:

$$\langle \ln N_\mu \rangle = \langle \ln N_\mu \rangle_p + (1-\beta)\langle \ln A \rangle \tag{4.6}$$

Since $N_\mu \propto R_\mu$, $\ln N_\mu$ can be replaced with $\ln R_\mu$. By means of Eq. (4.6), the $\langle \ln A \rangle$ of the measured X_{max} can be converted into a prediction of $\langle \ln R_\mu \rangle$, for a certain hadronic interaction model. The corresponding relationship between $\langle \ln R_\mu \rangle$ and $\langle X_{max} \rangle$ can be represented by a line and this is shown in Fig. 4.9. The lines are the predicted $\langle R_\mu \rangle$ at θ=67° for different hadronic models and primaries. The black point represents the Auger measurement at 10^{19} eV. The discrepancy with the MC simulations is highlighted by the lack of overlap between data and model lines. In particular, it has been quantified and the muon deficit of simulations has been found to be 30% to 80 %$[^{+17}_{-20}(\mathrm{sys.})]\%$ at 10^{19} eV depending on the model. The significance of this result is limited because of the uncertainty in the absolute scale of the measurement, which is mainly inherited by the energy scale [89].

4.2.3 Muon Production Depth

The depth at which the muon production is maximum, called X^μ_{max}, is another mass-sensitive observable, correlated with X_{max}. A deeper X^μ_{max} is expected for protons with respect to iron-induced showers. It has been demonstrated that the longitudinal muonic profile can be reconstructed exploiting the SD signal times recorded by the stations. The MPD is the subject of this thesis. In the next chapters, I will give the details about its properties and about the reconstruction method, but, for sake of completeness, I summarise here the published results about X^μ_{max}, compared to model predictions [121].
The analysis is performed using only SD stations between 1700 m and 4000 m from the shower core and for events with energy above $10^{19.3}$ eV ($\simeq$ 20 EeV) and zenith range [55°-65°]. This last choice allows to remove the electromagnetic contamination with a simple threshold signal cut and to end up with a signal which is mainly muonic. The total systematic uncertainty associated to this method is 17 g/cm^2, which corresponds to about 25% of the proton-iron separation. The most relevant sources of error come from the reconstruction method due to differences in the hadronic interaction models and unknown primary mass. This aspect will be elucidated in the following chapter, describing the analysis performed in this thesis.

Fig. 4.10 displays the results (black points) and the hadronic model predictions by EPOS-LHC and QGSJetII-04 for proton and iron-induced showers. The data are divided in five energy bins of width 0.1 in log(E/eV), except for the last bin, which contains all events with energy above log(E/eV)=19.7 ($\simeq$ 50 EeV). The trend of the results is flatter compared to the constant composition of the simulations. This suggests a composition getting heavier with the energy. In addition, it is clear that while the data are bracketed by QGSJetII-04, they fall below the EPOS-LHC estimation for iron. This highlights that the study of the MPD profile can also be used as a tool to constrain hadronic interaction models. Besides, further information on composition can be obtained by reconstructing the shower-to-shower fluctuations of X^μ_{max}, as I will show in this thesis.

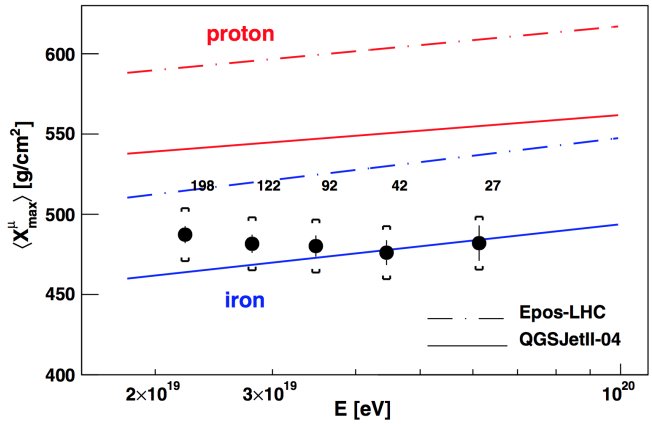

Figure 4.10: Data of $\langle X^{\mu}_{max} \rangle$ (black points) as a function of the energy (period 1 January 2004-31 December 2012), compared with the expectations for proton and iron simulations with EPOS-LHC and QGSJetII-04 hadronic interaction models (colored lines). The numbers indicate how many events are used for each energy bin. The brackets represent the systematic uncertainty.

CHAPTER 5

General properties of the Muon Production Depth

The Pierre Auger Observatory has developed different methods to study the mass composition of UHECRs and, as outlined in Sec. 4.2.3, one of them is the reconstruction of the Muon Production Depth (briefly MPD). My work has been focused on this topic and in particular on extending the applicability ranges of this analysis, as I will show in Chapter 6. In the following, I will mainly describe the general properties of the muonic longitudinal profile, considering the ideal case of the Monte Carlo (MC) EAS simulations without the detector, i.e. at the so-called *generation level* of the simulation. I will discuss how the MPD depends on the zenith angle and the energy of the UHECRs, and on the selected range of core distances for the muon sampling. In addition, I will evaluate its mass discriminating power. For this study, I will use simulations of proton and iron-induced air showers, generated with the CORSIKA propagation code [37] (version 7.335) and the most recent post-LHC hadronic interaction models, EPOS-LHC [39] and QGSJetII-04 [40].

5.1 Apparent MPD and core distance cut

At generation level, the MPD distribution can be built for each simulated UHECR event for the ideal case in which the production height of each muon, z, is a known quantity (z=0 corresponds to the observer altitude). In this context, a first clarification has to be done. The *true* MPD is defined by the total number of muons produced in each slant depth unit, regardless of the probability to reach ground and be detected. Actually, during their travel through the atmosphere, some muons will be absorbed. Only an *apparent* MPD can thus be observed at ground, which is related to the true MPD, through the energy, transverse momentum at production and propagation effects [123]. From now on, I will consider only the detectable MPD, i.e. the apparent distribution which is built using only muons arriving at ground.
More frequently the muon production heights are expressed in terms of amount of traversed matter in $\mathrm{g/cm^2}$:

$$X = \int_z^\infty \rho(z')\mathrm{d}z' \tag{5.1}$$

where z is the muon production height and ρ is the atmospheric density profile. Larger X will correspond to smaller altitudes z. For a given event, the histogram of X of muons forms the MPD distribution. From now on, X will be indicated as X^μ, being obtained only for the muonic shower component. Fig. 5.1 shows an example of apparent MPD profiles, obtained for a set of proton (red) and iron (blue) showers, simulated at 25 EeV and zenith angle 62°. By looking the figure, it is clear that the maximum production of muons for iron showers is reached at a smaller slant depth (higher altitude) with respect

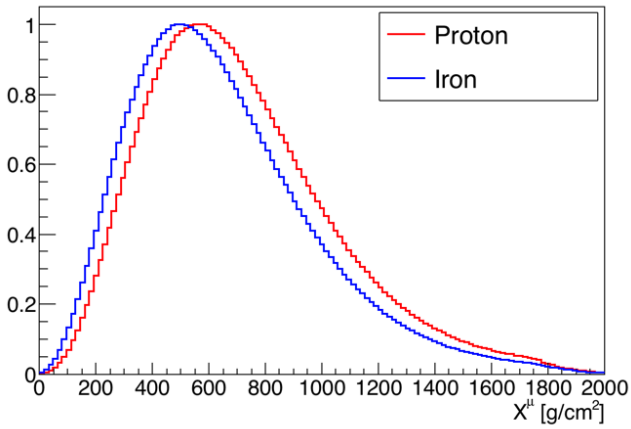

Figure 5.1: Average normalised MPD distributions obtained from a set of proton and iron-induced air showers, simulated at 25 EeV and zenith 62°. All muons arriving at ground are considered.

to proton showers, given the same energy and zenith angle.
The average MPD profiles of Fig. 5.1 are obtained considering all muons arriving at ground, regardless of their distance r from the shower core. The core is the impact point of shower axis at ground and the radial distance r is defined on the shower front plane, which is the plane perpendicular to the shower axis. The MPD reconstruction, which will be described in detail in Chapter 6, is based on approximations not valid for muons arriving close to the core. For this reason only muons arriving at $r > r_{cut}$ are considered. The choice of r_{cut} depends on the details of the analysis and r_{cut}=1200 m has been chosen for this work, allowing a reduction of the reconstruction systematics. The details of this choice will be better clarified in Chapter 6 (Sec. 6.3.1) .
The point to underline here is that the shape of the MPD is significantly affected by the distance cut and this is is clearly shown in Fig.5.2, where average MPD profiles with all muons arriving at ground are compared to those built with muons arriving at r>1200 m. The effect of the cut is the suppression of the tail of the profile, since the latter is mostly populated by low energy muons, produced close to ground and which arrive close to the core. As a consequence, the maximum of the profiles is shifted towards smaller depths and this is more evident for more vertical events (θ<60°). For more inclined events, muons are distributed over a larger area and the percentage of muons removed by the cut is lower. On the contrary muons are spread over a smaller area for vertical events and this explains why the cut effect is stronger.

5.2 The fitting procedure

The average profiles are very useful to qualitatively understand the MPD features, but for a quantitative analysis an event-by-event fit is fundamental. The so-called *Universal Shower Profile function* (USP briefly) is used for this purpose, as it describes very well the asymmetric shape of the MPD profile [124]. The USP function is expressed by the

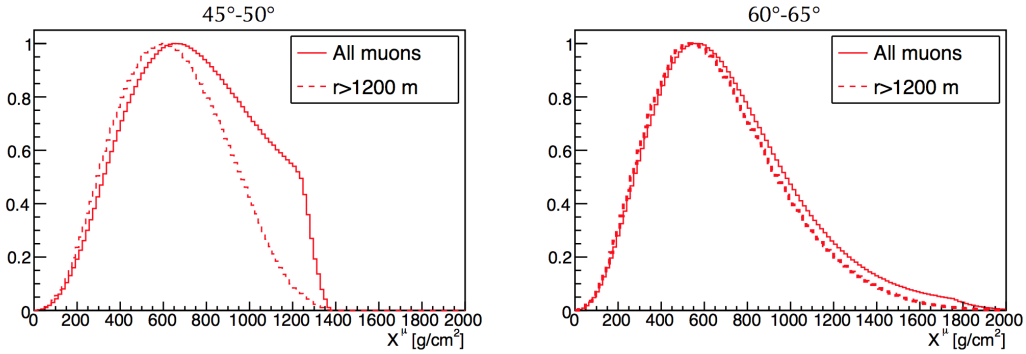

Figure 5.2: Average normalised MPD distributions obtained from proton events at 25 EeV using all muons (full line) and muons arriving at distances r>1200 m from the shower core (dotted line). The left and right panels refers to events with zenith angle ranges respectively [45°-50°] and [60°-65°].

following equation:

$$\frac{1}{N}\frac{\mathrm{d}N}{\mathrm{d}X} = \left(1 + \frac{R}{L}(X - X^{\mu}_{max})\right)^{R^{-2}} \cdot \exp\left(-\frac{X - X^{\mu}_{max}}{LR}\right) \tag{5.2}$$

X is the slant depth defined by Eq. 5.1 and there are four parameters: N is the number of muons, X^{μ}_{max} is the point along the shower axis where the muon production reaches its maximum, L represents the width of the distribution and R is a quantity related to the asymmetric shape of the MPD profile. Larger L values correspond to larger MPD profiles. The larger is the absolute value of R, the larger is the deformation of the distribution with respect to a gaussian function. Positive (negative) R values correspond to distributions with non gaussian tails at high (low) values of X. An example of USP fit is shown in Fig. 5.3 for a simulated proton shower with zenith angle 55° and energy $\log_{10}$(E/eV) = 19.5 ($\simeq$ 30 EeV).

The best set of parameters that describes a given longitudinal muon profile is obtained through a log-likelihood minimisation of the USP function. The fit is performed with free parameters, because the MPD distributions are well sampled at generation level (we will see that this is not true when MPD is reconstructed with the detector). In addition, the fit is applied event-by-event, because of the large shower-to-shower fluctuations, which characterise shower properties. These fluctuations come from the statistical nature of the interaction processes, in particular the height of the first interaction.

In this respect, the fitting procedure is fundamental, allowing to extract X^{μ}_{max}. This will be our main physical observable for composition and hadronic studies, subject of this thesis together with its fluctuations $\sigma(X^{\mu}_{max})$. As anticipated, both X^{μ}_{max} and $\sigma(X^{\mu}_{max})$ are expected to be larger for lighter primaries and they will be therefore exploited to distinguish, at least statistically, EAS originating from different primaries.

Interesting information about the general properties of the MPD comes also from the physical parameters L and R. They have been studied considering the zenith and the energy of the simulated events. Fig. 5.4 shows how L and R vary with the logarithm of the primary energy. Bins of Δlog(E/eV)=0.1 between 19.2 and 20 are used and the results are reported for proton and iron-induced showers, simulated with EPOS-LHC and QGSJetII-04 hadronic interaction models. One can see that both L and R are almost independent of the energy, being the average values 270 g/cm^2 and 0.45 respectively.

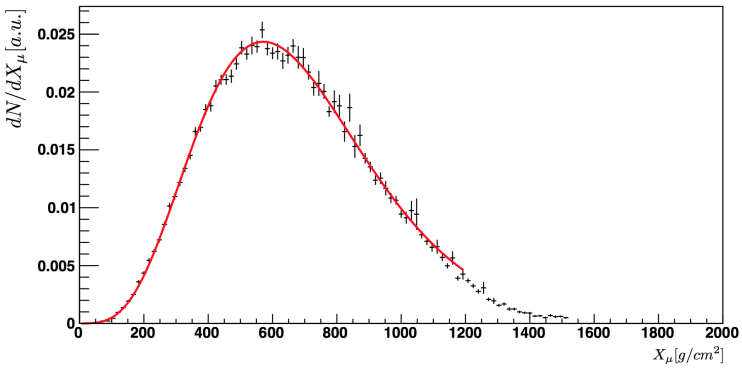

Figure 5.3: Example of MPD distribution for a simulated proton shower at 55° and log(E/eV) =19.5 ($\simeq$ 30 EeV). The USP fit (red line) is also shown. It is performed with free parameters in the range 0-1200 g/cm^2 and it gives X^{μ}_{max} = 571 g/cm^2, L = 265 g/cm^2, R=0.4.

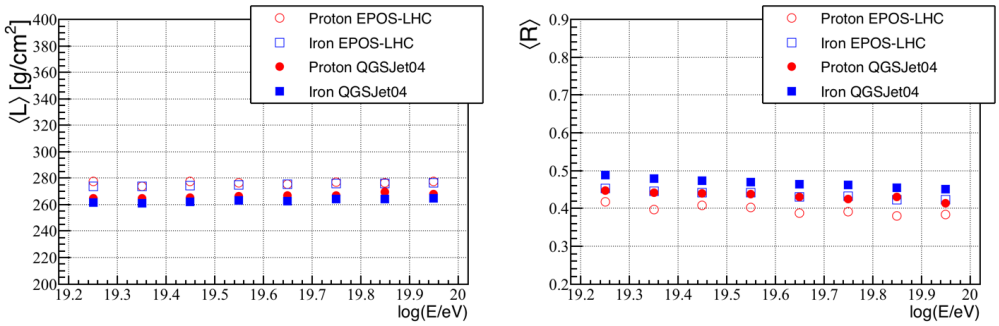

(a) (b)

Figure 5.4: Dependence of USP fit parameters L (panel a) and R (panel b) on the primary energy, shown as a function of logarithmic energy between 19.2 and 20 in bins of width Δlog(E/eV)=0.1.

The MPD shape instead changes significantly with the zenith angle and the profile becomes larger and more asymmetric for high zenith events. This is reported in Fig. 5.5, where L and R parameters are displayed in bins of $\Delta\theta$=5° between 45° and 65°. The study of L and R parameters at generation level turns out to be important for the data analysis. In fact, real MPDs are not well sampled as happens on Monte Carlo and the fit procedure will be performed with the R parameter fixed according to the zenith angle of the event (Sec. 6.3.7).
In the following sections, I will focus on X^{μ}_{max} and $\sigma(X^{\mu}_{max})$ dependence on the zenith angle and energy of the primary.

5.3 Zenith angle dependence

The analysis described in this thesis will be performed for zenith angles θ in the interval [45°-65°]. In order to understand the reasons of this choice, we discuss here the dependence of the MPD on the zenith angle.

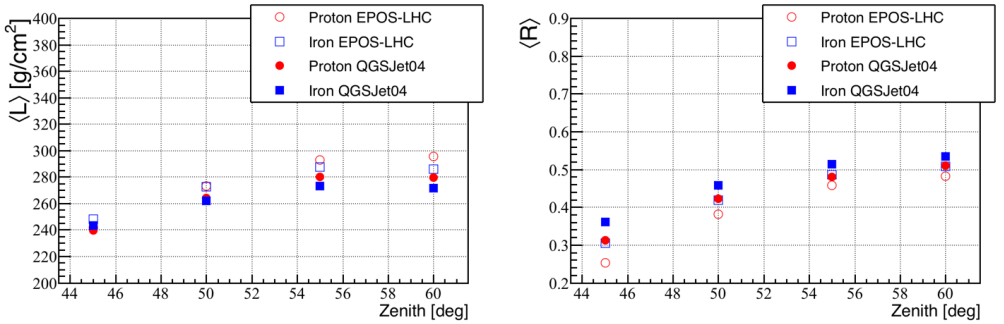

(a) (b)

Figure 5.5: Dependence of USP fit parameters L (panel a) and R (panel b) on the zenith angle of the event, shown between 45° and 65° in bins of width $\Delta\theta$=5°

As already outlined, muons in air showers derive mainly from the decay of charged pions, whose critical energy depends on the atmospheric density. The pion decay probability is in fact greater than the interaction one when air density is low. As a consequence, a more inclined event develops higher in the atmosphere with respect to a vertical event, because of a smaller density of the traversed matter. Fig. 5.6 shows average MPD distributions for four zenith intervals with θ<45° evaluated with respect to the altitude of the Pierre Auger Observatory ($\simeq$ 1400 m). It is clear how for more vertical events the X^{μ}_{max} is less defined, especially for protons. In fact, the maximum development has not been reached yet, when the shower arrives at ground. This explains why 45° has been chosen as lower angular limit of the analysis. Instead, for what concerns the upper value, this is not a physical limit, it is rather due to the kind of reconstruction that should be used. For larger zenith angles, the event reconstruction follows a different procedure [125]) and given the larger muon path, the contributions to the arrival time delays are not simply due to geometrical and kinematic effects (see Sec. 6.3.1).

Fig. 5.7 displays the evolution of the average $\langle X^{\mu}_{max,MC}\rangle$ (panel a) and $\sigma(X^{\mu}_{max,MC})$ (panel b) with the zenith angle, for 4 bins of width $\Delta\theta$=5° between 45° and 65°. The values are obtained by fitting the X^{μ}_{max} distributions of each bin to a gaussian function. The results of the simulations are shown for the two hadronic interaction models EPOS-LHC and QGSJetII-04. One can see that $\langle X^{\mu}_{max}\rangle$ decreases with θ, for the reasons explained above, while the fluctuations slightly increase with it.

For what concerns the absolute values of $\langle X^{\mu}_{max}\rangle$ and $\sigma(X^{\mu}_{max})$, they are very different for proton and iron-induced showers. Note also that $\langle X^{\mu}_{max}\rangle$ is significantly different in the two hadronic interaction models and this makes difficult the study of mass composition. In the following, the mass and model dependence will be discussed.

5.4 Energy dependence and correlation with X_{max}

As discussed in Chapter 2, the electromagnetic component of EAS is characterised by the elongation rate, which is determined by the evolution with the energy of the electromagnetic X_{max}. In the same way, it can be studied exploiting the muonic component of a shower and we will call it as *muonic elongation rate*. The evolution of $\langle X^{\mu}_{max}\rangle$ with the energy is shown in Fig. 5.8 (panel a) for the two hadronic models and for proton and

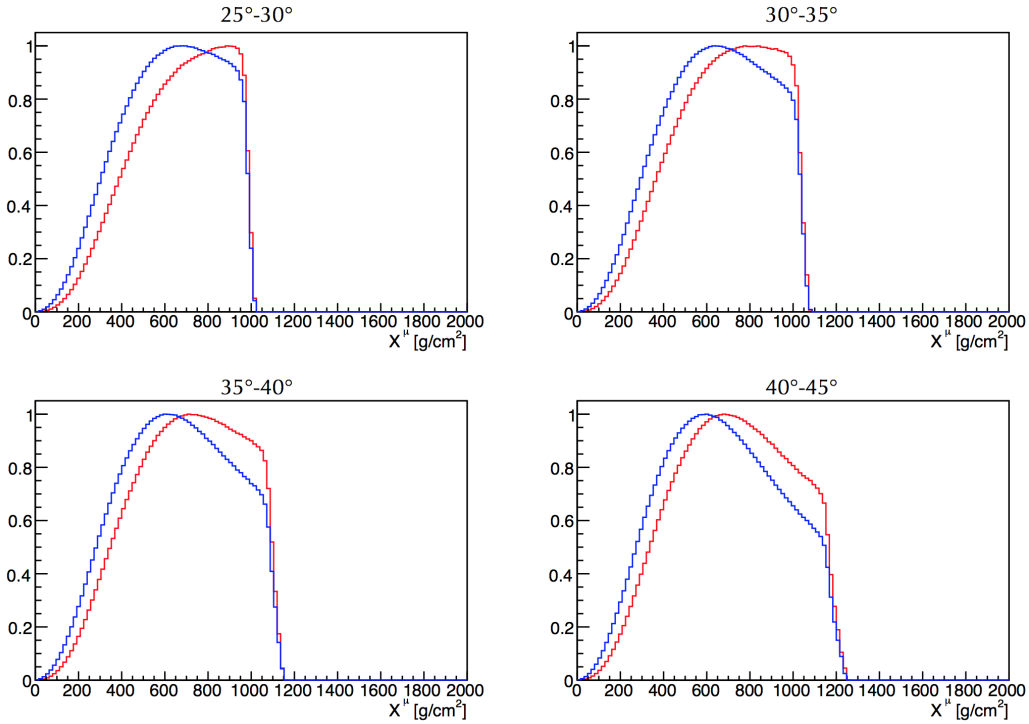

Figure 5.6: Average normalised MPD distributions for a set of proton (red) and iron (blue) induced showers, simulated at 25 EeV. It is clearly visible how the maximum begins to be well defined going to higher zenith angles. For very vertical events the maximum would be reached at a slant depth greater than that of the Pierre Auger Observatory. To better highlight this effect, MPD distributions are calculated considering all muons at ground, without distance cut.

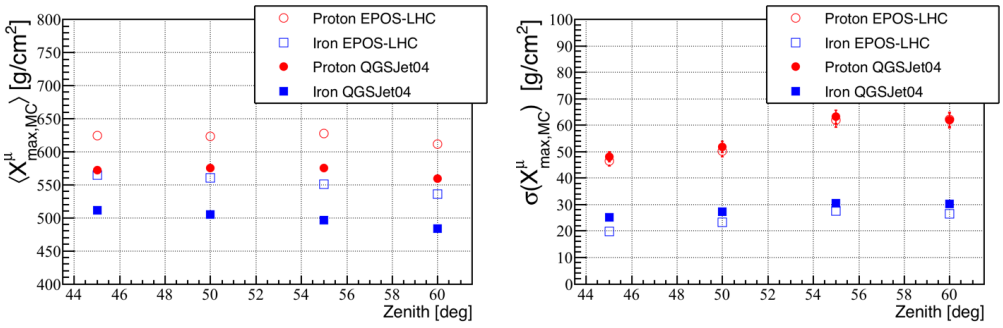

(a) (b)

Figure 5.7: Expectations of $\langle X^{\mu}_{max} \rangle$ (panel a) and $\sigma(X^{\mu}_{max})$ (panel b) as a function of the zenith angle for EPOS-LHC (empty symbols) and QGSJetII-04 (full symbols) and for proton (red) and iron (blue) primaries. The values are obtained by fitting the X^{μ}_{max} distributions of each energy bin to a gaussian function.

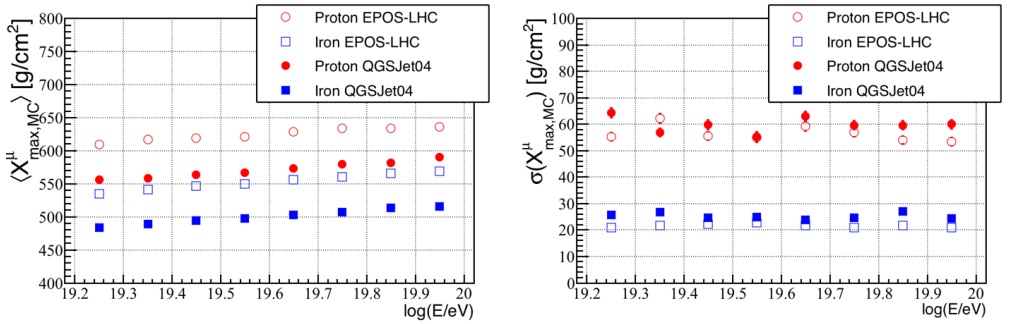

(a) (b)

Figure 5.8: Expectations of $\langle X^{\mu}_{max} \rangle$ (panel a) and $\sigma(X^{\mu}_{max})$ (panel b) as a function of the energy for two hadronic model simulations EPOS-LHC (empty symbols) and QGSJetII-04 (full symbols) and for proton (red) and iron (blue) primaries. The values are obtained by fitting the X^{μ}_{max} distributions of each energy bin to a gaussian function.

iron primaries. The energy on the x-axis is reported in terms of $log_{10}(E/eV)$ and predictions are grouped in 8 bins with width Δlog(E/eV)=0.1, from $10^{19.2}$ ($\simeq$15 EeV) to 10^{20} eV (100 EeV). Using the simplified arguments given in Sec. 2.1.2, it is clear that more energetic primaries develop deeper in the atmosphere. This translates in a larger X^{μ}_{max}, as can be seen from Fig. 5.8. One can also note that the predicted muonic elongation rate is the same for both proton and iron and for the two hadronic models, but the absolute value of $\langle X^{\mu}_{max} \rangle$ is very different between EPOS-LHC and QGSJetII-04. This difference is about 50 g/cm^2 and it is of the same order of the proton-iron separation which is about 70 g/cm^2.

Fig. 5.8 (panel b) shows instead the shower-to-shower fluctuations, $\sigma(X^{\mu}_{max})$, evaluated at generation level as a function of the energy and for the different masses and hadronic models. The shower-to-shower fluctuations are almost constant with the energy and are smaller for iron with respect to proton primaries. $\sigma(X^{\mu}_{max})$ is about 20 g/cm^2 for iron and about 60 g/cm^2 for protons. Unlike X^{μ}_{max}, the predictions of $\sigma(X^{\mu}_{max})$ are in agreement for the two hadronic models. This makes this observable more suitable than X^{μ}_{max} for composition studies.

The predictions are shown for MPDs evaluated with the distance cut r>1200 m and are corrected for the zenith angle dependence displayed in Fig. 5.7. This angular correction will be discussed in Sec. 8.3.

Finally, in this context, it is interesting to underline that, for a given event, Monte Carlo simulations predict that the maximum muon production happens at significantly smaller depths with respect to the electromagnetic maximum, with a difference of about 200 g/cm^2. As already explained, the electromagnetic component of a shower is generated by photons from π_0 decays. The development of this component depends mainly on the primary cross-section and on the critical energy of pions (related to the multiplicity). It has been shown that the predicted elongation rate for X_{max} is linear with primary energy (see 2.1.2) and a similar linear trend is predicted for X^{μ}_{max}, as shown in Fig. 5.8. This indicates that the MPD evolution is regulated by the same parameters of the electromagnetic component evolution.

The correlation between X_{max} and X^{μ}_{max} is confirmed quantitatively by simulations, as one can see by inspecting Fig. 5.9. This shows the predictions of X_{max} and X^{μ}_{max} for

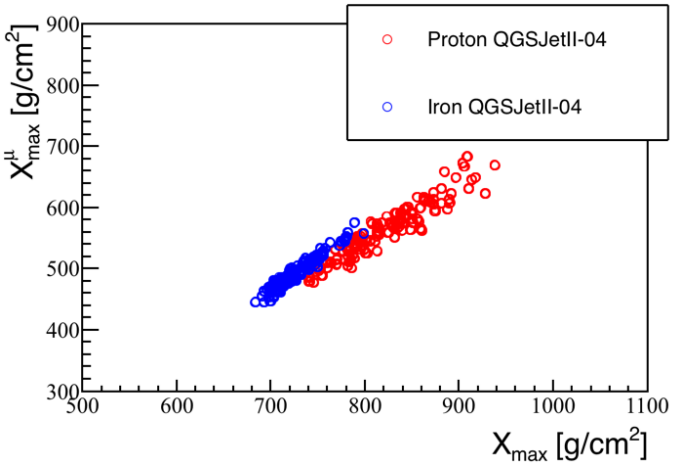

Figure 5.9: Correlation plot between X_{max} and X^{μ}_{max} shown for proton and iron-induced showers, simulated at 35 EeV with the hadronic interaction model QGSJetII-04. The same degree of correlation is observed for EPOS-LHC and when different energies are considered.

proton and iron simulated events at 35 EeV. The two quantities, which describe different aspects of the same shower, exhibit a strong correlation, because they both correlate with the first interaction point X_{first}.
Given the hybrid detection performed at the Pierre Auger Observatory, this opens new possibilities for the mass composition analysis. Exploiting the method for the MPD reconstruction (chapter 6), in Sec. 8.2 a preliminary study will be discussed about the correlation between X_{max} and X^{μ}_{max} as measured on data.

5.5 MPD sensitivity to primary mass composition

A fundamental step is to demonstrate the discriminating capability of the MPD for the mass composition studies. This is already clear enough by looking Fig. 5.8, where the average predicted values of $\langle X^{\mu}_{max} \rangle$ and $\sigma(X^{\mu}_{max})$ are well separated for proton and iron showers. To give a more quantitative estimation of the MPD sensitivity to primary mass composition, the so-called *merit factor* can be evaluated. Fig. 5.10 shows, as example, the distribution of X^{μ}_{max} values predicted for proton and iron-induced showers simulated at 35 EeV (log(E/eV)=19.55). In particular, in order to distinguish the two populations, two conditions should be satisfied. First of all, the average values of proton and iron X^{μ}_{max} distribution have to be sufficiently separated. This is expressed by the following relation:

$$\Delta = \langle X^{\mu}_{max,p} \rangle - \langle X^{\mu}_{max,Fe} \rangle \tag{5.3}$$

where $\langle X^{\mu}_{max,p} \rangle$ and $\langle X^{\mu}_{max,Fe} \rangle$ refer to the average value for proton and iron respectively. The second condition for a good discrimination between primaries is related to the width of the corresponding distributions, which should not be too overlapped. The merit factor can be therefore defined on the basis of Δ and of the standard deviation of the X^{μ}_{max} distributions:

$$D = \frac{\Delta}{\sqrt{\sigma^2(X^{\mu}_{max,p}) + \sigma^2(X^{\mu}_{max,Fe})}} \tag{5.4}$$

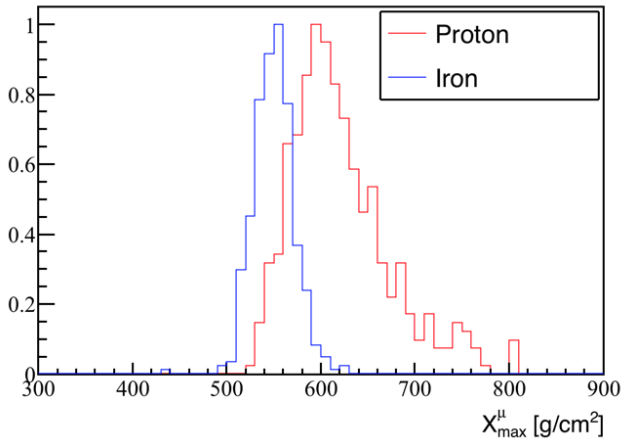

Figure 5.10: Monte Carlo distribution of X^{μ}_{max} obtained for proton and iron-induced showers simulated ad 35 EeV.

where $\sigma(X^{\mu}_{max,p})$ and $\sigma(X^{\mu}_{max,Fe})$ are the standard deviations for proton and iron respectively. Both Δ and the merit factor D are shown for the two hadronic interaction models EPOS-LHC and QGSJetII-04 in Fig. 5.11. On average the separation Δ is 70 g/cm^2 and the merit factor is 1.2, regardless of the primary energy. The discriminating power is the same for the two hadronic interaction models and it has been verified that it is also independent of the zenith angle of the event. Although the merit factor should be evaluated introducing the effects of the real reconstruction, these results confirm that the MPD is a promising tool for mass composition studies of UHECRs. However, one has to take into account the systematics associated to the hadronic interaction models.
The method used for reconstructing the MPD in realistic conditions, by simulating the detector, will be the subject of the following chapter.

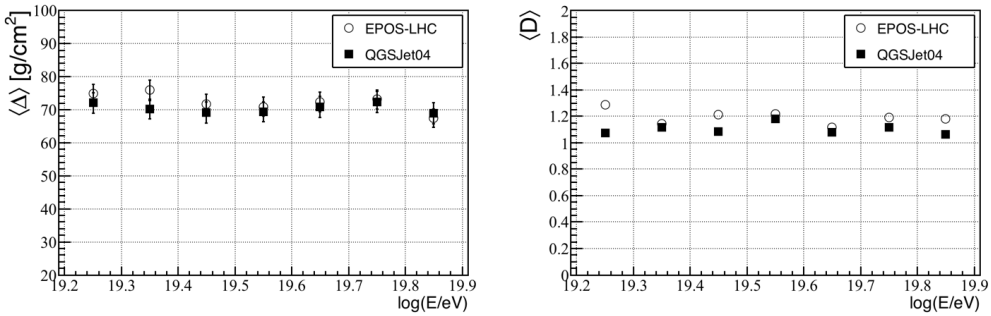

(a) (b)

Figure 5.11: Proton-iron separation Δ (panel a) and merit factor D (panel b) evaluated for simulations with two hadronic interaction models EPOS-LHC and QGSJetII-04 as a function of the logarithmic primary energy.

CHAPTER 6

The extended reconstruction of X^{μ}_{max}

In the previous chapter, the general properties of the MPD have been discussed. It has been highlighted that the muonic longitudinal profiles depend on the zenith angle of the event, on its energy and on the selected core distances at which muons are sampled. In addition, the MPD mass discriminating power, based on the estimation of X^{μ}_{max} and of the corresponding shower-to-shower fluctuations, has been shown.
As explained in Sec. 4.2.3, the Pierre Auger Collaboration published interesting results about MPD for inclined events at [55°-65°] with energies E>$10^{19.3}$ eV and exploiting SD signals collected by stations far from the core (r>1700 m) [121].
The work in this thesis has been focused on extending the applicability of the MPD analysis. The ranges of energy, zenith angle and distances from the core which are explored can be summarised as follows:

- $10^{19.2} \leq$ E $\leq 10^{20}$ eV
- $45° \leq \theta \leq 65°$
- $1200 \leq$ r ≤ 4000 m

The method has been tuned using simulated proton and iron-induced showers, produced with CORSIKA-7.335 code. The simulations are available with two post-LHC hadronic interaction models, QGSJetII-04 and EPOS-LHC, and were produced with thinning level 10^{-6} and energy spectrum E^{-1}. A summary of the Monte Carlo (MC) simulations statistics is given in Table 6.1. Each of those events was then simulated on 8 different positions of the SD array, exploiting the software framework $\overline{\text{Off}}\underline{\text{line}}$ [75].
In the following I will focus on the different ingredients needed for the MPD reconstruction, by using the simulations when also the detector is simulated. In this case the muon production altitudes for a given event are of course unknown variables. The model for deriving muon production points from their arrival times is the same used for the

	QGSJet-II04 p | Fe	EPOS-LHC p | Fe
energy range	$10^{19.2}$-10^{20} eV	$10^{19.2}$-10^{20} eV
angular range	45°-65°	45°-65°
events	2362	2317

Table 6.1: Simulation libraries used in this work. The last row shows the total number of proton and iron-induced showers, for each hadronic interaction model.

published analysis, being the basis of the method. All the other passages have been expressly developed in order to take into account for the various effects introduced by the extended analysis ranges.
The method here described has been recently published [126] on the basis of the work carried out in [127], [128], [129]. Its performances will be evaluated taking into account all the possible dependencies on mass, hadronic interaction models, distance, energy and zenith angle. For this purpose, we define the *bias* on X^{μ}_{max}:

$$\text{bias} = X^{\mu}_{max,Rec} - X^{\mu}_{max,MC} \tag{6.1}$$

where $X^{\mu}_{max,MC}$ is our reference and it is evaluated in the ideal conditions described in the previous chapter, i.e. using the MC muon production altitudes. For the same event, $X^{\mu}_{max,Rec}$ can be estimated after each step of the analysis or after the whole reconstruction chain. Both $X^{\mu}_{max,MC}$ and $X^{\mu}_{max,Rec}$ are calculated using the same energy, zenith angle and distance ranges listed above. In addition, as explained in chapter 5, the USP fit is performed event-by-event for deriving the maximum muon production depth.

6.1 Reconstruction of the MPD from muon time delays

The SD stations of the Pierre Auger Observatory measure the lateral development of a shower, by recording the arrival times of particles at ground. In order to build the muonic longitudinal profile with the SD, the measured muon times must be related to their corresponding production points in the atmosphere. In [123, 130] a phenomenological muon time distribution model has been developed. It establishes a relation between the arrival times of muons at ground with respect to the shower front and their production points in the atmosphere. This model will be briefly described in the following.
The measured muonic time structure at ground is the combination of energy spectra of muons at production, energy loss during propagation and decay probability. Muons are created in the shower by the decay of charged kaons and pions. They are well collimated with the shower axis, being produced in a narrow cylinder around it. A 10 GeV (1 GeV) muon typically will have a 1° (10°) outgoing angle with respect to the shower axis. Because of their long radiation lengths, they do not suffer many interactions in their way to the ground: bremsstrahlung and pair production are improbable and multiple scattering effects are negligible. These are the main reasons which allow to assume that they travel following straight lines from their production point.
A cylindrical coordinate system defined by (z,r,ζ) is used for the muon coordinates at ground and it is depicted in Fig. 6.1. z is the position along the shower axis, r is the distance from it and ζ the polar angle measured on the shower front plane (ζ=0 is in early part of the shower and the angle is oriented counterclockwise). The shower front plane can be defined as the plane perpendicular to the shower axis, that travels at the speed of light c and that hits the ground at t = 0. The coordinates (t,r)=(0,0) represent the shower core and θ is the zenith angle of the event. The distance traveled by a muon can be thus defined simply by:

$$l = \sqrt{r^2 + (z - \Delta)^2} \tag{6.2}$$

where Δ is the distance from the ground impact point to the shower plane:

$$\Delta = r \tan\theta \cos\zeta \tag{6.3}$$

According to the assumptions mentioned above, there are two main contributions to the delay of a muon with respect to the shower front, which can written as:

$$t \simeq t_g + t_\epsilon \tag{6.4}$$

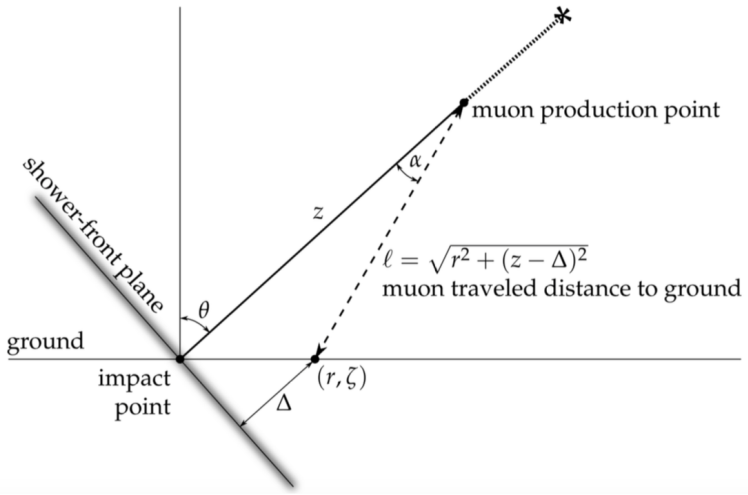

Figure 6.1: Sketch of the geometry of the muon travel path from the production point to the ground. See text for details.

where t is the available observable in the SD stations, t_g and t_ϵ are called respectively geometrical delay and kinematical delay. t_g comes from the geometry depicted in Fig. 6.1: it represents the delay of muons due to the deviation of their trajectories with respect to the shower axis. In fact, muons arriving at a distance r from the shower axis will take longer than those arriving at r=0, being larger their path. t_ϵ is instead related to the muon finite energy: muons travel at a smaller speed than the light one and they lose energy during their path mainly because of inelastic collisions with atomic electrons in the air. For this reason, they are further delayed with respect to the shower front which is assumed to move with the speed of light.
Considering the geometrical delay t_g, the muon arrival time with respect to shower front can be written as:

$$ct_g = l - (z - \Delta) \tag{6.5}$$

Eq. (6.5) can be inverted in order to evaluate z as function of t_g:

$$z = \frac{1}{2}\left(\frac{r^2}{ct_g} - ct_g\right) + \Delta \tag{6.6}$$

By considering that $t_g \simeq t - t_\epsilon$ and by introducing the pion decay length z_π, Eq. (6.6) can be thus rewritten as:

$$z \simeq \frac{1}{2}\left(\frac{r^2}{c(t - t_\epsilon)} - c(t - t_\epsilon)\right) + \Delta - z_\pi \tag{6.7}$$

t_ϵ is not a measurable quantity and it must be parametrised exploiting MC simulations, as it will be explained in Sec. 6.2. The term z_π which appears in the formula takes into account the decay length of the parent pion. Indeed, muons are not produced in the shower axis, but co-linearly with the trajectory followed by the parent pions. The muon

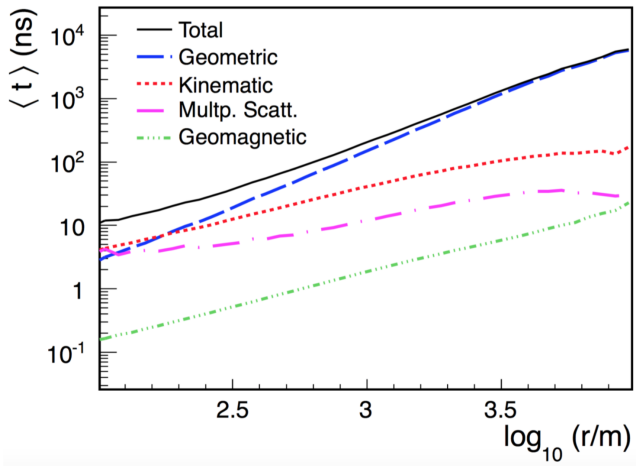

Figure 6.2: Contributions to the average muon delay as a function of the distance from the shower core, for a proton-induced shower with a zenith angle of 60° and primary energy of E=10 EeV [123].

path starts deeper in the atmosphere by an amount which is simply the decay length of the pion:

$$z_\pi = ct_\pi E_\pi/(m_\pi c^2)\cos\alpha \tag{6.8}$$

The pion energy dependence of this correction has been taken from [123]. α is the angle between the vector of the muon momentum and the shower axis. The term z_π introduces an average time delay of ~ 3 ns (this correction amounts to $\sim$1% of the total delay).

As can be seen from Fig. 6.2, there are other sources which can contribute to the total delay of a muon. The muon path can be in fact deflected because of the interaction with the geomagnetic field and/or because of multiple scattering effects. These are important for very inclined events and are negligible in the ranges of this analysis. In addition each delay component plays a different contribution in relation to the distance from the shower core. Going to smaller distances from the core, the kinematical delay becomes significative and this is essentially due to the large spread in muon energies, dominated by low ones [130]. This is one of the reasons which motivated the choice of the distance cut in this analysis, as I will explain in the following section.

Finally, as already mentioned in Sec. 5.1, the muon production altitude z is usually converted in slant depth X, as amount of traversed matter in g/cm^2. The histogram of X for a given event forms the MPD distribution.

Bias of the time model

The performance of the model described in Sec. 6.1 can be estimated by evaluating the bias that it introduces on the MPD reconstruction. In particular, the bias is the difference between $X^\mu_{max,Rec}$ and $X^\mu_{max,MC}$, where $X^\mu_{max,Rec}$ is calculated at generation level by using the muon production heights z^μ derived from the Eq. (6.7) and from the MC muon energies. The kinematical delay contribution t_ϵ is therefore estimated exploiting the simulated muon energies. $X^\mu_{max,MC}$ is instead directly evaluated with the simulated z^μ.

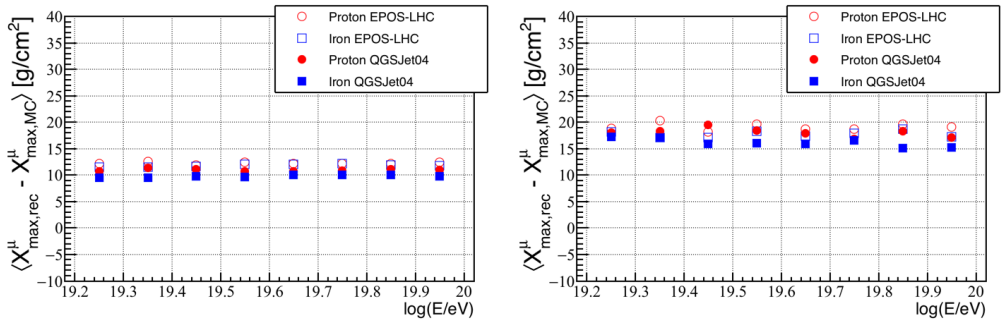

(a) (b)

Figure 6.3: The bias due to the muon time distribution model evaluated for each primary and model, as a function of the energy for [45°-55°] (panel a) and [55°-65°] (panel b).

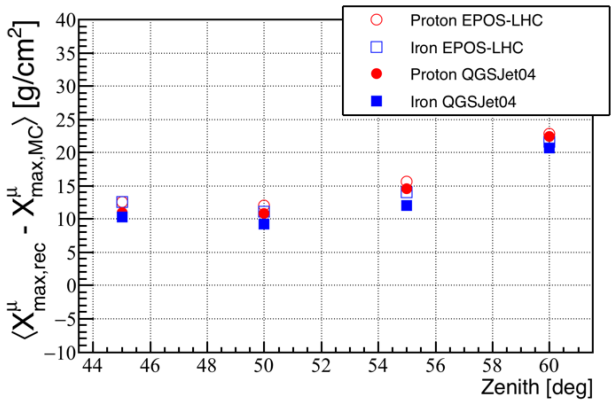

Figure 6.4: The muon time model bias evaluated for each primary and model as function of the zenith angle.

Fig. 6.3 shows the bias obtained for each primary and hadronic model, as a function of the logarithm of the primary energy (8 bins of Δlog(E/eV)=0.1) for two angular ranges [$45° - 55°$] (panel a) and [55°-65°] (panel b). Averaging on mass and models, the bias amounts to 11 and 17 g/cm^2 in the two zenith ranges respectively and does not depend on the energy. Fig.6.4 better displays the angular dependence of the bias due to the muon time distribution model: it almost doubles from 45° to 65°, going from 12 g/cm^2 to 22 g/cm^2.

6.2 Parametrisation of the muon kinematical delay

In Sec. 6.1, a relation has been derived between the muon delays and the corresponding production points (Eq. (6.7)). The kinematical delay can not be evaluated directly, because the water Cherenkov stations of the SD can not measure particle energies. This requires therefore the study of a parametrisation at MC level as a function of known variables. In [130], a parametrisation was studied for large distances from the core and

for old hadronic interaction models. However, due to the different angular and distance ranges considered in the current analysis and thanks to the possibility to exploit more up-to-date post-LHC models, a revaluation of the parametrisation was needed. A multi-parametric fit has been realised, in order to take into account different correlations among the measured variables: the kinematical delay dependence on the distance from the shower core r, on the zenith angle θ and on the muon production altitude z_m. In addition, to include the effect of different masses and models on the kinematic delay, the study has been performed on a mixed sample of proton and iron primaries (50%p-50%Fe) for both post-LHC models (50%QGSJetII-04-50%EPOS-LHC). The parametrisation has been tuned between 45° and 65° and for a given energy, $\log_{10}$(E/eV) = 19.55, since the kinematic delay does not depend significantly on the primary energy. In the following, the numerical result of this multi-parametric fit is shown:

$$\begin{aligned} t_\epsilon = 53.15 - 75.66 * (z_m - \Delta)_n + 77.4 * z_m^2 + 49.71 * r_n \\ -73.93 * (z_m - \Delta)_n^3 - 46.47 * r_n * (z_m - \Delta)_n + 5.195 * \theta_n \\ -7.159 * (z_m - \Delta)_n * \theta_n + 30.84 * (z_m - \Delta)_n^4 \\ -1.102 * (z_m - \Delta)_n^2 * \theta_n - 1.427 * r_n * (z_m - \Delta)_n^2 \end{aligned} \tag{6.9}$$

The muon production height z_m is evaluated by using Eq. (6.6). r_n, $(z_m\text{-}\Delta)_n$ and θ_n are the normalised variables for the core distance, the muon altitude and the zenith angle, respectively:

$$\begin{aligned} r_n &= 1 + 2 * (r - 4000)/(4000 - 1000); \\ (z_m - \Delta)_n &= 1 + 2 * ((z_m - \Delta) - 40000)/(40000 - 6.59); \\ \theta_n &= 1 + 2 * (\theta - 64.78)/(64.78 - 55.03); \end{aligned} \tag{6.10}$$

The performance of the parametrisation has been tested by comparing it with the kinematical delay evaluated using the MC muon energies. The latter will be indicated as *true* kinematical delay, being our reference. Fig. 6.5 shows the studied parametrisation (empty dots) and the true kinematical delay (full dots), as a function of the zenith angle (top panels), of the core distance (middle panels) and of the difference $(z_m - \Delta)$ (bottom panels), for proton EPOS-LHC (left panels) and iron QGSJet-04 (right panels). The results are shown for proton EPOS-LHC and iron QGSJet-04 because they represent the two extreme cases for the MPD analysis, giving the largest and the smallest values of X^{μ}_{max} respectively (see for example Fig. 5.8).

As already shown in Fig. 6.2, the kinematical delay increases with the core distance. This is not easy to understand, because near the core on average muon energies are larger and one would expect a lower kinematic delay. However, for small core distances the spread on energy is larger and the kinematical delay is dominated by low energy muons. Following the same arguments, it is simple to understand how this delay increases considering muons produced closer to the ground, because they have lower energies. In addition, inspecting Fig. 6.5, one can also see that the kinematic delay depends on the zenith angle. This reflects the fact that the energy spectrum of muons which arrive at ground level depends on the zenith angle and on average more vertical showers have lower energy muons [131]. Comparing the true kinematical delay (full dots) with the parametrisation (empty dots), one can conclude that all these dependences are reasonably well reproduced. For very large distances (r>3000m), the parametrisation is overestimated, especially for protons. However, the number of muons at these distances

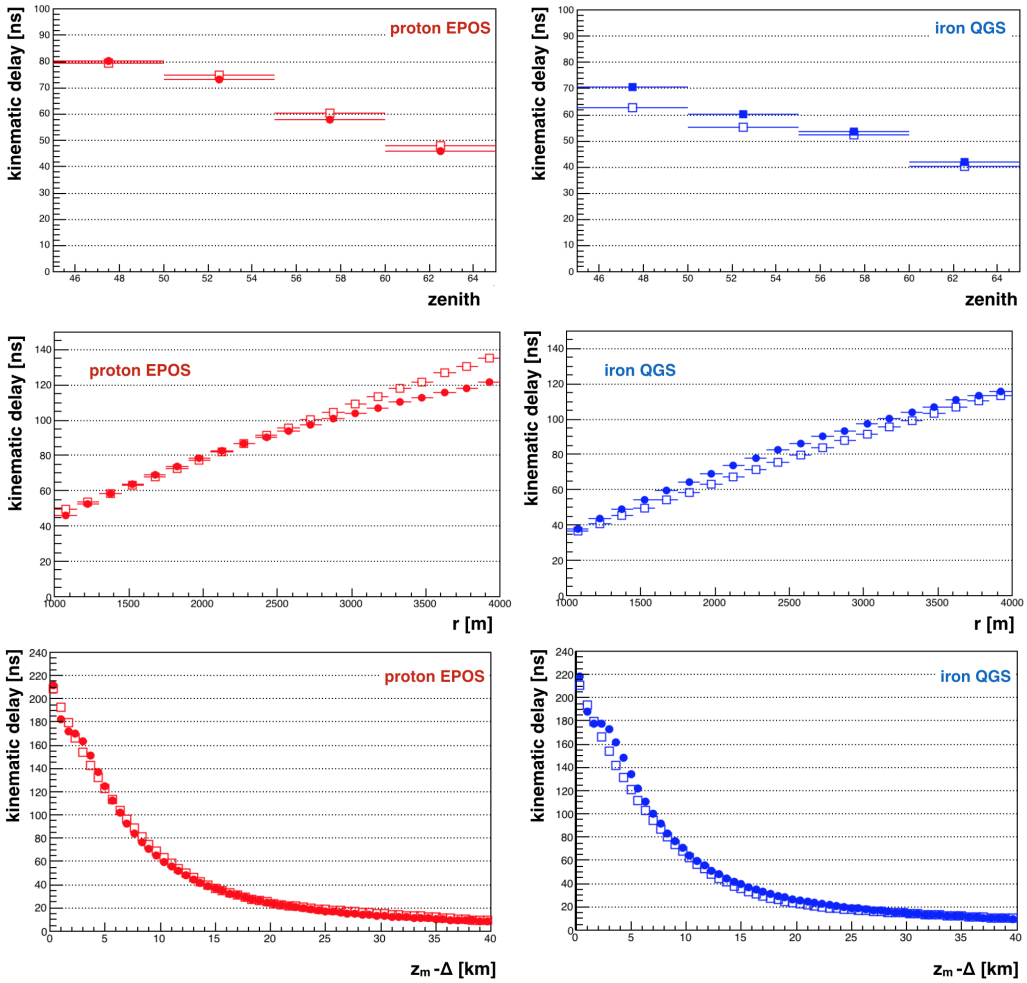

Figure 6.5: The true (full dots) and the parametrised (empty dots) kinematic delay as a function of the zenith angle (top panels), distance from the core (central panels) and production height (bottom panels) for proton EPOS-LHC (left panels) and iron QGSJetII-04 (right panels).

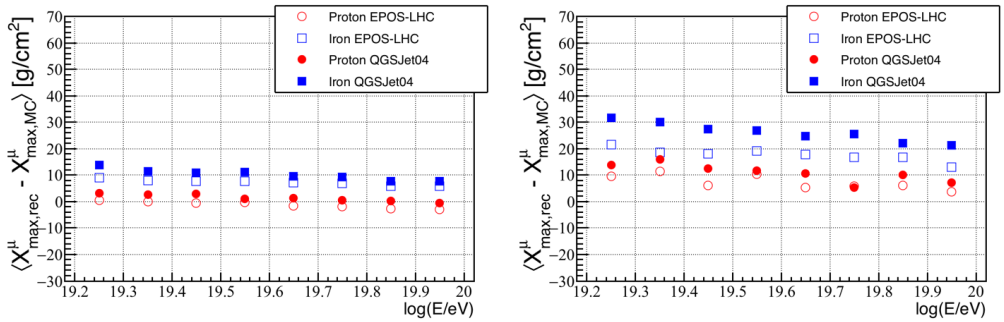

(a) (b)

Figure 6.6: The bias due to the time model including the kinematic delay parametrisation, evaluated for each primary and model as a function of the energy for [45°-55°] (panel a) and [55°-65°] (panel b).

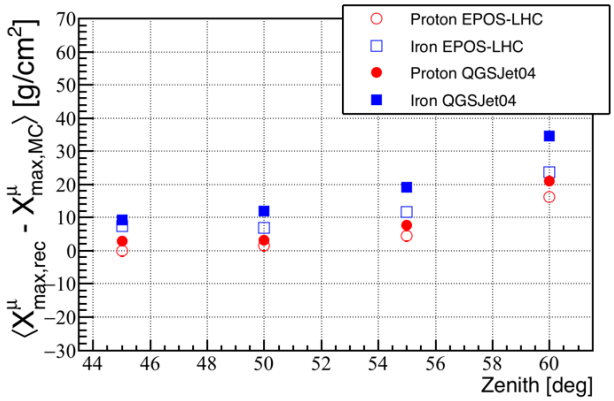

Figure 6.7: The bias due to the muon time model including the kinematic delay parametrisation as a function of the zenith angle.

is less than 1% of the total number, thus not affecting the MPD reconstruction.

Bias of the muon kinematical delay parametrisation

The impact of this new kinematical delay parametrisation on the MPD evaluation has been studied at generation level. In this case $X^{\mu}_{max,Rec}$ is reconstructed using the relation of Eq. (6.7) and the parametrised t_{ϵ} of Eq. (6.9). The results are shown in Fig.6.6, as before as a function of the logarithmic energy and in the two zenith intervals. The bias amounts to about 5 and 15 g/cm^2 at low and high zenith angles respectively. The energy dependence stays within 5 g/cm^2 at low angles, while it is between 5 and 11 g/cm^2 in the highest angular range. Despite the tuning of the kinematic delay parametrisation on a mixed sample, a bias due to the mass and model is still present. The maximum bias difference in the extreme cases of proton EPOS-LHC and iron QGSJetII-04 is about $\pm$ 8 g/cm^2 and $\pm$ 13 g/cm^2 in the zenith angle ranges [45°-55°] and [55°-65°] respectively.

Fig. 6.7 shows the evolution with the zenith angle of the bias due to the time model, including the kinematic delay parametrisation. A larger contribution from the models with respect to the mass appears for increasing angles.

6.3 MPD reconstruction with the SD

So far the MPD reconstruction has been performed at generation level with CORSIKA simulations. The situation is of course more complicated. Therefore, in the following the study of the method will be focused on Monte Carlo when also the detector is simulated, in order to face the realistic conditions of the measurement. This level of the analysis will be called *detector level*, in order to distinguish it from the generation level of the simulation.
The reconstruction of the MPD distribution at detector level is a combination of different steps, which can be summarised as follows:

- step 0: correction for a problem found on MC simulations, which affects muon delays (Sec. 6.3.2);
- step 1: removal of the electromagnetic component in order to isolate the muon signal only (Sec. 6.3.3);
- step 2: evaluation the production depth for each muon, considering the SD stations with r>1200 m, and construction of the MPD profile for a given event (Sec. 6.3.6);
- step 3: fit of the MPD profiles in order to extract the physical information from the distributions (Sec. 6.3.7).

All the points cited above have been specifically developed with the aim of deriving a reliable MPD reconstruction in the extended energy, angle and distance ranges declared in the introductory remarks and motivated in Sec. 6.3.1.
In Sec. 6.3.8, I will focus on the the performance of this method, which is fundamental to estimate the systematic uncertainties associated to the reconstruction of the MPD maximum.
The whole reconstruction chain discussed in the following will be applied to real data, except for the correction at the step 0, which is only used for solving a problem on the MC simulations at detector level.

6.3.1 Applicability ranges of the analysis

The MPD properties have been fully investigated at generation level (see Chapter 5) and the evaluation of MPD starting from arrival times of muons has been described (see Sec. 6.1 and Sec. 6.2). We have therefore all the elements to understand how to select the applicability ranges of this analysis. It has been demonstrated that there is a physical angular limit on the observation of X^{μ}_{max} and this is $\simeq 45°$. For lower zenith angles, the shower has not reached its maximum when it impacts on the ground, considering the Pierre Auger Observatory altitude level. The upper limit of 65° is not physical and it is rather due to the kind of reconstruction that should be used (for example, for larger zenith the geomagnetic field effect on muon time delays can not be neglected).
The choice of the lower limit r_{cut} =1200 m for the muon sampling region is motivated by various reasons. The first one is related to the uncertainty on each X_{μ} contributing to the full MPD distribution [121]. This uncertainty can be calculated using Eq. (6.6)

and converting z_μ to X_μ (Eq. (5.1)) assuming the atmospheric density profile $\rho(z) = \rho_0 e^{-\frac{z cos\theta}{h_0}}$:

$$\delta X_\mu = \frac{2X_\mu h_0}{r^2 \cos\theta} ln^2 \frac{X_\mu \cos\theta}{h_0 \rho_0} c\delta t \tag{6.11}$$

where h_0 is the average height at which the first muon is produced, ρ_0 is atmosphere density at that height and r is the distance from the core. δt is the resolution in the FADC sampling of the time distribution of the shower particles in each SD station and it is δt=25 ns.
One can note that the reconstruction uncertainty δX_μ decreases quadratically with the core distance. In addition, the total uncertainty in the determination of the MPD maximum decreases with the number of muons, N_μ, which is a function of the mass of the primary particle: heavy primaries have a larger number of muons with respect to light nuclei. The lower limit of r must be thus carefully chosen, in order to avoid possible biases in the selection of heavier nuclei.
This limit is also related to the muon kinematical delay contribution, t_ϵ. As explained in Sec. 6.1, t_ϵ is not negligible near the core and it is necessary to keep it as a small fraction of the geometrical delay t_g, in order to avoid the introduction of further dependencies on simulations. r_{cut} =1200 m implies that t_ϵ is less than 20% of t_g (the other contributions to the total delay are of the order of a few percent).
As regards the energy range, this analysis is applied to events with log(E/eV)>19.2 ($\simeq$ 15 EeV) and this is essentially related to the statistics of muons at disposal for the MPD reconstruction. As explained in Sec. 2.1.2, N_μ increases with the energy, but at detector level this number is not very large. This is due to the separation between SD stations (1.5 km) and to their finite collecting surface. N_μ is further reduced by the distance cut. For the chosen energy range, the lowest number of muons at the detector level corresponding to the lowest energies is sufficient for a reliable reconstruction of MPD profiles (we have approximately $N_\mu \simeq 15$ for an event with 15 EeV).

6.3.2 Step 0: resampling correction to simulations

The simulations used in this work are corrected in order to solve a problem which has been highlighted on the simulated muon arrival times at the detector level [133]. Before to describe the issue and how it can be solved, it must be clear that the evaluated correction has been applied only on simulations and not on real data.
MC simulations of EAS are produced exploiting the thinning algorithm. This means that only a certain fraction of the original huge amount of secondary particles is followed. This subsample of secondary particles with suitable statistical weights allows to estimate the longitudinal and the lateral development of an EAS. The benefits are a reasonable CPU time and a limited storage for the simulations.
On the other hand, going at the detector level, the particles falling on the SD stations are very few and do not describe the actual flux. In order to cope this aspect, the *resampling* (or *un-thinning*) algorithm is implemented, allowing the regeneration of particles reaching the detectors. As extensively described in [132], it is based on the delicate choice of a resampling area, in which particles are cloned according to their statistical weight. This area should be small enough to reproduce the physical properties of the particles, but large enough to avoid statistical fluctuations. The resampling area is defined by a radial distance δ and an angular aperture α from the detector position (see the grey area sketched in Fig. 6.8).
The simulations used in this work were produced with a thinning factor of 10^{-6} and then generated at detector level with a resampling area of α=8.6° and δ=10%. While it was

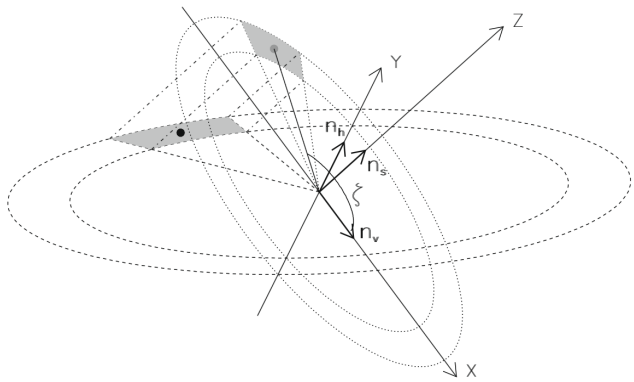

Figure 6.8: Sketch of the shower reference frame: Z is along the shower axis, XY plane is the shower plane. The sampling region around the detector (black point) is in grey: it is the projection onto the ground, along Z-axis, of a region in the shower plane (X, Y) delimited by a circular crown and an angular sector [132].

shown that the choice of the thinning level does not affect the MPD distribution [134], the effect of the resampling turned out to be important [133]. It has been demonstrated that the non-optimal choice of the resampling area has introduced an underestimation of the muon delays. This underestimation increases with the distance from the core and does not depend on the nature of the primary, its energy and hadronic model. This effect has been evaluated on the whole angular range of this analysis. In particular, as done in [135], we reproduced the reconstruction conditions at generation level, by integrating only muons falling in the crowns defined by :

$$\frac{|r_d - r|}{\delta\, r_d} \tag{6.12}$$

r is the distance from the shower core, r_d assumes discrete values between 1000 and 4000 m from the core and δ=0.1. In this condition, the average muon delays, $\langle \tau_{rec} \rangle$, as function of distance have been evaluated. The crucial point consists in the choice of a different radial distance δ=0.01. This condition is considered to better reproduce the true situation for muon delays distributions [134]. In this case, we found averaged delays, that we call $\langle \tau_{true} \rangle$ and the resampling correction has been estimated as the difference:

$$\Delta\tau = \tau_{rec} - \tau_{true} \tag{6.13}$$

The results are shown in Fig. 6.9, for proton QGSJetII-04 and log(E/eV)=19.55 in two angular bins: [45°-55°] and [55°-65°]. The underestimation depends on the zenith angle and it is larger for smaller angles. In addition, it increases with the distance from the shower core, passing from about 5 ns at 1200 m to 30-50 ns between 3000 m and 3500 m, depending on the zenith angle.
The reconstructed muon delays have been corrected exploiting the fits shown in Fig. 6.9. Having derived the muon delay underestimation at generation level, the correction to the delays has been applied muon by muon at detector level, where the resampling problem appears. After the correction, the reconstructed MPD maximum $X^{\mu}_{max,Rec}$ increases of about 10 g/cm^2 at low angles and 15 g/cm^2 at high angles.

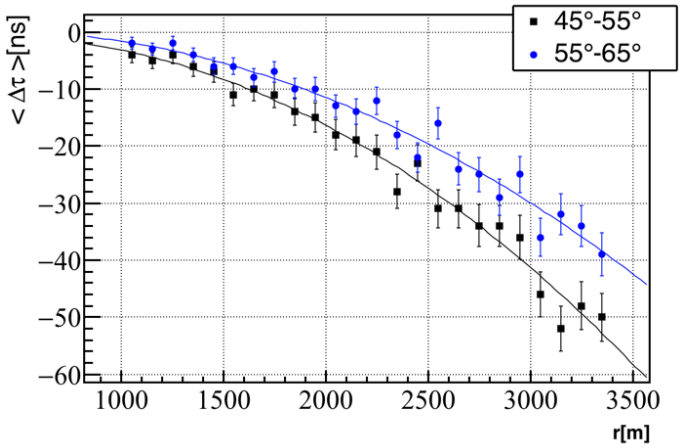

Figure 6.9: Resampling correction evaluated as function of core distance, in two zenith ranges (proton showers, QGSJET-04 model, log(E/eV)=19.55). The quadratic fit used for the correction is shown.

The described correction must be applied only to simulations, unlike the other steps that have been listed in the previous sections of this chapter. The reconstruction on X^{μ}_{max} has been evaluated by varying the resampling correction of each zenith range within the errors. The difference in the average reconstruction bias of X^{μ}_{max} is less than ≈ 1 g/cm^2, therefore giving a negligible contribution in terms of systematic uncertainty.

6.3.3 Step 1: removal of the electromagnetic background

The time traces measured in the SD stations are due to both electromagnetic particles and muons. A fundamental ingredient for the MPD reconstruction is therefore the extraction of the muonic signal. Possible trigger fluctuations and accidental signals are minimised by a simple requirement on the minimum signal of each station (S > 3 VEM), while the smoothing algorithm (Sec. 6.3.4) and a time cut (Sec. 6.3.5) are applied in order to remove the electromagnetic background. In particular, for each event which passes the selection in energy and zenith angle, these procedures are performed for each SD station between 1200 m and 4000 m.
It is worth mentioning that under the conditions of the published MPD analysis [121], i.e. inclined events [55°-65°] and large distances from the core (r>1700m), the electromagnetic contamination can be removed by a simple threshold cut, being most of it absorbed in the atmosphere. However, this approach can not be applied when lower zenith angles and distances from the core are considered. In this case, the electromagnetic background is not negligible and using a simple threshold cut would result in a large bias on the reconstructed maximum of the MPD distribution.

6.3.4 The smoothing

The estimation of the electromagnetic component is performed by using the smoothing algorithm developed for the MPD reconstruction in [127]. It exploits the different characteristics of the time structure of the electromagnetic and muonic signals. The first one is smooth and typically spread over a large time interval, because of the high density and

low energy of electromagnetic particles (10 MeV on average). Instead, the second one is characterised by peaked signals, due to low density and high energy of the muons (1 GeV on average). Top panels of Fig. 6.10 show these features for the signal a simulated proton event, at 50° and 30 EeV, taken as example. The green histogram and the red histogram are respectively the time distribution of the electromagnetic and the muonic component of the FADC trace, considered for one SD station which participates to the reconstruction of the simulated event. Each time bin have a width of 25 ns, given the sampling rate of 40 MHz.
Many kinds of smoothing techniques exist. One of them is based on symmetric polynomial filters applied to equidistant measured steps. An interval, called *convolute range*, is moved stepwise through the pattern and the central point of the interval is replaced by the value of a least square polynomial calculated from the other points in the interval. For this analysis, a polynomial of first degree is used and this is just the so-called *moving average*.
More specifically, for the MPD reconstruction, the smoothing algorithm is applied, station by station, in a convolute range called N_{bin}, which depends on the zenith angle of the event. If one considers the smoothing average in the frequency domain as a low-pass filter, a large convolute range will be enough to follow the low electromagnetic signal in inclined showers. On the contrary, in vertical showers, which have a larger background, a narrow window is needed. The convolute range has been carefully tuned by minimising the relative difference between the original electromagnetic signal from the simulation and the one obtained from the smoothing method.
The procedure to derive the electromagnetic and the muonic component in a time interval T divided into N_{bin} equidistant bins is thus the following:

- for each i_{th} time bin, the total signal averaged over the 3 PMTs, $S_{tot}(i)$, is evaluated.
- The smoothed trace is then derived by substituting each bin content with the average signal value estimated in the range [i-N_{bin},i+N_{bin}] and assigned to the electromagnetic component $S^{EM}_{Smoo}(i)$.
- The muon signal in the considered i_{th} time bin, if any, will be given by the positive difference:

$$S^{\mu}_{Smoo}(i) = S_{tot}(i) - S^{EM}_{Smoo}(i) \tag{6.14}$$

Few iterations of the procedure are enough to reach convergence.
The bottom panels of Fig. 6.10 show, for the same simulated event aforementioned, S_{tot}, i.e. the time distribution of the total signal trace (black histogram) and S^{μ}_{Smoo}, i.e. the time distribution of the total signal after the smoothing procedure (blue histogram). Comparing the latter with the pure muonic signal reported on the right top panel, one can see how the position of the muon peaks and the signal intensity are reproduced well enough (there is a small residual electromagnetic contamination which is removed with a further procedure which will be explained in Sec. 6.3.5).
The performance of the smoothing method has been quantitatively evaluated by checking the reconstruction quality for both the muon time distribution and the muon signal. As regards the accuracy of the muon time distribution reconstruction, the relative differences Tx = (Tx_{Smoo}-Tx_{MC})/T x_{MC} has been evaluated. Tx is the time at which the muon signal reaches x% of the total one, Tx_{Smoo} refers to the smoothed signals, Tx_{MC} to the MC muon signal. Fig. 6.11 displays this difference at 10% (left panels), 50% (middle panels) and 95% (right panels). T10, T50 and T95 are evaluated for each SD station and an average value is then considered for each event. The results are shown as a function

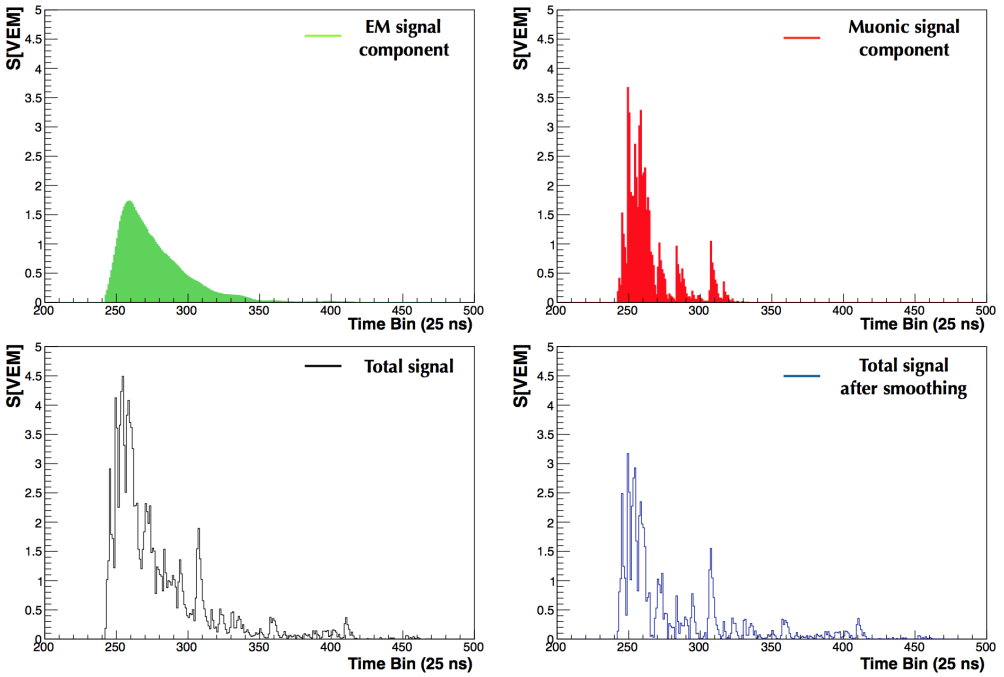

Figure 6.10: Signal components recorded with one SD station for a simulated proton event at 50° and 30 EeV. The green histogram (top left panel) and the red histogram (top right panel) are respectively the time distribution of the electromagnetic and the muonic components of the FADC trace. The black histogram (bottom left panel) is the total signal distribution and the blue one (bottom right panel) is obtained from the total signal after the smoothing procedure.

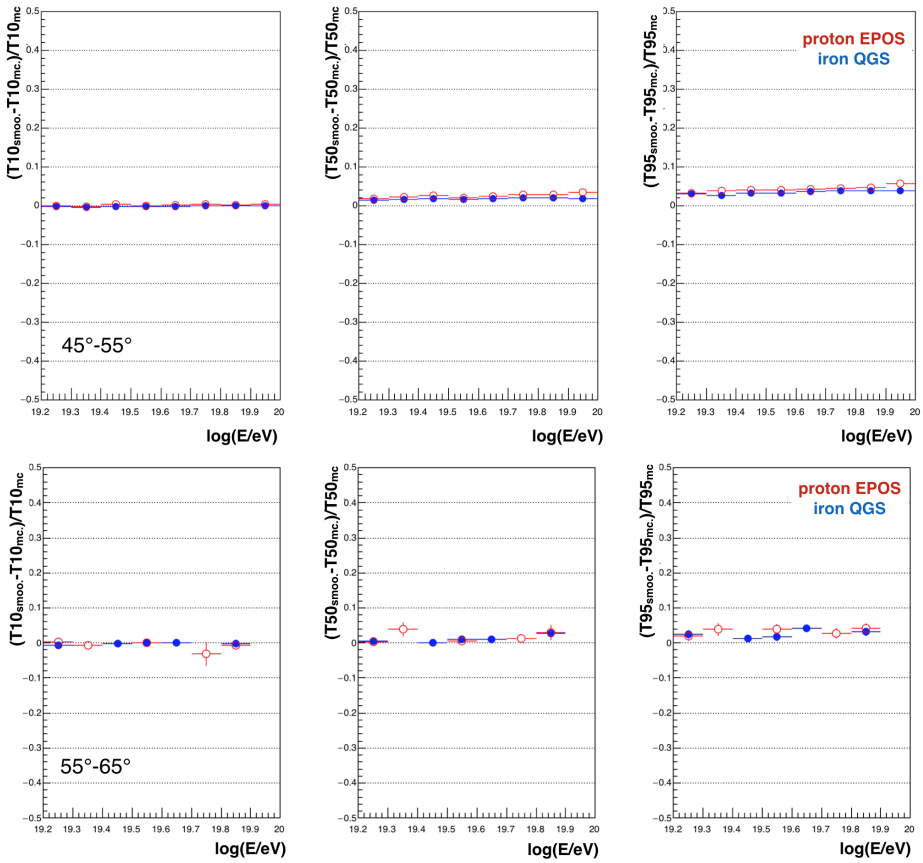

Figure 6.11: The accuracy of the smoothing method in determining the muonic time distribution as a function of energy, for [45°-55°] (top) and [55°-65°] (bottom). The relative differences in T10, T50 and T95 (see text for the definition) are shown by columns, from left to right and are evaluated for proton EPOS-LHC (red dots) and iron QGSJetII-04 (blue dots).

of the logarithmic energy, for the angular ranges [45°-55°] (top panels) and [55°-65°] (bottom panels), for proton EPOS-LHC (red dots) and iron QGSJetII-04 (blue dots). As before, we use these two as the extreme cases of the possible combinations model-mass.
The relative difference is below 1% for T10, below 4% in the case of T50 and below 6% in the case of T95, for both angular ranges and it does not depend significantly on the energy. Therefore, the smoothing technique allows to derive the muon time distribution from the total trace, with a good accuracy in the whole energy and angular range of this analysis.
For what concerns the accuracy in the evaluation of the muon signal intensity, Fig.6.12 shows the relative difference between the reconstructed muon signal, S_{Smoo} and the MC one, S_{MC} as a function of the energy, for zenith bins [45°-55°] (left panel) and [55°-65°] (right panel) and again for proton EPOS-LHC (red dots) and iron QGSJetII-04 (blue dots) simulated showers. For inclined events, the method accuracy stays within 5%, with a small (few %) dependence on energy and mass. In the lower zenith angle bin, on the contrary, the accuracy of the method is about 10% and depends on the shower energy,

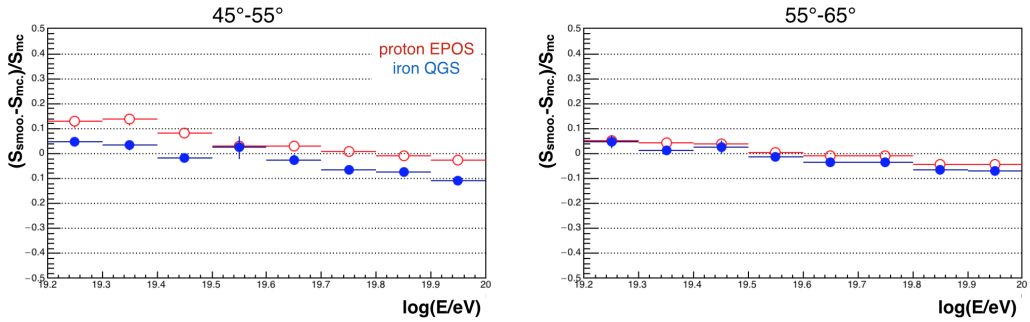

Figure 6.12: The accuracy of the smoothing method in determining the muonic signal as a function of energy, for [45°-55°] (left panel) and [55°-65°] (right panel).

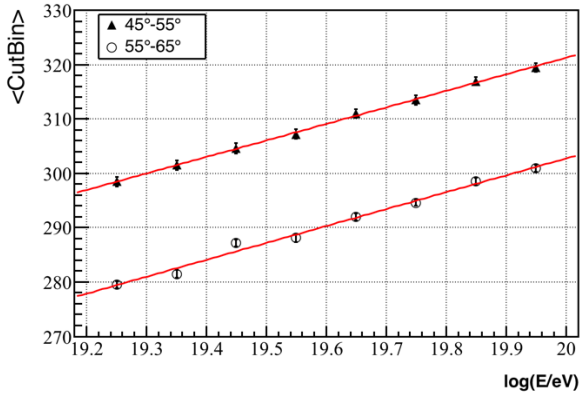

Figure 6.13: Average time cut bin as a function of the energy and for the two zenith bins [45°-55°] and [55°-65°]. The results are obtained averaging on those obtained for the different primaries and hadronic models used in this work.

mass and models. The effect is due on the one hand to the larger number of particles entering the stations and producing overlapping signals, and on the other hand to the increase of the electromagnetic component. However, the reconstruction of the muonic time structure is relevant for deriving the MPD, while the muon signal intensity enters the MPD profile reconstruction as a weight only and a 10% accuracy is considered satisfactory.

6.3.5 The time cut

Fake spikes mimicking real muons can affect the smoothing performances, leading to an overestimation of the muonic signal. Besides artificial ones, due e.g. to bad behaviour of PMTs, which can be removed in the first steps of the analysis, more important and unavoidable are the spikes due to high energy photons and electrons (>300 MeV). This background turns out to mostly affect the tail of the signal time distribution recorded at the SD stations, where its relative contribution increases with respect to the muonic one. This is reflected on the MPD distributions, resulting in a distortion of the tail of the reconstructed profile. The effect increases with the primary energy and it is more

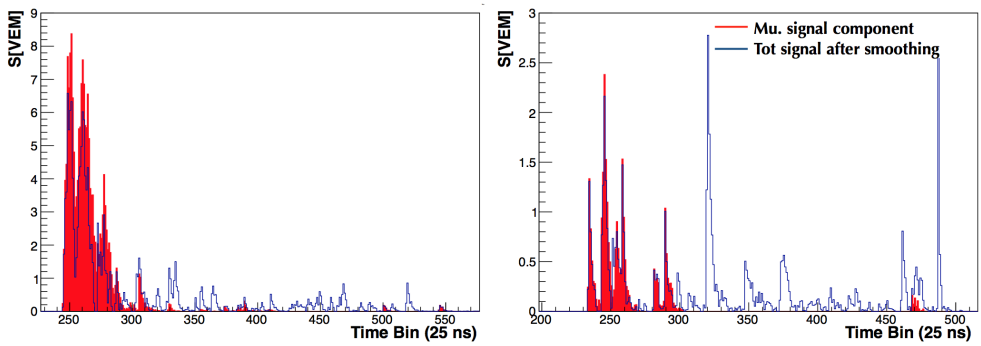

Figure 6.14: Examples of signal time distributions for two SD stations, one near the core at 1300 m (left panel), the other far from the core at 2000 m (right panel), for a simulated proton event with energy 88 EeV and zenith angle 45°. The trace in red is the simulated muonic component of the trace, the blue one represents the total trace after the smoothing algorithm. See text for details.

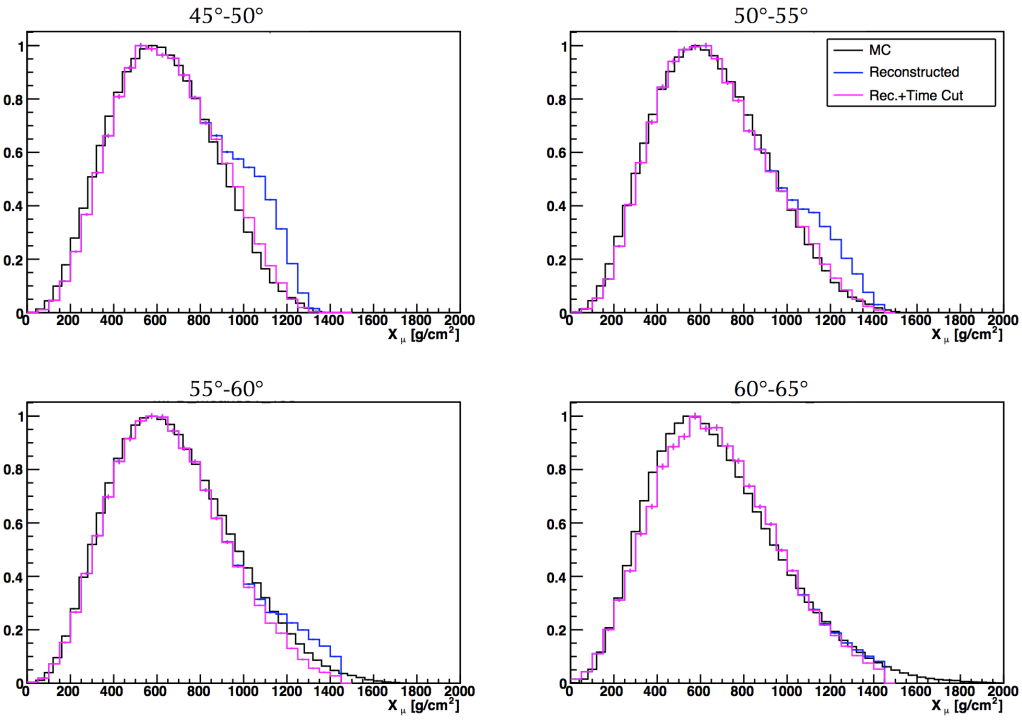

Figure 6.15: Average MPD distributions obtained from proton events at 30 EeV at MC level for four zenith intervals. The black line refers to average profiles evaluated at generation level using X^{μ}_{MC} information. The blue and purple average MPDs are calculated at the detector level after the whole reconstruction chain (including the time offset that will be described in the next section 6.3.6), respectively without and with the time cut. See text for details.

important at low zenith angles, because the EM component is less absorbed. In addition, MPD distributions of protons are more distorted because the corresponding showers have a smaller number of muons with respect to iron-induced ones [127].
This physical, unavoidable background must be removed and a cut on the signal SD trace has been studied as a function of the energy and the zenith angle of the event. The cut has been tuned according to the MC simulations in order to keep more than 85% of the muon signal, thus avoiding an unreliable MPD reconstruction. In particular, the cut has been estimated by evaluating the difference between the MC muon trace (of course unknown on real data) and the total trace after the smoothing procedure. The cut is set at the time bin of maximum overestimation of the MC muon signal. An average is then evaluated based on the 4 different combinations of mass and models considered in this work. It is shown in Fig. 6.13 as a function of the logarithmic energy and for the two zenith ranges [45°-55°] and [55°-65°]. The best fit used for the cut is also displayed and its numerical results for the two angular bins are:

$$\langle \mathrm{CutBin} \rangle_{50^\circ} = -268.8 + 30.4 \cdot \log_{10}(\mathrm{E/eV}) \tag{6.15}$$

$$\langle \mathrm{CutBin} \rangle_{60^\circ} = -318.9 + 31.08 \cdot \log_{10}(\mathrm{E/eV}) \tag{6.16}$$

It can be seen that the cut bin spans from the 300th bin to the 340th bin at low zenith angles. It increases with the energy since the trace length increase with it. It is smaller for inclined events, between the 280th bin and the 300th, since the time distributions are narrower, for both the muonic and the EM components.
Fig. 6.14 better clarifies this method. It reports an example of signal time distributions for two out 14 SD stations which are triggered by a simulated proton event at 88 EeV and 45° and which satisfy the requirement on the signal S > 3 VEM. The plot on the left refers to one of these 14 stations, which is near the core (1300 m). For the same simulated event, the plot on the right shows the signal of a station farther from the core (2000 m). In particular, the red histogram represents only the pure muonic MC component of trace, whereas the blue one is the total trace after the smoothing algorithm. The contamination from the high-energy electromagnetic background is evident for both SD stations, but thanks to the time cut here studied, the signal after the 320th bin is removed, according to Eq. (6.15) and therefore according to the energy and zenith angle of the event.
Fig. 6.15 displays the effect of the time cut on average MPD distributions simulated at detector level after the whole reconstruction chain. Note that a time offset is also applied, as will be discussed in Sec. 6.3.6. The MPD distributions are reported for four zenith bins, [45°-50°], [50°-55°], [55°-60°], [60°-65°] , without (blue line) and with the cut on the trace of Fig. 6.13 (purple line). The average profiles are compared with the simulated ones at generation level (black line). The distortion caused by the high-energy EM background is clearly visible, especially at low zenith angles, where it affects the tail of the distributions. When the time cut is applied, the distortion is efficiently removed.

6.3.6 Step 3: evaluation of the MPD distributions

Once the muonic signal has been extracted, for each i_{th} time bin of each SD station of the selected event, the muon arrival time is estimated with respect to the shower front by using the expression:

$$t = t_0 + (i - i_0) \cdot 25 + 12.5 \text{ ns} \tag{6.17}$$

where t_0 is the arrival time of the shower plane and i_0 is the start bin of the trace. The factor 12.5 indicates that the arrival time is considered with respect to the centre of the

time bin. The muon delay t is corrected for the resampling problem described in Sec. 6.3.2 (step 0). It is then assumed that the muon delay t is only geometrical and an approximated production height z is estimated. The approximated z is used in order to evaluate the kinematical delay of the parametrisation described in Sec. 6.2. The muon time distribution model (Sec. 6.1) is exploited for the estimation of the muon time delays as follows:

$$z = \frac{1}{2}\left(\frac{r^2}{c(t - t_{\epsilon} - t_{\mathrm{Off}})} - c(t - t_{\epsilon} - t_{\mathrm{Off}})\right) + \Delta - z_{\pi} \tag{6.18}$$

This expression is different from Eq. (6.7), because a time offset t_{Off} has been introduced. Its value has been tuned on simulations: it amounts to 60 ns and and it is constant in the whole energy and angular range of this analysis. It is used in order to globally correct the MPD for the different effects which are introduced by the detector. In fact, the latter can contribute to distort the reconstruction of the MPD with respect to the ideal situation at generation level. First of all, as already anticipated, at generation level all muons between 1200 m and 4000 m are used to build the MPD distribution, while at the detector level only muons arriving on SD stations are used. The discrete sampling at ground and the finite collecting area of the SD stations (10 m^2 for vertical events) of course affect the MPD reconstruction, strongly reducing the number of collected muons. In addition, the uncertainty on the evaluation of the muon production altitude is related to the detector time resolution, as shown in Eq. (6.11), on the smearing of the muon signal due to the light propagation inside the SD station and on the electronics response.
The full MPD histogram is finally obtained by integrating the MPD profiles reconstructed from each SD station. The overall result of the listed detector effects can be seen in Fig. 6.16, where average MPD profiles after the reconstruction chain (green distributions) are compared with those obtained at generation level (black distributions). The example shown in the figure regards proton showers simulated at 30 EeV with four different zenith angles: in the whole range, the MPD distributions are clearly shifted to higher X_{μ} values due to detector distortion. A correction of the detector effects is obtained by introducing the time offset. Its effect is shown in the figure with the purple histograms: a nice agreement with the ideal Monte Carlo profiles is obtained in the whole considered angular range.

6.3.7 Step 4: fit procedure and quality cuts

As described in chapter 5, in order to evaluate X^{μ}_{max} from the MPD distributions, it is necessary to apply a fit procedure on event-by-event basis. The chosen function for this work is the *Universal Shower Profile* (USP) function (see Eq. (5.2)), which describes the distribution by means of 3 parameters with a clear physical meaning: X^{μ}_{max}, L (the width of the profile) and R (the asymmetry of the profile). The fit is performed, both at generation and at detector level, in a limited range of atmospheric depths, between 0 and 1200 g/cm^2. This interval contains the whole set of possible values of X^{μ}_{max}.
At generation level, a log-likelihood minimisation of the USP function with all parameters free is adopted to derive $X^{\mu}_{max,MC}$. This is possible because all muons arriving at ground between 1200 m and 4000 m are used to build the MPD distributions, which are therefore well sampled. At detector level, the number of muons is not large for the reasons explained in Sec. 6.3.6: they are not collected continuously because of the spacing between SD stations (1.5 km), which have a finite collecting surface. In addition, as explained in Sec. 6.3.1, a distance cut is mandatory to keep the distortions of the reconstructed MPD small, but this of course further reduces the number of muons at disposal for the reconstruction. For all these reasons, a free parameter fit at detector level does

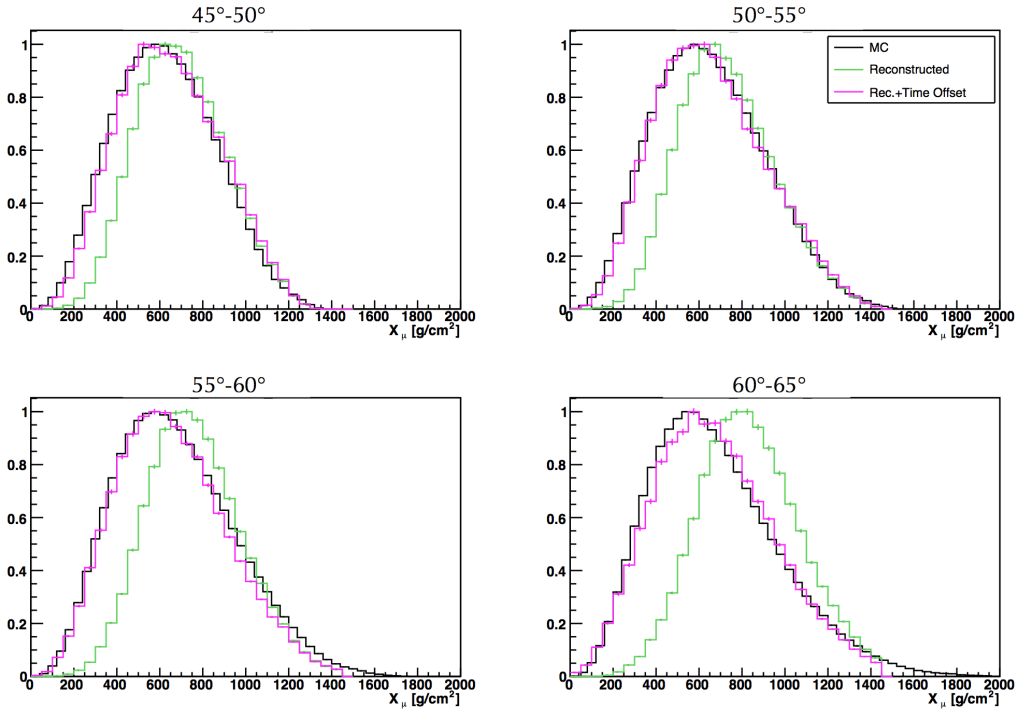

Figure 6.16: Average MPD distributions obtained from proton events simulated at 30 EeV in four zenith intervals. Black distributions refers to average profiles obtained at generation level using X^{μ}_{MC} information. Green and purple average MPDs are obtained at the detector level after the whole reconstruction chain (including the time cut described in the previous section 6.3.5), respectively without and with the time offset of 60 ns. See text for details.

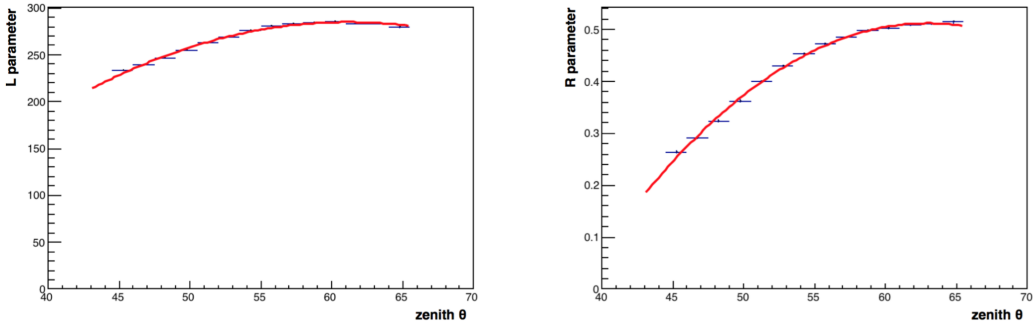

Figure 6.17: The parameters of the USP function, L (left panel) and R (right panel), are shown as a function of the zenith angle at generation level. The best fit is reported (red line) and on this basis R is fixed as a function of the angle at detector level.

not allow a realiable estimation of the shower parameters.

We therefore decide to study the evolution of the parameters R and L at generation level as a function of the zenith angle of the event. As shown in Fig. 6.17, both L (left panel) and R (right panel) increase with the angle since the MPD profiles are more asymmetric and wider for inclined events. This is more evident for proton showers and for this reason the study has been performed on a mixed sample of both proton/iron nuclei with both QGSJetII-04 and EPOS-LHC hadronic interaction models. Fig. 6.17 shows also the best fit on the parameters, which is a second order polynomial:

$$\langle \mathrm{L} \rangle = -528.5 + 26.6 \cdot \theta - 0.22 \cdot \theta^2 \tag{6.19}$$

$$\langle \mathrm{R} \rangle = -2.762 + 0.104 \cdot \theta - 0.00083 \cdot \theta^2 \tag{6.20}$$

According to these results, for each event the fit is performed by setting the starting value of the parameter L and by fixing R as a function of the zenith angle of the event. Once the fit has been performed, a set of quality cuts are applied in order to discard events for which the X^{μ}_{max} estimate is not reliable. These selection criteria are listed in the following:

- only events with at least 5 SD stations are accepted.
- The fit convergence is required.
- Events with L parameter in the range [130-415 g/cm^2] are used for the analysis. This condition allows to remove those events for which the MPD distribution is not well reconstructed in the first part or in the tail, leading to unphysical values for the parameter L. The optimal range chosen for the L parameter is a 3σ limit on its distribution for both data and simulations.
- Events with relative uncertainty $\delta X^{\mu}_{max}/X^{\mu}_{max} < \epsilon_{max}$ are accepted. This value is chosen at 3σ from the mean of the $\delta X^{\mu}_{max}/X^{\mu}_{max}$ distribution and it is reported in table 6.2. ϵ_{max} depends on the energy, since the accuracy in the estimation of X^{μ}_{max} improves with it. This is a natural consequence of the increase in the number of muons that enter the MPD distribution as the energy grows.

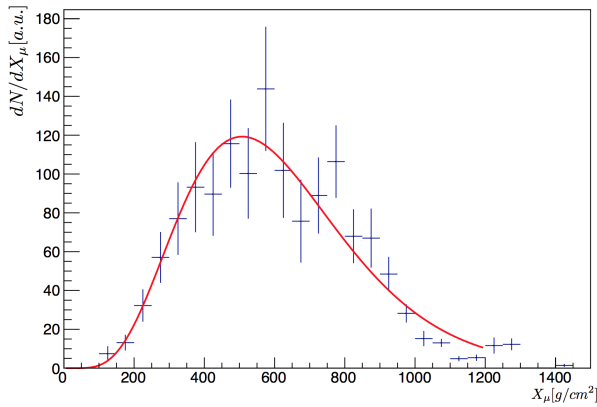

Figure 6.18: Example of a reconstructed MPD distribution for an iron QGSJetII-04 event simulated with θ=55° and energy 35 EeV. The USP fit is shown (red line).

The efficiency of the listed cuts is always above 95% for each primary and hadronic model. One has to consider that in principle a set of quality cuts could introduce a mass bias. In fact, iron showers are better reconstructed than proton ones, having a larger number of muons for a given energy. However, our procedure has been found to select proton and iron showers with about the same efficiency, being the difference within 4% on average and within 8% at the lowest energies. The systematic uncertainty related to the mass bias is therefore expected to be very small. More details about it will be given in Sec. 8.3, where all the possible sources of systematic uncertainty of X^{μ}_{max} are discussed. An example of a reconstructed MPD distribution is shown in Fig. 6.18 for an iron-induced shower simulated with QGSJetII-04 model at 55° and 35 EeV.

$\log_{10}$(E/eV)	ϵ_{max}
19.2-19.5	9%
19.5-20.	6%

Table 6.2: The maximum relative uncertainties allowed in the estimation of X^{μ}_{max}.

6.3.8 Total reconstruction bias

A fundamental step of the MPD analysis consists in the evaluation of the bias after the whole reconstruction chain. This is important for two main reasons: on the one hand it is used to correct real data in order to have an unbiased evaluation of X^{μ}_{max}; on the other hand, it allows to estimate the systematic uncertainties of the method related to the mass and models.
Therefore, the reconstruction bias has been carefully studied in order to highlight possible dependencies on the mass, the hadronic model, the energy and the zenith angle of the simulated showers. The results are reported in Fig. 6.19, as a function of the logarithm of the primary energy and for 2 zenith bins: [45°-55°] (panel a) and [55°-65°] (panel b). Again $X^{\mu}_{max,MC}$ is estimated at generation level, using the MC muon slant depths, while $X^{\mu}_{max,Rec}$ is evaluated at detector level, using all the different steps of the method described in this chapter. As shown, the final reconstruction bias depends on the energy,

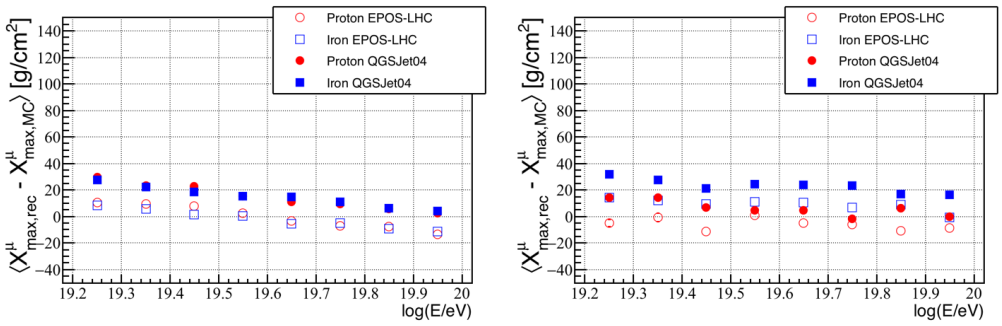

(a) (b)

Figure 6.19: Reconstruction bias of X^{μ}_{max} as a function of the logarithm of the primary energy at [45°-55°] (panel a) and [55°-65°] (panel b). The bias is shown for each hadronic interaction model and primary mass considered in this work.

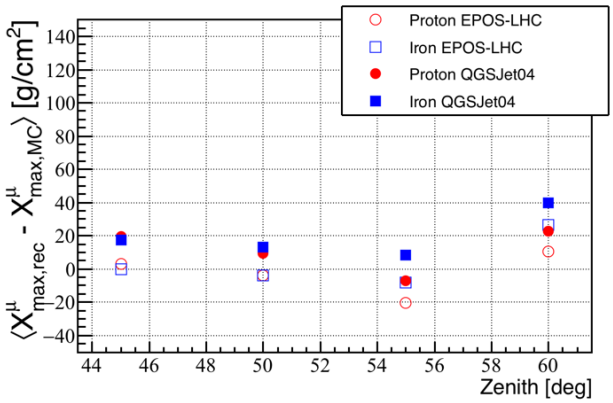

Figure 6.20: The reconstruction bias as a function of the zenith angle for proton/iron primaries and EPOS-LHC/QGSJETII-04 hadronic models. Values are integrated in energy.

	log(E/eV) 19.25	log(E/eV) 19.35	log(E/eV) 19.45	log(E/eV) 19.55	log(E/eV) 19.65	log(E/eV) 19.75	log(E/eV) 19.85	log(E/eV) 19.95
45°-50°	21	19	16	10	7	4	3	-2
50°-55°	16	11	9	6	1	-1	-5	-8
55°-60°	1	-1	-6	-6	-6	-8	-14	-14
60°-65°	25	29	25	25	25	20	25	23

Table 6.3: Reconstruction bias averaged on primaries and models for each energy and zenith bin. Values are in [g/cm^2].

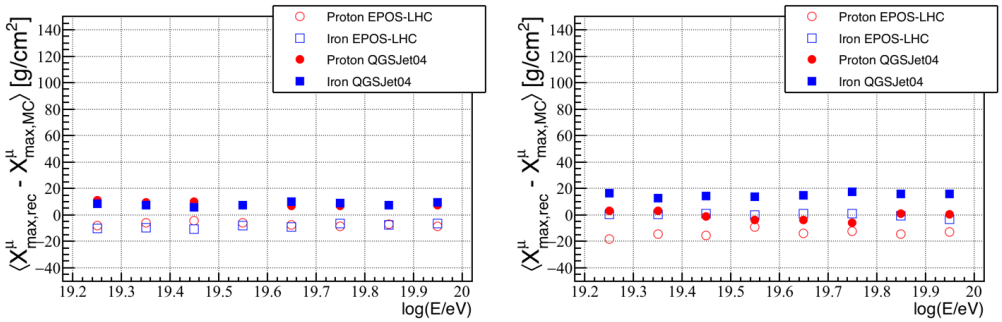

(a) (b)

Figure 6.21: Reconstruction bias of X^{μ}_{max} after the correction for its angular and energy dependence. It is shown again in two zenith ranges: [45°-55°] (panel a) and [55°-65°] (panel b), and for each hadronic model and primary mass.

especially at low zenith angles. This derives from the combination of different factors: on the one hand, at low energy, the smaller number of muons makes the reconstruction worse, on the other hand, at high energy, muons produce overlapped signals in the SD stations, especially for more vertical events, and this also generates a worse reconstruction.

As regards the angular dependence, it is better shown in Fig. 6.20. Four zenith bins have been considered: [45°-50°], [50°-55°], [55°-60°] and [60°-65°]. It can be seen that, on average, the bias ranges from 10 g/cm^2 to 24 g/cm^2 as the zenith angle increases. This observed dependence is quite compatible with the one at generation level due to the time model and the parametrisation of the kinematical delay (Fig. 6.7).

Both the energy and angular dependence of the reconstruction bias have to be taken into account. Table 6.3 displays the values used for correcting the data in order to have an unbiased evaluation of the maximum of the muon longitudinal profile. The tabulated numbers are obtained averaging the bias on the whole sample of simulations (p/Fe EPOS-LHC/QGSJetII-04), considering 4 zenith bins and 8 energy bins. The reconstruction bias has been corrected for the angular and energy dependence, according to Table 6.3, as shown in Fig. 6.21. After the correction, the bias is flat in zenith and energy and it is 0 on average, as expected. The dependence of the reconstruction performance on the mass and the model is clearly highlighted. It can be quantified by means of a quantity that we call *spread*:

$$\text{spread} = \pm(\text{bias}_{\text{Max}} - \text{bias}_{\text{min}})/2 \tag{6.21}$$

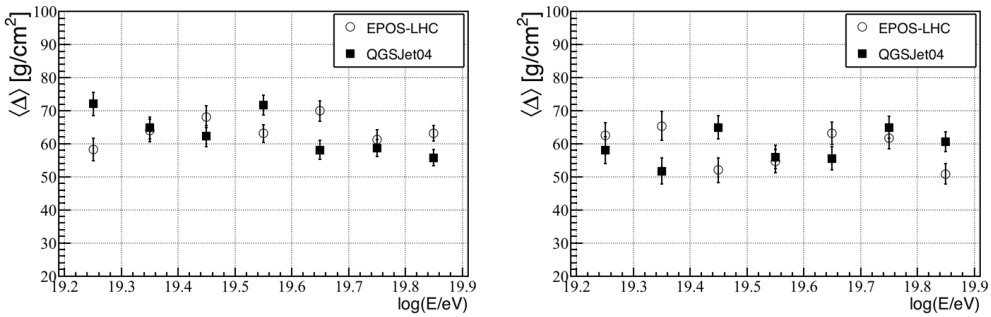

Figure 6.22: Proton-iron separation Δ evaluated after the reconstruction chain here described. The results are shown for the two hadronic interaction models EPOS-LHC and QGSJetII-04 as a function of the logarithm of the primary energy and for the two zenith bins [45°-55°] (panel a) and [55°-65°] (panel b).

bias$_{Max}$ and bias$_{min}$ are respectively the maximum and the minimum value of the bias evaluated among all the primaries and hadronic models on the energy and zenith ranges of this analysis.
It can be seen that at low zenith angles the spread is almost due only to the model and it amounts to about $\pm$11 g/cm^2. For higher angles, it increases to $\pm$18 g/cm^2 due to the non negligible contribution of the mass dependence. These numbers represent the systematic uncertainty associated to the MPD method developed in this work, which is related to the unknown mass of the primary and hadronic interaction model.
A reduction of the systematic uncertainty here described could be obtained by moving the core distance cut to r$_{cut}$=1500 m. Following this approach, the spread would be few g/cm^2 smaller, essentially because of a reduced contribution of the kinematical delay parametrisation. However such cut would result in a significant loss of events (about 50%) in the lower energy range $10^{19.2}$-$10^{19.4}$ eV. Since this option does not reduce significantly the spread and it reduces the sample at disposal for the analysis, we decided to do not exploit it.

6.4 Merit factor after the reconstruction

The MPD merit factor has been evaluated again, after the whole reconstruction chain by means of Eq. (5.3) and (5.4). The proton-iron separation Δ is shown in Fig. 6.22, whereas the merit factor D is reported in Fig. 6.23. The results are shown for the two hadronic interaction models and for the two zenith bins [45°-55°] (panel a) and [55°-65°] (panel b) as a function of the logarithm of the primary energy. It can be seen that the proton/iron separation is similar to that obtained at generation level in Sec. 5.5. On average the Δ factor is 64 g/cm^2 at low angles and 60 g/cm^2 at high angles.
For what concerns the merit factor, it worsened as expected because of the reconstruction by about a factor of 1.5, with respect the one found at generation level. On average it is 0.9 at low angles and 0.7 at high zenith angles, independently on the hadronic model, being the same the shape of the X^{μ}_{max} distributions for EPOS-LHC and QGSJetII-04. The performance of the method are not constant in energy and zenith angle and this explains

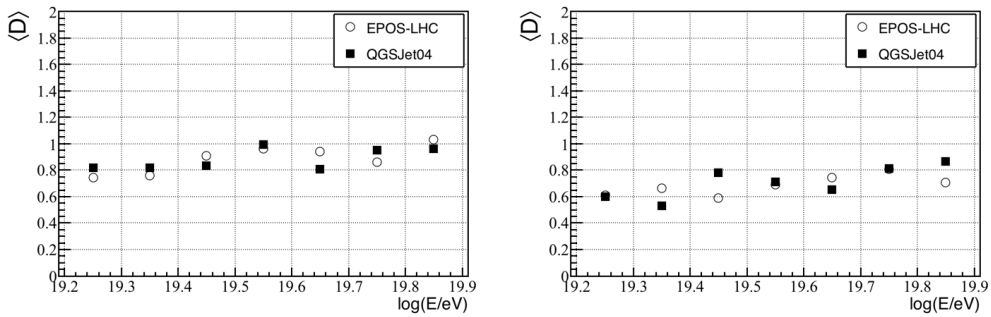

(a) (b)

Figure 6.23: Merit factor D evaluated after the reconstruction chain here described. Results are shown for the two hadronic interaction models EPOS-LHC and QGSJetII-04 as a function of the logarithm of the primary energy and for the two zenith bins [45°-55°] (panel a) and [55°-65°] (panel b).

why D slightly changes in the considered ranges.
It can be concluded that the method here developed globally preserve the proton-iron separation, but the corresponding distributions of reconstructed X^{μ}_{max} are more overlapped, making more difficult the study of the composition.

CHAPTER 7

Reconstruction of the shower-to-shower fluctuations of X^{μ}_{max}

By recalling the simplified arguments of the superposition model (see Sec. 2.1.3), it is clear that the shower-to-shower fluctuations are a mass-sensitive observable. We have seen that for an EAS initiated by a nucleus of mass A, the corresponding fluctuations are $\sigma_A = \sigma_p/\sqrt{A}$, where σ_p are the fluctuations for proton. This behaviour with the mass A is confirmed by air shower simulations, even if the trend is slightly different. The physical fluctuations are studied with the FD, whereas an analogous study by means of the SD was not possible under the conditions of the published MPD analysis (r>1700m, 55°-65°). The extension of the MPD applicability ranges studied in this work has now opened the possibility for a reliable estimation of the shower-to-shower fluctuations, exploiting the advantage of the large SD duty cycle.
In this chapter, I will show the discriminating power of $\sigma_{sh}(X^{\mu}_{max})$ (Sec. 7.1). On real data this quantity can not be measured directly, because of the detector effects which modify the width of X^{μ}_{max} distributions (Sec. 7.2). The estimation of the physical fluctuations on data requires therefore the knowledge of the detector resolution and I will illustrate the method for calculating it (Sec. 7.3). Its reliability will be demonstrated, allowing to extract the shower-to-shower fluctuations from the measured ones. The associated systematic uncertainty will be also evaluated (Sec. 7.4).

7.1 Shower-to-shower fluctuation sensitivity to primary mass

In Chapter 5, the MPD features have been extensively studied on the basis of a set of MC simulations of proton and iron-induced showers produced with the hadronic interaction models EPOS-LHC and QGSJetII-04. At generation level, the MPD distribution is built by using the MC slant depths of muons arriving at ground between 1200 m and 4000 m from the shower core. By means of the USP fit, performed event-by-event, the mass-sensitive observable $X^{\mu}_{max,MC}$ is extracted. The standard deviation of the distribution of $X^{\mu}_{max,MC}$ represents the physical fluctuations of the maximum. In particular $\sigma_{sh}(X^{\mu}_{max,MC})$ (from now on indicated as $\sigma_{sh,MC}$ for brevity) is obtained by fitting the distributions of $X^{\mu}_{max,MC}$ with a gaussian function in each energy bin, as shown in Fig. 7.1 (panel a). The evolution of $\sigma_{sh,MC}$ with the primary energy is again reported here in Fig. 7.1 (panel b), for the set of simulations used in this work and summarised in Table 6.1.
It is evident that proton and iron are well separated, by about 40 g/cm^2. In addition it is remarkable the agreement between hadronic interaction models. This makes the fluctuations of X^{μ}_{max} more robust than X^{μ}_{max} itself for mass compositions studies.

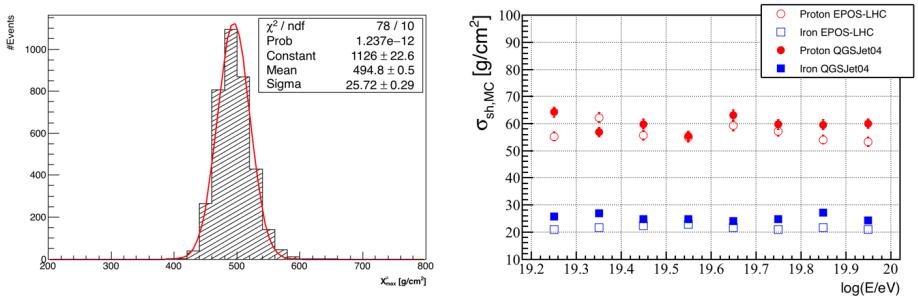

(a) (b)

Figure 7.1: (Panel a) Distribution of X^{μ}_{max} evaluated at generation level for iron QGSJetII-04 simulated showers in the whole energy and angular range of the analysis. From the gaussian fit, the shower-to-shower fluctuations are evaluated: $\simeq 25.7 \pm 0.3$ g/cm^2. (Panel b) Monte Carlo shower-to-shower fluctuations of X^{μ}_{max} as a function of the energy for both hadronic model simulations EPOS-LHC (empty symbols) and QGSJetII-04 (full symbols) and for proton (red) and iron (blue) primaries.

7.2 Observed fluctuations on MC simulations

The relation between the physical fluctuations of the MPD maximum and the observed ones is the following:

$$\sigma^2_{obs} = \sigma^2_{sh} + \sigma^2_{det} \tag{7.1}$$

σ_{obs} represents the fluctuations observed after all reconstruction steps. The term σ_{sh} indicates the physical fluctuations (shown in Fig. 7.1 for MC at generation level) and σ_{det} is the detector resolution. This means that the mass-sensitive observable can not be directly measured on real data, because the distribution of reconstructed X^{μ}_{max} is modified by the detector effects. This can be clearly seen in Fig. 7.2, where the distributions of X^{μ}_{max} are reported, as example, for iron QGSJetII-04 simulated events. The histograms are obtained for 8 bins of $\log_{10}$(E/eV), as indicated: the black hatched ones refer to $X^{\mu}_{max,MC}$, while the blue ones to the reconstructed MPD maximum $X^{\mu}_{max,Rec}$. It can be seen that the reconstruction modifies the distributions: it shifts them, changing the average value of X^{μ}_{max}, and it enlarges them. Therefore, the physical fluctuations must be deconvolved from measurements, by subtracting the detector resolution.

7.3 Evaluation of the detector resolution

The detector resolution can be evaluated on MC simulations as the standard deviation of the X^{μ}_{max} reconstruction bias distribution:

$$\sigma_{det} = \sigma(X^{\mu}_{max,Rec} - X^{\mu}_{max,MC}) \tag{7.2}$$

The detector resolution from the bias distributions is shown in Fig. 7.3 as a function of the logarithm of the primary energy, in the angular range [45°-65°], for the whole set of simulations used in this work. The resolution improves with energy because of the increasing number of muons. In addition, it ranges from about 60 g/cm^2 at $\log_{10}$(E/eV) = 19.2 to about 40 g/cm^2 at $\log_{10}$(E/eV) = 20 for proton showers. It is 10 g/cm^2 smaller

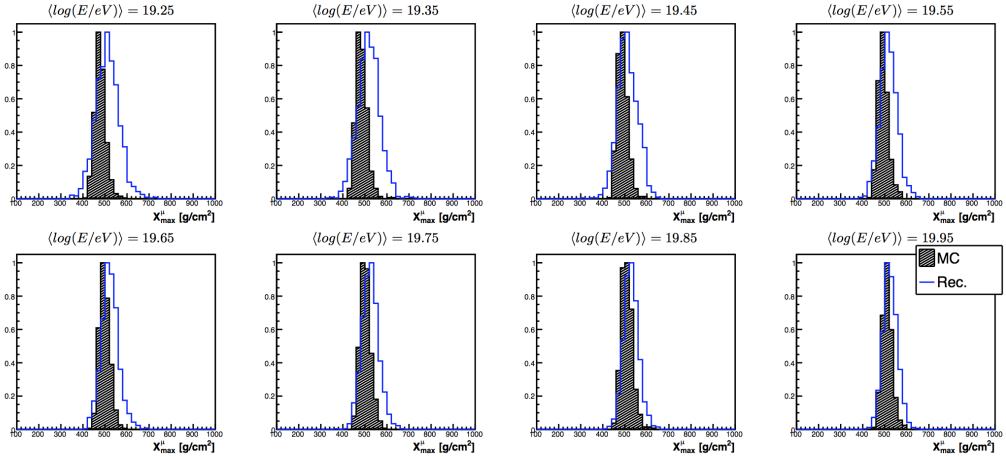

Figure 7.2: Distributions of X^{μ}_{max} for simulated iron QGSJetII-04 events in 8 bins of $\log_{10}$(E/eV). Black hatched histograms refer to $X^{\mu}_{max,MC}$, i.e. to values calculated at generation level. Blue histograms refer to $X^{\mu}_{max,Rec}$, i.e. the maximum MPD values after the reconstruction chain described in Chapter 6.

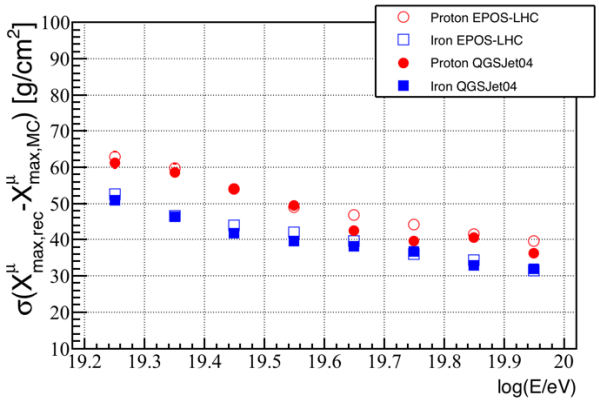

Figure 7.3: The detector resolution evaluated on the X^{μ}_{max} reconstruction bias distribution as a function of the logarithm of the primary energy for two hadronic model simulations EPOS-LHC (empty symbols) and QGSJetII-04 (full symbols) and for proton (red) and iron (blue) primaries.

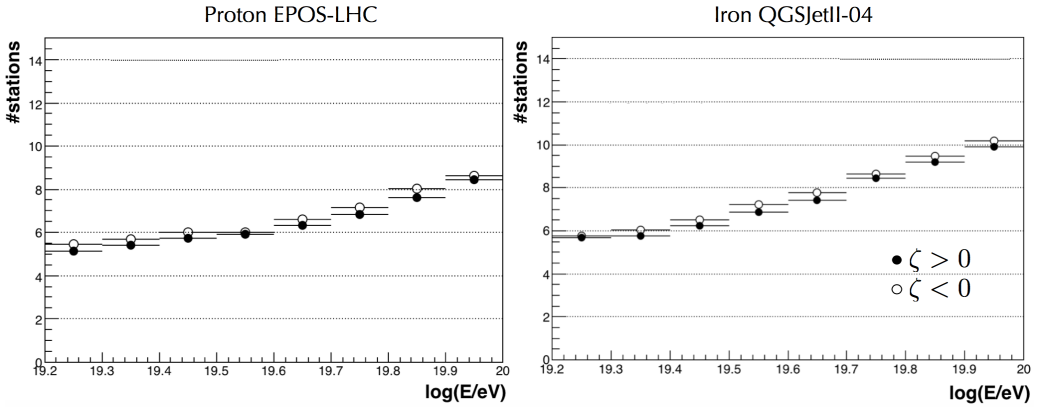

Figure 7.4: Number of stations participating to the MPD reconstruction as a function of energy, for proton/EPOS-LHC (left panel) and iron/QGSJetII-04 (right panel) in the left sector (ζ<0, empty dots) and the right sector (ζ>0, full circles).

in the case of iron showers, because they are richer in muons and because the reconstruction performs differently depending on the primary mass.
Of course, Eq. (7.2) can not be estimated on real data and for this reason an alternative method has been investigated [136].
In general, two simultaneous and independent measurements of the MPD for the same event allow to calculate the detector resolution. As already explained, the MPD reconstruction for each event is based on the timing information recorded by the SD stations. If their number is large enough, the accepted stations can be in principle subdivided in two (or more) sets. Depending on the azimuthal angle of the stations in the shower reference frame, two MPD distributions can be built: one with *left* stations (ζ<0) and one with *right* stations (ζ>0), that we well call respectively *left* MPD and *right* MPD. The two sectors are selected so that the signal distribution is symmetric for each of them.
As shown in Fig.7.4, given the energy, zenith and core distance ranges considered in this work, the average number of stations per event in each sector is high enough for a correct estimation of both X^{μ}_{max} from left MPD and X^{μ}_{max} from right MPD.
Exploiting this method (hereafter referred to as the *left-right method*), the detector resolution is obtained as:

$$\sigma_{det} = \sigma\left(\frac{X^{left}_{Rec} - X^{right}_{Rec}}{\sqrt{2}}\right) \tag{7.3}$$

where $X_{Rec} = X^{\mu}_{max,Rec}$ for brevity and X^{left}_{Rec}, X^{right}_{Rec} refer to the maximum of the left MPD and of the right MPD respectively. The denominator of Eq. (7.3) is a statistical factor. It takes into account that the resolution decreases as the square root of the number of muons and that the two MPDs will have about half of the total muons that would be used to build the total MPD of the event. The statistical factor in the case of two divisions is therefore trivially derived as follows:

$$\eta = \sqrt{\frac{N^{\mu}_{left} + N^{\mu}_{right}}{2} \cdot \frac{1}{N^{\mu}_{tot}}} \tag{7.4}$$

Fig. 7.5 (panel a) shows an example of the distribution obtained by means of Eq. (7.3) for simulated iron QGSJetII-04 showers. The average value is centered around 0, con-

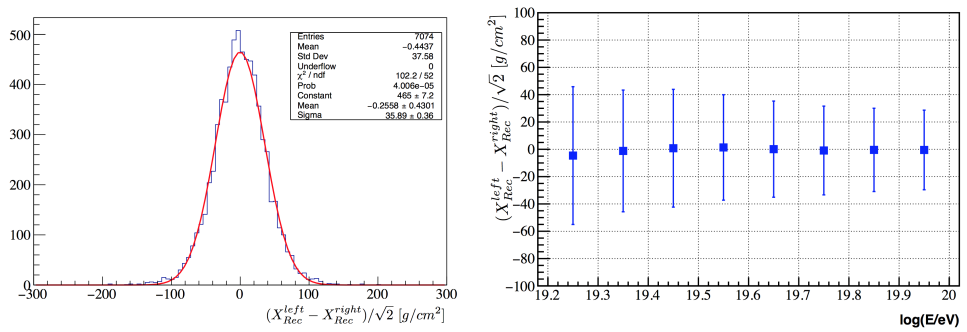

(a) (b)

Figure 7.5: Distribution derived from Eq. (7.3) for a set of simulated iron showers for the whole energy range of this analysis. The standard deviation gives the detector resolution (panel a). Results of Eq. (7.3) as a function of the energy for iron showers. The bars represent the detector resolution (panel b).

firming that the muon signal distribution is about the same on each sector. On each distribution derived from Eq. (7.3) a gaussian fit is performed and the standard deviation is extracted, which is the detector resolution we are looking for. The results as a function of the energy are shown in Fig. 7.5 (panel b). Average values are centered on 0 as expected, the bars represent the standard deviation of the distributions, i.e. the detector resolution.
The reliability of this method can be checked at MC level by comparing it with the detector resolution from Eq. (7.2). The results obtained in the two ways are shown in Fig. 7.6 for proton and iron and for the two hadronic interaction models used in this work. One can see that globally the detector resolution estimated from the left-right method reproduces the one found from the distributions of ($X^{\mu}_{max,Rec}$-$X^{\mu}_{max,MC}$). This confirms the reliability of the method here described.

7.4 Reconstruction of shower-to-shower fluctuations

In the previous section, the reliability of the left-right method for the detector resolution estimation has been demonstrated . This procedure is therefore exploited in order to derive on real data the physical fluctuations of the shower, by simply inverting Eq. (7.1):

$$\sigma_{sh} = \sqrt{\sigma^2_{obs} - \sigma^2_{det}} \tag{7.5}$$

σ_{sh} is evaluated at generation level on simulations and it is reported in Fig.7.1. We call it $\sigma_{sh,MC}$ and use it as our reference. Similarly to the bias defined in Chapter 6, we can now calculate the bias on the estimation of the shower-to-shower fluctuations:

$$\text{bias} = \sigma_{sh,Rec} - \sigma_{sh,MC} \tag{7.6}$$

$\sigma_{sh,Rec}$ refers to the physical fluctuations extracted with Eq. (7.7), which are shown in Fig. 7.7 for all primaries and hadronic interaction models as a function of the logarithm of the energy in 8 bins of Δlog(E/eV) =0.1 between 19.2 and 20.
The bias associated to the reconstruction of the shower-to-shower fluctuations of X^{μ}_{max}

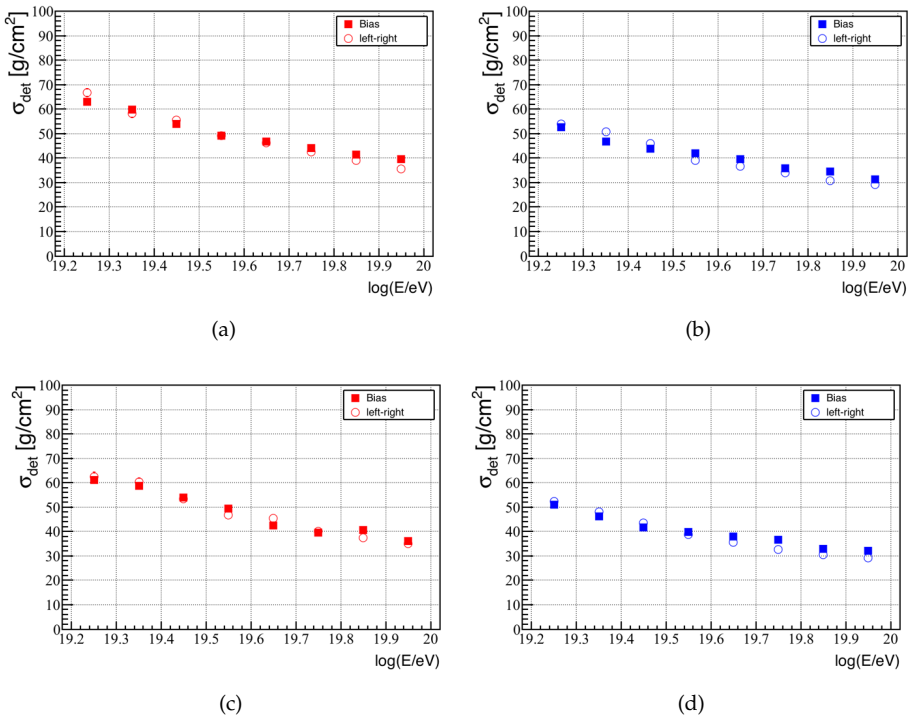

Figure 7.6: Detector resolution obtained from the bias distributions and from the left-right method for proton EPOS-LHC (panel a), iron EPOS-LHC (panel b), proton QGSJetII-04 (panel c), iron showers QGSJetII-04 (panel d).

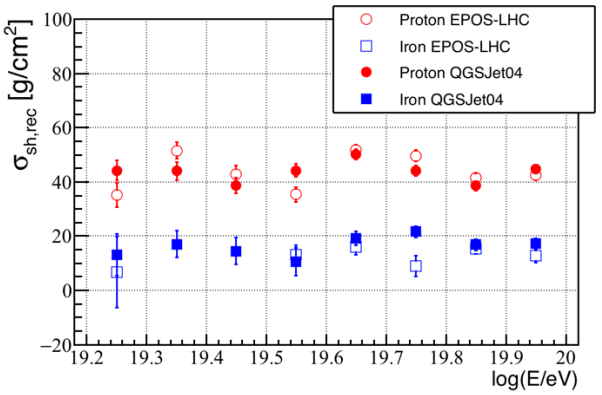

Figure 7.7: Reconstructed shower-to-shower fluctuation as a function of the logarithm of the energy for the two hadronic model simulations EPOS-LHC (empty symbols) and QGSJetII-04 (full symbols) and for proton (red) and iron (blue) primaries. The bars represent the statistical errors.

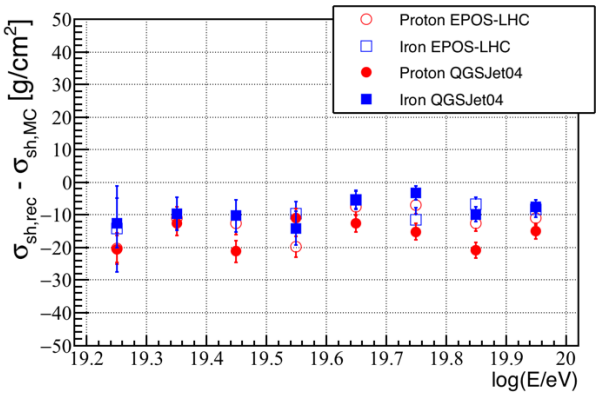

Figure 7.8: Bias on the shower-to-shower fluctuation reconstruction (Eq. 7.6) as a function of the logarithm of the energy for the two hadronic interaction models EPOS-LHC (empty symbols) and QGSJetII-04 (full symbols) and for proton (red) and iron (blue) primaries. The bars represent the statistical errors.

is shown in Fig. 7.8. It can be seen that the shower-to-shower fluctuations are on average systematically underestimated of -12 g/cm^2, independently on the energy. This will be taken into account in the data analysis in order to have an unbiased estimation of σ_{sh}. Furthermore, the bias depends on the primary and hadronic interaction model. As done for the X^{μ}_{max} analysis, the mass and model spread can be defined as the difference between the maximum and the minimum bias value divided by 2. It turns out to be $\pm$10 g/cm^2. This is the systematic uncertainty that is associated to the method here described.

CHAPTER 8

Measurement of X^{μ}_{max} and $\sigma_{sh}(X^{\mu}_{max})$ on data

In this last chapter of my thesis I will finally discuss the results of X^{μ}_{max} and $\sigma_{sh}(X^{\mu}_{max})$ I obtained applying the method described in chapter 6 and chapter 7 on Auger data. The dataset I used is between January 2004 and September 2016. A preliminary study about the correlation with the electromagnetic X_{max} will be presented. The muonic elongation rate, the angular dependence of X^{μ}_{max} and the energy dependence of $\sigma_{sh}(X^{\mu}_{max})$ will be shown. On a shower-to-shower basis, hadronic interaction and primary composition studies are difficult because of the intrinsic shower-to-shower fluctuations which characterise shower properties. For this reason the results will be shown by estimating the average $\langle X^{\mu}_{max} \rangle$ and its fluctuations, starting from the X^{μ}_{max} distributions measured in different energy or angular bins. The systematic uncertainties will be also discussed. In addition, exploiting the X^{μ}_{max} measurements the logarithm of the mass A will be derived.

8.1 Summary of the MPD reconstruction and data selection

The data analysis is performed exploiting the $\overline{\text{Off}}\underline{\text{line}}$ framework, v3r0 version, with the standard event reconstruction, as well as the updated atmospheric databases. The latter are of crucial importance to correctly convert the measured muon production height [m] to the muon production depth [g/cm^2].
Physical events are selected by requiring the 6T5 trigger. As explained in Sec. 3.3, this is a stringent quality trigger which ensures to have a sample with a good reconstruction of all parameters at ground. In addition, events are accepted for the analysis after excluding bad periods (i.e. periods with known software or hardware malfunctioning) and by eliminating the lightnings. Finally, for each event, SD stations with accidental timing information are excluded.
As discussed in detail in the previous chapters, a good reconstruction of the muon longitudinal profiles is obtained by limiting the energy, zenith angle of the air showers and station distance from the core. The same ranges applied on simulations have been applied on data and the specific cuts used in this work can be summarised again as follows:

- E $\geq 10^{19.2}$ eV ($\simeq$ 15 EeV) , to ensure a minimum number of muons per event ($\simeq$ 15);
- $45^{\circ} \leq \theta \leq 65^{\circ}$, to ensure a full profile development;
- shower core distance between 1200 and 4000 m, to ensure a low dependence of the reconstructed muon times on the parametrised kinematical delay.

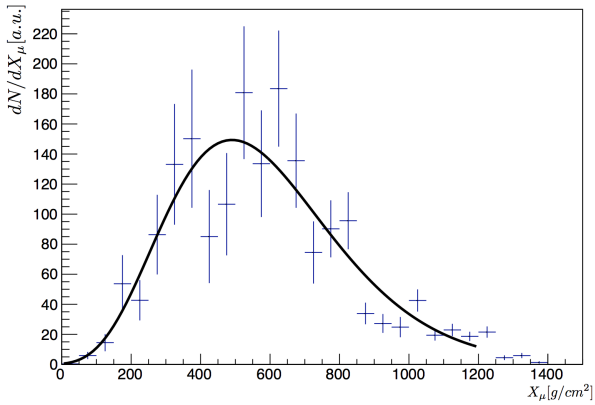

Figure 8.1: Example of reconstructed MPD distribution for a real event with zenith angle 50° and energy 50 EeV. The USP fit is shown (black line).

The MPD reconstruction on real data is implemented with the different steps described in chapter 6. They are here summarised for sake of clarity.

- Step 1: for each event passing the above mentioned selection criteria, SD stations between 1200 m and 4000 m are accepted for the reconstruction if the total signal for each of them is greater than 3 VEM. This allows to further minimise the impact of accidental signals. In order to extract the muonic signal from the total recorded trace, the smoothing algorithm and the time cut are applied on the signal of each SD station.

- Step 2: for each muon, its delay t is calculated. Firstly, an approximated production height z is estimated, assuming that the delay is only geometrical. The approximated z is then used in order to evaluate the kinematical delay of the studied parametrisation. The latter together with the time offset of 60 ns are exploited for the final estimation of the muon time delays. These are corrected for the decay length of pions and the production height z is evaluated and converted to the slant depth X, according to the atmospheric density profile. The values of X^μ are stored in a histogram and the MPD profile is obtained in each station. The MPD distribution of a given event is finally built by adding the distributions from each SD station.

- Step 3: the USP fit is applied on the MPD of each event in the range 0-1200 g/cm^2, setting the starting value of L and fixing R as a function of the zenith angle of the event, according to simulations. Once the fit has been performed, a set of quality cuts is applied in order to discard events for which the X^μ_{max} estimate is not reliable, as explained in Sec. 6.3.7.

- Step 4: for each event passing all the described cuts, X^μ_{max} is corrected for the reconstruction bias of the method, according to Table 6.3.

The quality cuts applied after the fit procedure remove about 1% of the total sample and the total final statistics of data used for this analysis amounts to 2268 events. An example of measured MPD for one of the selected real events is shown in Fig. 8.1, together with the USP fit.

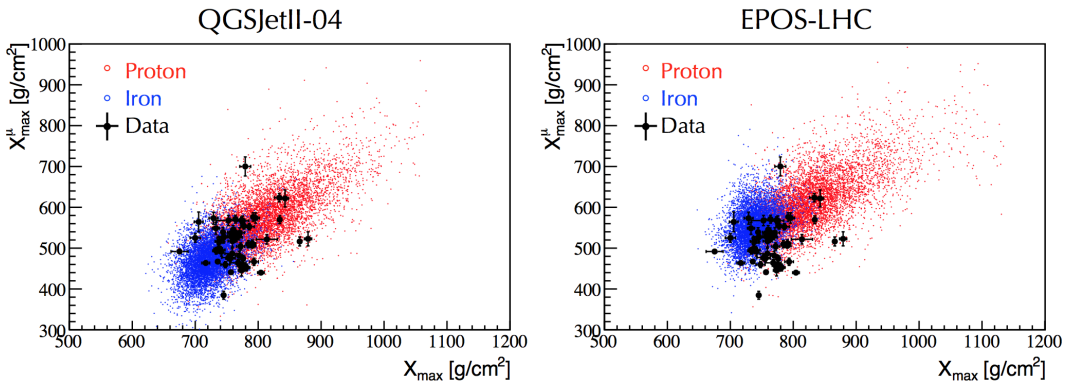

Figure 8.2: The measured X^{μ}_{max} vs. X_{max} (black dots) for the 60 events passing the selection cuts on both observables as compared to the predictions of QGSJetII- 04 (left panel) and EPOS-LHC (right panel) for both proton (red) and iron (blue) showers.

8.2 Preliminary study of the correlation between X^{μ}_{max} and X_{max}

As outlined in Sec. 5.4, the electromagnetic shower maximum X_{max} and the muonic one X^{μ}_{max} are expected to be correlated. A preliminary study has been performed in this work, in order to test the reconstruction method here described. In particular, the dataset collected up to December 2014 has been used on the basis of the analysis performed in [105] and the events recorded by both the SD and the FD have been selected. Among all hybrid events collected at the Pierre Auger Observatory, 60 events with well reconstructed X_{max} and $X^{\mu}_{\rm max}$ have been found with energies in the range [$10^{19.2}$-$10^{19.75}$eV]. This number is small because of the different quality cuts of the two analyses and also because this work is focused on energies E$\geq 10^{19.2}$ eV ($\simeq$15 EeV), but FD low duty cycle does not allow to collect a large statistics of data at the highest energies.
The results for these 60 events is shown in Fig. 8.2 (black points), together with MC proton and iron predictions, for QGSJetII- 04 (left panel) and EPOS-LHC (right panel). Data are not corrected for the bias of this MPD method (step 4) and the prediction of X^{μ}_{max} are therefore obtained at detector level (i.e. after the reconstruction procedure). For what concerns X_{max} expectations, they have been evaluated at generation level and then smeared for the detector resolution. By inspecting Fig. 8.2, it can be seen that the bulk of the measurements is superimposed to iron predictions for both models, although with very different average values. In particular, the correlation coefficient has been evaluated on data and on MC. It amounts to 0.23$\pm$0.13 on data and it is compatible with that predicted from iron showers, which is about 0.26 (0.28) for QGSJetII-04 (EPOS-LHC) model.
In addition to being an important check which confirms the reliability of the X^{μ}_{max} measurements, this preliminary study shows that a more in-depth analysis is a promising tool for mass composition studies. In fact X^{μ}_{max} and X_{max} rely on very different measurements, have very different systematics and give insight on complementary components of the shower. By exploiting for example a multi-variate technique, the simultaneous analysis of these two observables can therefore provide very interesting results, enhancing the discriminating power of the single variables.

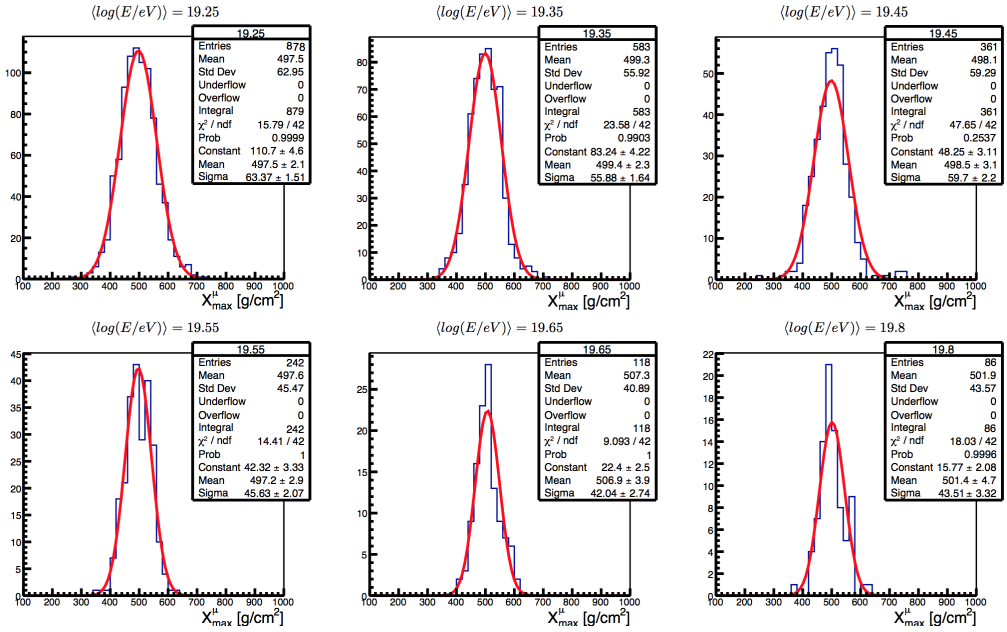

Figure 8.3: Distributions of X^{μ}_{max} measurements in the zenith range [45°-65°] shown in 6 energy bins of $\log_{10}$(E/eV) in the range [19.2-20]. See text for more details.

8.3 X^{μ}_{max} analysis

Fig. 8.3 shows the unbiased distribution of X^{μ}_{max}, obtained by applying on data all the steps summarised in Sec. 8.1, for 6 different energy bins. For energies $\log_{10}$(E/eV) between 19.2 and 19.7, the bins have a width of $\Delta\log_{10}$(E/eV)=0.1. For greater energies, there is not enough statistics to keep the same binning and data are integrated in one bin for $\log_{10}$(E/eV) in the range [19.7-20]. A gaussian fit is performed on each histogram and the first two moments of the distributions are extracted: the average MPD maximum and the standard deviation. From the latter, the shower-to-shower fluctuations will be derived in Sec. 7.

All results are referred to an average zenith angle of 55°, by correcting for the angular dependence of X^{μ}_{max}. This has been studied on MC, in particular on the whole MC sample in order to take into account the mass/model dependence. Fig. 8.4 shows the results of this study, in particular the evolution of the simulated X^{μ}_{max} with the zenith angle. According to simulations, a simple linear function in $cos\theta$ can describe the zenith dependence. The red line represents the linear fit, whose slope β is exploited to refer $X^{\mu}_{max}(\theta)$ to the equivalent value at 55°:

$$X^{\mu}_{max}(55^{\circ}) \simeq X^{\mu}_{max}(\theta) - \beta \cdot (\cos\theta - \cos 55^{\circ}) \tag{8.1}$$

The systematic uncertainty related to this choice has been evaluated on the data by using the correction estimated on a single primary and hadronic model. It can be considered negligible given that the measured X^{μ}_{max} changes by less than 1 g/cm^2.

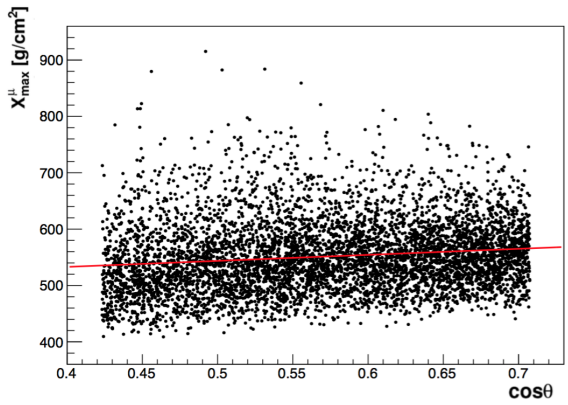

Figure 8.4: Scatter plot of $X^{\mu}_{max,MC}$ and $cos\theta$ evaluated on the mixed sample of proton and iron showers simulated with EPOS-LHC and QGSJetII-04. The red line is the linear fit whose slope is used for referring X^{μ}_{max} measured on data to 55°.

8.3.1 Systematic uncertainties

Possible sources of systematic uncertainty have been investigated. In the following a brief list is reported for the different contributions which have been examined.

Mass and Model Spread. As discussed in Section 6.3.8, the difference between the reconstructed and the simulated X^{μ}_{max} depends on the mass and on the hadronic interaction model exploited in the simulations. In other words, the reconstruction bias shows a spread between masses and hadronic models and it amounts to about ± 14 g/cm^2. This is considered as the systematic error due to the reconstruction effects, differences in the hadronic interaction models and differences due to the unknown nature of the primary particle. It is the most important contribution to the total uncertainty.

Long-term stability. A possible dependence of the X^{μ}_{max} measurement on seasonal variation has been checked. Fig. 8.5 shows X^{μ}_{max} as a function of the time, where single data points refer to seasons, starting from 2008 up to 2015. This set of years has been chosen in order to have a comparable statistics of events for each data point. Indeed, the SD array was completed in 2008.
The results shown in Fig. 8.5 seem to indicate some small variation in time which goes beyond simple statistical fluctuations. By fitting the measurement with a constant function, one finds $\chi^2/\text{ndf} \simeq 1.3$. However, the observed variation can not be interpreted as a seasonal effect, since its period is not compatible with the year time-scale (the fit with a sinusoidal function gives a period of about 1.5). In order to take into account this effect of unknown origin, an error of σ_{sys} = 3.5 g/cm^2 is included in the systematics. It has been determined as follows:

$$\sigma_{sys} = \sqrt{\bar{\sigma}^2 - \sigma^2_{stat}} \tag{8.2}$$

where $\bar{\sigma}=\frac{1}{\sqrt{1/\sum \sigma_i^2}}$ is the the standard deviation of the sample and σ_{stat} is the average error evaluated on the total sample between 2008 and 2015.

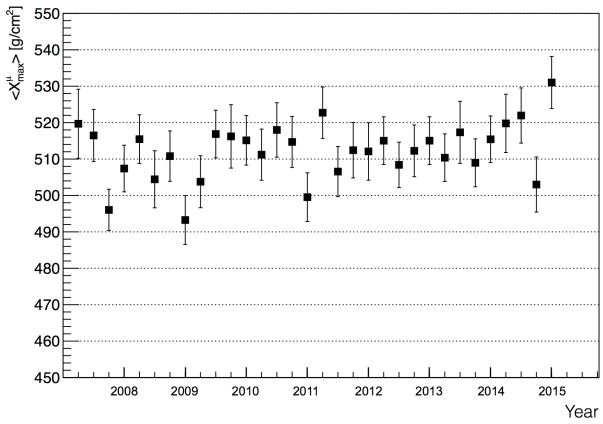

Figure 8.5: X^{μ}_{max} as a function of the time. Each data point represents the average value of the measurement over a season. The years between 2004 and 2007, together with 2016, have been excluded from the evaluation of the long-term stability of X^{μ}_{max}, because they are poorer in statistics: the array was completed in 2008 and the dataset used in this work is up to September 2016.

Selection Efficiency. The quality of the MPD profile reconstruction improves with the number of sampled muons. For this reason, the analysis shows a better performance in the case of iron showers, which are richer in muons. This translates in a different selection efficiency of the method (i.e. the number of events which passes the selection cuts), that may introduce a systematic effect in the determination of X^{μ}_{max}. The difference in the selection efficiency between proton and iron showers is on average smaller than 5% for both hadronic models. The possible associated systematic uncertainty has been determined by analysing a MC mixed sample (50% proton, 50% iron) after the quality cuts used in this work. This results in a small contribution of 1 g/cm^2 to the systematics.

Core Position. The azimuthal asymmetry in extensive air showers produces a systematic shift of the core position to the early part of the shower. In fact, the early part has a higher signal density, when cylindrical symmetry is assumed, as in the Offline reconstruction process. We evaluated this shift on available simulations, finding an average bias of 90 m in agreement with [137]. It depends on the zenith range, mass and model. In particular, the bias is greater for proton showers. The corresponding systematic error has been estimated at MC level, by building the MPD starting from the true core position instead of the reconstructed one. The associated systematic uncertainty on X^{μ}_{max} is small and amounts to about 2 g/cm^2.

Angular and Energy Resolution. The measurement of X^{μ}_{max} is corrected for a reconstruction bias that depends on the energy and zenith angle (Sec. 6.3.8). Besides, the L and R parameters are set as a function of the zenith angle, event by event (Sec. 6.3.7); the time cut for the removal of the high energy electromagnetic background is a function of both the zenith angle and the energy. For these reasons, it is important to quantify the effect due to the angular and energy resolution on X^{μ}_{max}. In the energy and zenith angle range of interest, the angular resolution of the Pierre Auger Observatory is 0.7°, given the cut on the minimum number of stations participating to the event reconstruction, while the energy resolution is 14%. In order to investigate the possible contribution to the systematic uncertainty, the

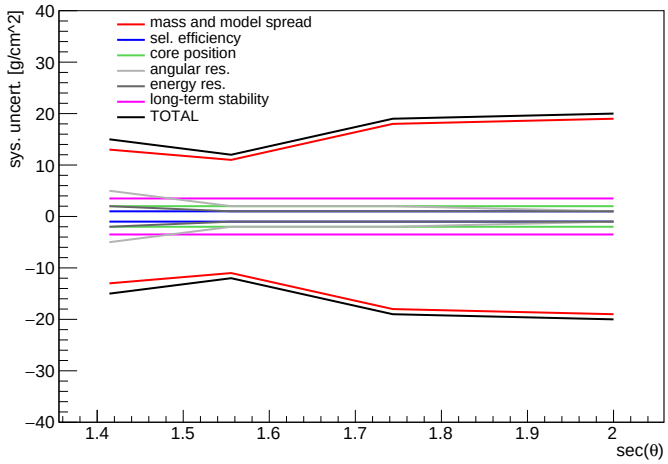

Figure 8.6: Single contributions to the systematic uncertainty on X^{μ}_{max} as a function of the zenith angle.

reconstruction has been performed by selecting randomly the zenith angle and the energy of each event from a gaussian distribution centered on the MC value and with standard deviation defined by the resolution. This has been studied separately for the zenith and for the energy. The variation in X^{μ}_{max} has been estimated in 2 g/cm^2 due to the angular resolution and of 1 g/cm^2 due to the energy resolution.

Time Variance Model. The uncertainty on the arrival time of the EAS front influences the reconstruction of the curvature and of the impact point on ground. Therefore, it can be important for the reconstruction of the MPD maximum. To evaluate its contribution to the systematics of the method, two different parametrisation of the time variance model [86] have been tested, namely the default one and that described in [138]. They differ in the modelling of the fluctuations of the arrival time of the first particle. The difference between the two models induces a systematic uncertainty smaller than 1 g/cm^2 on the determination of the maximum and it is therefore considered negligible.

Accidental muons. In general, isolated atmospheric muons or bunch of particles from low-energy showers close to a SD station can introduce a source of random noise. This can damage the data quality, in particular underestimating the start time of traces due to random signals prior to the shower ones. This effect must be therefore quantified. In order to do that, proton and iron showers have been simulated again, injecting accidental signals in the SD stations. The impact on the MPD reconstruction was found to be low, of about 1 g/cm^2, given the quality cuts which already act reducing the effect from this background.

Sources of systematic uncertainty of less than 1 g/cm^2 are neglected and only the significative contributions affecting the X^{μ}_{max} measurement are shown in Table 8.1. These add up to a total of 15 g/cm^2 in the whole considered angular range. This value is approximately 20% of the proton-iron separation and it is similar to that of the published

Source	Sys. Uncertainty [g/cm^2]
Mass and model spread	14
Long-term stability	3.5
Selection efficiency	1
Core position	2
Angular resolution	2
Energy resolution	1
Total	15

Table 8.1: The different contributions to the systematic uncertainty in the reconstruction of X^{μ}_{max}.

MPD analysis.
All the sources of systematic error have been studied as a function of the zenith angle θ and of the energy. There is no dependence on the latter, while the angular dependence is reported in Fig. 8.6. It can be seen that the contributions which vary with θ are essentially the mass/model spread and the uncertainty due to the angular resolution.

8.3.2 Muonic elongation rate

Similarly to what is done with X_{max}, the elongation rate of X^{μ}_{max} can be evaluated and compared to MC predictions. The evolution of X^{μ}_{max} with the energy is shown in Fig. 8.7, for the dataset between January 2004 and September 2016 and for events between 45° and 65°. X^{μ}_{max} is referred to 55°. The data are integrated in 6 bins of energy, for $\log_{10}$(E/eV) in the range [19.2-20]. The energy scale is converted in unit of eV. The measured X^{μ}_{max} has been corrected event-by-event for the reconstruction bias discussed in Sec. 6.3.8, taking into account its dependence on the energy and on the zenith angle. The results are shown with their statistical and systematic uncertainties and compared to proton and iron showers simulated with EPOS-LHC and QGSJetII-04 hadronic interaction models.
From the inspection of Fig. 8.7, two aspects can be underlined:

- the evolution of the measured X^{μ}_{max} with the primary energy is quite flat within the quoted uncertainties: in fact, the data are well described by an elongation rate of 9.5$\pm$7.1(stat)$\pm$3.5(sys) g/cm^2/decade. If the air shower simulations with the considered hadronic interaction models are to be taken as good representations of the underlying physics, then our data can not be described by a constant composition. In fact, in the case of pure composition, the elongation rate is expected to be $\simeq$ 50 g/cm^2/decade by both models, although with a large difference in the absolute value of X^{μ}_{max}.

- The results strongly depend on the considered hadronic interaction model and disfavour EPOS-LHC: in fact, if QGSJetII-04 is taken as reference, the data are bracketed between proton and iron predictions. If instead EPOS-LHC is chosen, it is difficult to interprete the results since in the whole energy range the data fall below the average value for iron.

Both these aspects confirm the conclusions of the published MPD analysis [121].

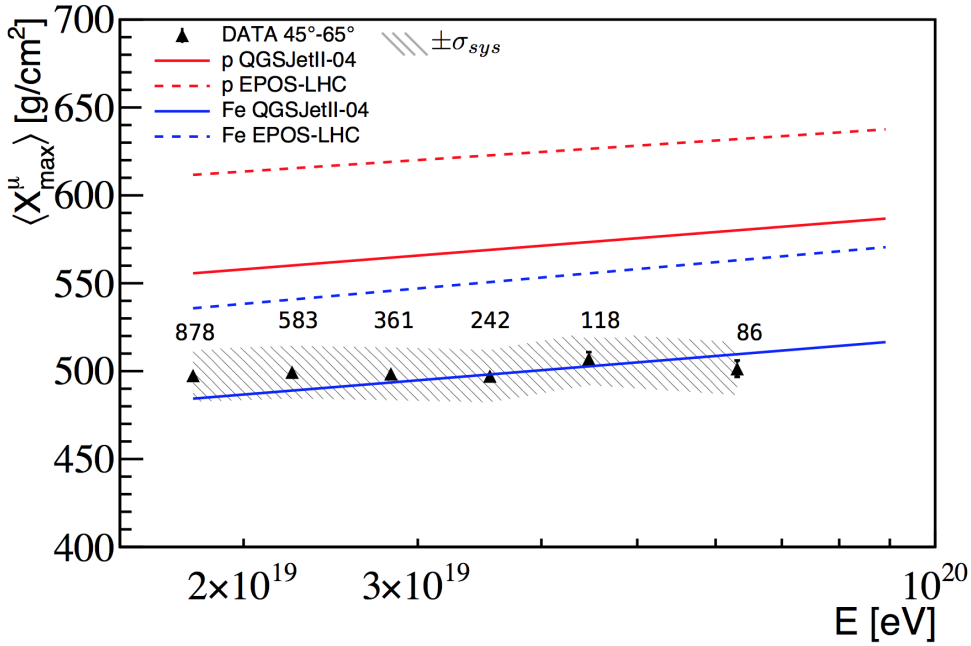

Figure 8.7: Muonic elongation rate. The measured $\langle X^{\mu}_{max} \rangle$ is referred to 55° and compared to expectations. Statistical and systematic uncertainties are shown by vertical black bars and cross-hatched ones respectively. The number of events is indicated for each energy bin.

8.3.3 Angular dependence of X^{μ}_{max}

By taking advantage of the extended angular range analysed in this work and of the large dataset, possible systematic effects of this analysis associated to the zenith angle have been studied. For this reason, X^{μ}_{max} has been evaluated as a function of the energy, separately for 4 bins of zenith of width $\Delta\theta$=5° between 45° and 65°. This is shown in Fig. 8.8. On each plot, the MC predictions for the corresponding zenith range are also reported.

It is clear that the results for the most inclined events are significantly different from those obtained at lower zenith angles. The difference is in the comparison between data and MC: while for θ<60° data are bracketed by QGSJetII-04 predictions and are inconsistent with EPOS-LHC, for θ>60° the data seem to be at odd with both EPOS-LHC and QGSJetII-04 model. This can be seen also in Fig. 8.9, where X^{μ}_{max} integrated over energy has been evaluated as a function of the zenith in 8 bins with $\Delta\theta$=2.5° between 45° and 65°. The results are reported in terms of the secant of the zenith angle. Again one can see that MC and data have a different angular dependence. Both decrease with the zenith angle, as expected, but for θ>60° (secθ=2), data show a more pronounced reduction of X^{μ}_{max}.

Since no changes in composition are expected as a function of the zenith angle, the explanation of this discrepancy could be related to some systematic effect. A possible source of systematics could be the reconstruction of inclined showers: in fact, it is well known that for this type of events the electromagnetic component of the shower is largely absorbed in the atmosphere and, therefore, the standard reconstruction may give unreliable results. For this purpose, the Pierre Auger Collaboration has developed a dedicated

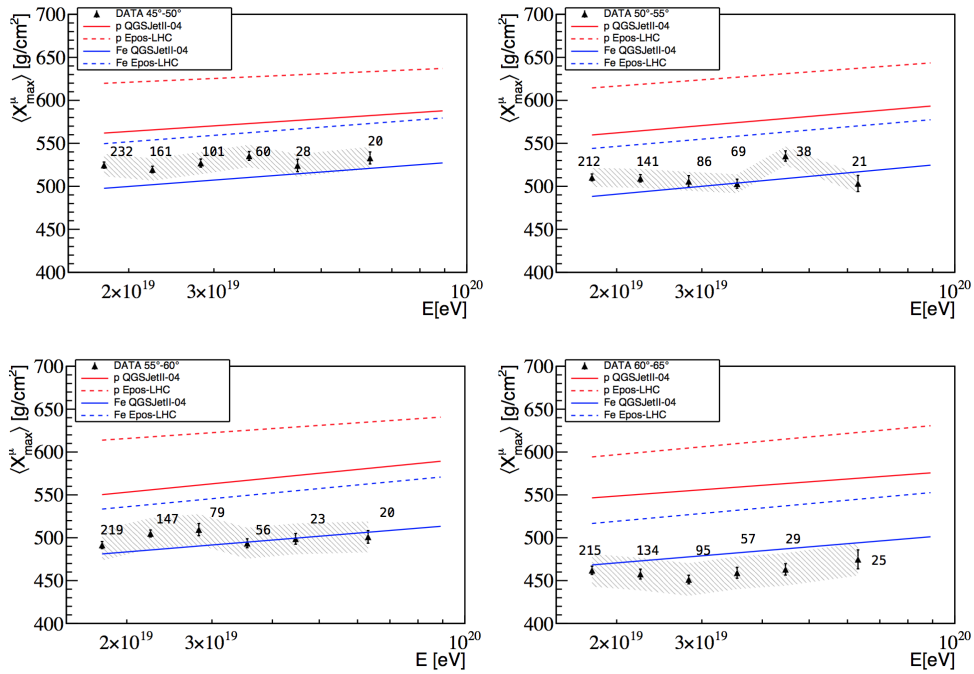

Figure 8.8: $\langle X^{\mu}_{max} \rangle$ as a function of the energy, shown in 4 zenith bins between 45° and 65°. See text for more details.

algorithm which allows a reliable reconstruction of showers above 60° (in particular, an Offline module called *SdHorizontalReconstruction*). The analysis has been therefore performed using this different event reconstruction, but no significative changes has been found on the MPD.
In conclusion, the different behaviour of data and MC at large angles is unexplained. However, it is worthwhile to point out that the known discrepancy between data and MC for some muon-related observables is larger at high zenith angles. As discussed in Sec. 4.2.2, the analysis of horizontal showers (θ>60°), which are muon dominated at ground, brought to the conclusion that both QGSJetII-04 and EPOS-LHC predict from 30% to 80% less muons than observed [120]. According to a more recent analysis discussed in Sec. 3.8.5 and performed on hybrid events with θ<60°, the average hadronic shower is instead from 33% to 60% larger than predicted, with a corresponding deficit of muons in simulations [47].
Therefore the increasing difference found in this analysis between data and expectations with growing inclination of the event may indicate a problem at simulation level.

8.4 $\sigma_{sh}(X^{\mu}_{max})$ analysis

In chapter 7, the procedure for evaluating the shower-to-shower fluctuations has been studied. For sake of clarity, it is briefly summarised here as follows:

- The left-right method is used for evaluating the detector resolution (Sec. 7.3): for each event, two MPDs are reconstructed, one with stations with azimuth angle ζ>0

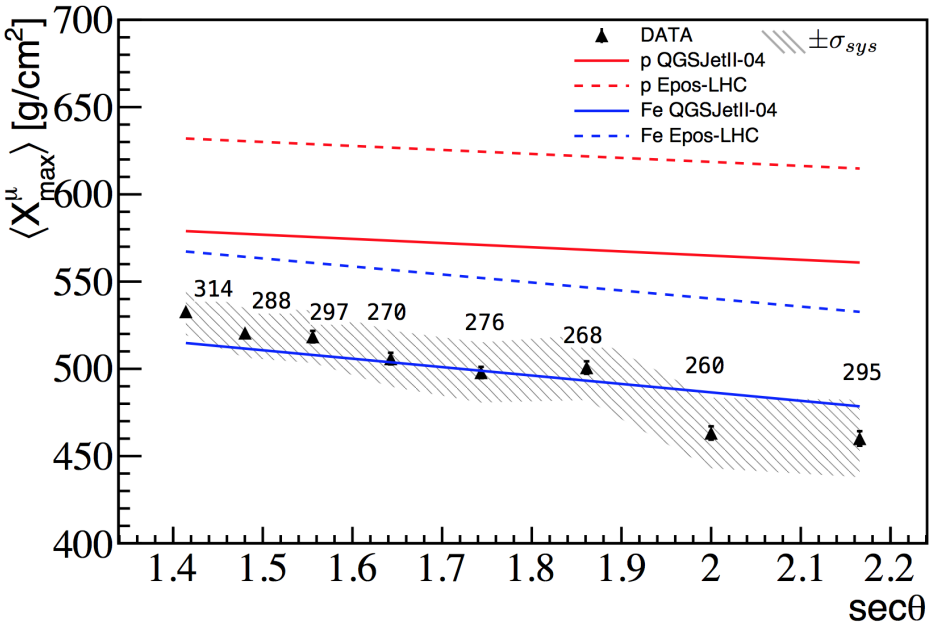

Figure 8.9: Average $\langle X^{\mu}_{max} \rangle$ as a function of the secant of the zenith angle. Statistical and systematic uncertainties are shown by vertical black bars and cross-hatched ones respectively. The number of events is indicated for each angular bin.

and one with ζ<0. By exploiting this simultaneous measurement of the same event, the detector resolution is calculated.

- The physical fluctuations of X^{μ}_{max} are extracted from the observed ones, i.e. from the standard deviations of distributions in Fig. 8.3. The formula used for deriving the shower-to-shower fluctuations is the following:

$$\sigma_{sh}(X^{\mu}_{max}) = \sqrt{\sigma^2_{obs}(X^{\mu}_{max}) - \sigma^2_{det}(X^{\mu}_{max})} \tag{8.3}$$

The calculation of the detector resolution can be applied on MC simulation (as already done in Sec. 7.3) and real data. Fig. 8.10 compares the detector resolution from simulations to that obtained with the same method on data. It can be seen that results are compatible within the statistical uncertainties, confirming the reliability of the method for extracting the physical fluctuations of X^{μ}_{max} from the measurements.
In the following, the contributions to the systematic uncertainty will be shown and the results will be presented and discussed. In particular, the latter will be derived by subtracting in quadrature the detector resolution as obtained by a fit on the data (black points in Fig. 8.10) to the total measured standard deviation of X^{μ}_{max}.

8.4.1 Systematic uncertainties

The different contributions to the systematic uncertainty on $\sigma_{sh}(X^{\mu}_{max})$ have been studied and can summarised as follows.

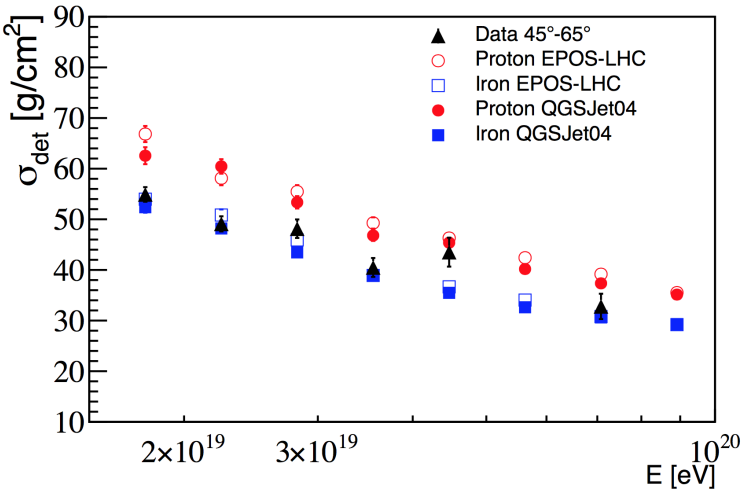

Figure 8.10: Detector resolution on data and on MC simulations for QGSJetII-04 and EPOS-LHC proton and iron showers.

Mass and model spread. As for X^{μ}_{max}, the reconstruction bias on $\sigma_{sh}(X^{\mu}_{max})$ depends on the primary and hadronic interaction model and the mass and model spread is defined as the difference between the maximum and the minimum bias value divided by 2. It turns out to be ± 10 g/cm^2, as shown in Fig. 7.8 of Chapter 7. This contribution is reported in Table 8.2 and it is the main source of systematic uncertainty.

Long-term stability. σ_{obs} and σ_{det} have been studied as a function of the time. By following the same approach used for X^{μ}_{max}, it has been found a contribution to the systematic uncertainty which amounts to 2.5 g/cm^2.

Other contributions. The sources of systematic errors on X^{μ}_{max} can in principle affect also σ_{obs} and σ_{det}. It has been therefore studied their impact on the measurement of the shower-to-shower fluctuations. All the significative contributions are shown in Table 8.2.

The systematics have been evaluated on MC simulations, except for the long-term stability. The estimation has been performed in a conservative way by calculating the change in $\sigma_{sh}(X^{\mu}_{max})$ due to the change in σ_{obs} and σ_{det}. The overall systematic error on $\sigma_{sh}(X^{\mu}_{max})$ amounts to 11 g/cm^2 for the whole angular range [45°-65°]. This value is approximately 30% of the proton-iron separation.

8.4.2 Energy dependence of the shower-to-shower fluctuations

The energy dependence of the shower-to-shower fluctuations of $\langle X^{\mu}_{max} \rangle$ is an important ingredient bringing information on the primary composition and allowing to test the hadronic interaction models.
In Fig. 8.11 the results about the evolution of $\sigma_{sh}(X^{\mu}_{max})$ with the primary energy are shown. The data are corrected for the bias of -12 g/cm^2 found on simulations in the comparison between the reconstructed value and the MC one. All data between 45° and

Source	Sys. Uncertainty [g/cm^2]
Mass and model spread	10
Long-term stability	2.5
Selection efficiency	1
Core position	1
Angular resolution	4
Energy resolution	1
Total	11

Table 8.2: The different contributions to the systematic uncertainty in the reconstruction of the shower-to-shower fluctuations $\sigma_{sh}(X^{\mu}_{max})$.

65° are considered and the number of events in each energy bin is shown.
In this case, predictions from the two hadronic interaction models are not at odds between each other and a univocal interpretation in terms of mass composition can be given. In particular, the values obtained for $\sigma_{sh}(X^{\mu}_{max})$ give an hint of a mixed-heavy composition at all energies.
Finally, it is worth mentioning that compatible results are obtained if the average detector resolution from MC simulations is used instead of that obtained from data.

8.5 Information about UHECR mass and comparison with other observables

It is possible to infer the mass composition of UHECRs from the measurements of X^{μ}_{max}. In particular, a linear relation is expected between X^{μ}_{max} and the logarithm of the primary mass A, as it happens for the X_{max}. In fact, assuming that the superposition model holds also for the muonic component of a shower and following the same arguments given in Sec. 4.1, $\ln A$ from X^{μ}_{max} can be derived:

$$\langle \ln A \rangle = \ln 56 \frac{\langle X^{\mu}_{max,p} \rangle - \langle X^{\mu}_{max,data} \rangle}{\langle X^{\mu}_{max,p} \rangle - \langle X^{\mu}_{max,Fe} \rangle} \tag{8.4}$$

$\langle X^{\mu}_{max,p} \rangle$, $\langle X^{\mu}_{max,Fe} \rangle$ and $\langle X^{\mu}_{max,data} \rangle$ refer respectively to proton simulated showers, iron simulated showers and data. This relation was tested at generation level and it was demonstrated that the deviation from the linearity between X^{μ}_{max} and lnA is small, about 6 g/cm^2 [139]. This therefore allows to exploit Eq. (8.4) for the evaluation of $\langle \ln A \rangle$. The average $\langle \ln A \rangle$ for a given energy bin can be calculated separately for the two hadronic interaction models, starting from the corresponding average values found in simulations and in data. Since $\langle \ln A \rangle$ is evaluated for each hadronic interaction model, X^{μ}_{max} data are corrected for the reconstruction bias of each model separately. For the same reason, the systematic uncertainty is about 7 g/cm^2 (instead of 15 g/cm^2), because only the difference due to the mass spread has to be taken into account. It is worth to highlight that the systematics can be reduced by using the measured X^{μ}_{max} (instead of the unbiased value) and comparing it with the MC predictions obtained at detector level. In this case, the systematic error due to the mass and model spread of the reconstruction method would cancel and the systematics which enter the evaluation of $\langle \ln A \rangle$ would reduce from 7 to 4 g/cm^2, but at the cost of using a measurement of the mass folded with detector effects.
The result of (unbiased) $\langle \ln A \rangle$ is shown for the two different hadronic models in Fig.

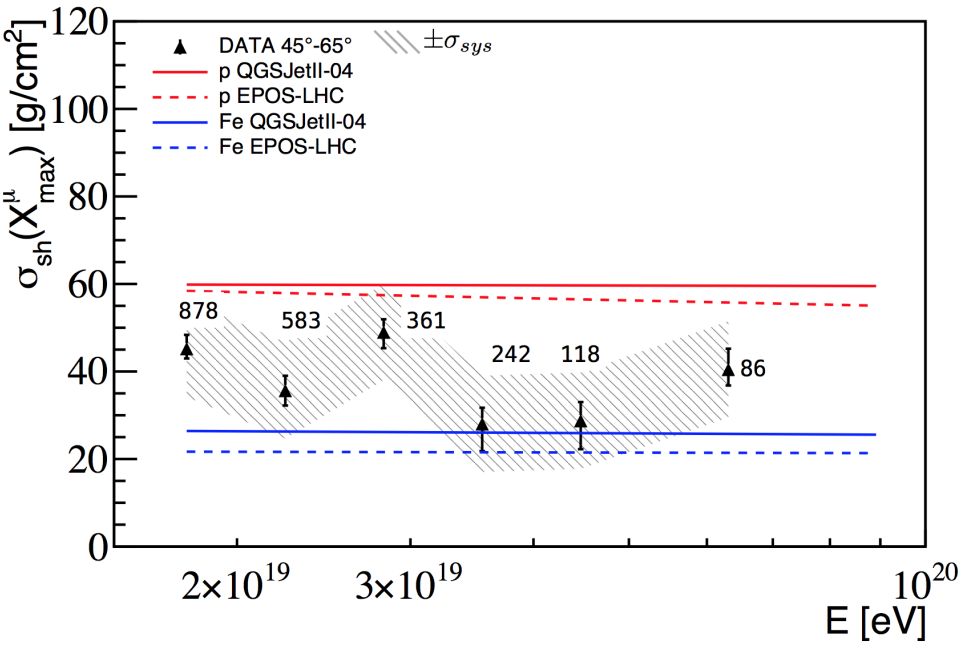

Figure 8.11: Shower-to-shower fluctuations $\sigma_{sh}(X^{\mu}_{max})$ from data compared to predictions for different primaries and hadronic models. Statistical and systematic uncertainties are shown with black and grey bars respectively.

8.12. $\ln A$=0 corresponds to proton nuclei, $\ln A$=4 to iron nuclei. The systematics (gray bars) and the statistical uncertainties (black lines) are indicated. It is clear that the $\ln A$ results depend on the simulations. This study is therefore subject to some level of uncertainty. In fact, by estimating the muonic elongation rate, a large discrepancy between experimental data and the predictions of EPOS-LHC has been highlighted. This is reflected in terms of mass composition: when this model is used to interpret the data, the composition seems to be dominated by elements heavier than iron ($\ln A$ is larger than 5). If QGSJetII-04 is considered, the composition is instead iron-like, showing a trend with energy toward heavier composition. Both, these results are coherent with the observed muonic elongation rate.
The evaluation of $\langle \ln A \rangle$ from the unbiased data of X^{μ}_{max} allows the comparison with other mass composition measurements performed at the Pierre Auger Observatory.
In Fig. 8.13, $\langle \ln A \rangle$ from X^{μ}_{max} of this analysis (green points) is compared to the values of $\langle \ln A \rangle$ derived for X_{max} [105] (black points), and X^{μ}_{max} for inclined events [121] (red points). Each of these measurements has been discussed in Sec. 4.1 and 4.2.3 respectively. $\langle \ln A \rangle$ from each observable is shown as a function of the energy for EPOS-LHC (left panel) and QGSJetII-04 (right panel) hadronic interaction models.
By inspecting Fig. 8.13 the following conclusions can be drawn:

- $\langle \ln A \rangle$ from X^{μ}_{max} derived in this thesis is in agreement with the observed muonic elongation rate (Fig. 8.7), as already outlined.

- $\langle \ln A \rangle$ from the MPD analysis here described is fully compatible with the published one within the systematic uncertainties and for both hadronic interaction models.

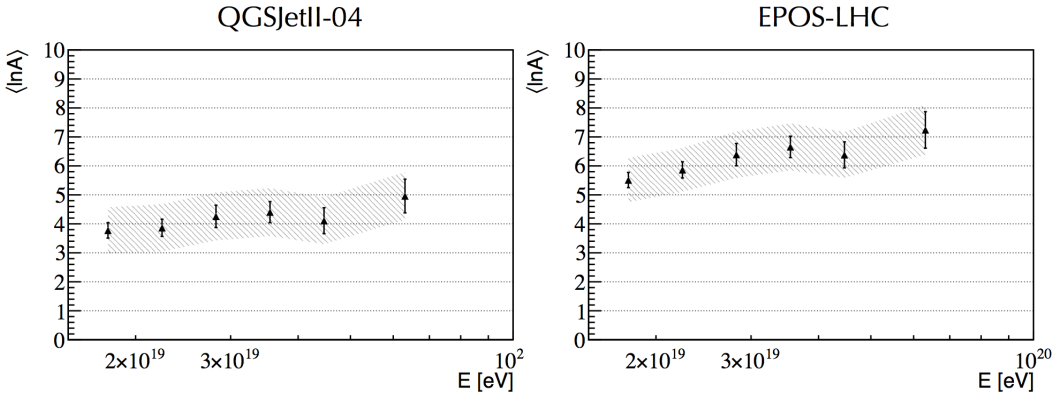

Figure 8.12: Average logarithmic mass $\langle \ln A \rangle$ as a function of the energy. EPOS-LHC (left panel) and QGSJetII- 04 (right panel) are used as reference models. Statistical (black bars) and systematic (grey shaded area) errors are indicated. See text for details.

The observed difference in the absolute value is due to the different ranges of the two analyses, being the published one performed for inclined events and in a more restricted interval of core distances (r>1700m).

- $\langle \ln A \rangle$ from X^{μ}_{max} and $\langle \ln A \rangle$ from X_{max} can be compared in the small energy range common to the two analyses. The results are incompatible at 6σ level if EPOS-LHC is considered, confirming that this model is not able to reproduce Auger data. If one instead considers QGSJetII-04, a compatibility of about 2.5σ for the two measurements is found.

On the basis of this comparison, one may confirm that EPOS-LHC is strongly disfavoured, whereas, considering QGSJetII-04, the measurements of X_{max} and X^{μ}_{max} are marginally compatible. However, the situation is even more puzzling. In fact, as discussed in Sec. 4.2.1 and reported in Fig. 4.8, QGSJetII-04 yields results of $\langle \ln A \rangle$ from $\sec(\theta)_{max}$ which are inconsistent at different distance ranges. This not happens for EPOS-LHC model. In addition, as shown in Sec. 4.1, considering V(lnA) from X_{max}, the model QGSJetII-04 leads to unphysical variances.
It is clear that all these measurements have very different systematic uncertainties and are sensitive to very different types of hadronic interactions. This is due to the different importance played by the muonic shower component for each of these measurements. In the case of X_{max} the main shower component is the electromagnetic one. As a consequence in that case the dominant contribution comes from the very first high energy hadronic interactions [140]. On the contrary, the muon production depth is dominated by the muon component which derives from long cascade of lower energy hadronic interactions (mostly pion-nucleus interactions) [141]. The risetime asymmetry is associated with a complex interplay between these two components [119].

However, a valid hadronic interaction model has to describe consistently all aspects of EAS physics and neither of the most-up-to-date hadronic interaction models seems to satisfactorily describe both the electromagnetic and the muonic components of the showers.

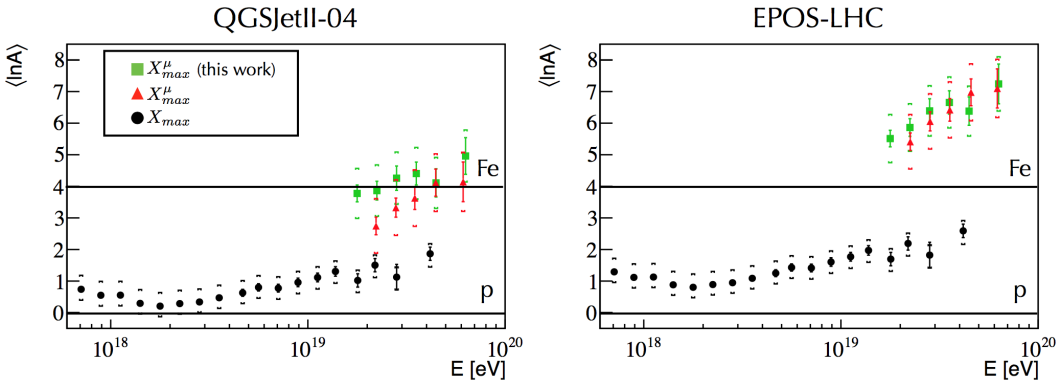

Figure 8.13: Evolution of $\langle \ln A \rangle$ with energy for X_{max} [105] (black points), X^{μ}_{max} for inclined events [121] (red triangles) and X^{μ}_{max} measured with the method described in this work (green squares), in the case of QGSJetII-04 (left panel) and EPOS-LHC (right panel).

Conclusions

The arrival times of particles from extensive air showers, collected by the surface detector of the Pierre Auger Observatory, have been exploited to measure the Muon Production Depth on 2268 events above 15 EeV, recorded in almost 13 years of data taking, between January 2004 and September 2016. It is worth to mention that the flux of ultra-high energy cosmic rays is extremely low in the energy range here analysed, and the composition measurements performed with the fluorescence detector suffer poor statistics, because of the low duty cycle of the telescopes.
By applying the method described in Chapter 6, the depth of maximum of the muon longitudinal development, X^{μ}_{max}, has been derived in a wide interval of zenith angles: [45°-65°]. This further increased the statistics of events at disposal. In addition, thanks to the extension of the applicability ranges of this analysis, the shower to shower fluctuations $\sigma_{sh}(X^{\mu}_{max})$ have been evaluated, exploiting the method discussed in Chapter 7.
X^{μ}_{max} is reconstructed with a total systematic uncertainty of 15 g/cm^2, the largest contribution coming from the mass and model spread. The shower-to-shower fluctuations of the muonic maximum are instead reconstructed with a systematic uncertainty of 11 g/cm^2 and also in this case the largest source of error is due to the mass and model spread. This uncertainties correspond respectively to about 20% and 30% of the proton-iron separation.
Both X^{μ}_{max} and $\sigma_{sh}(X^{\mu}_{max})$ contain information about the mass composition of the ultra-high energy cosmic rays: according to the results of this work, they give hints of a non-constant composition with increasing energy, between 15 EeV and 100 EeV. In particular, considering the shower-to-shower fluctuations, the composition results to be mixed-to-heavy at all energies. However, the large systematic uncertainties due to the hadronic interaction models prevent to get a stronger conclusion.
On the other hand, some more insights on hadronic interaction models have been obtained. In particular, EPOS-LHC is disfavoured by the X^{μ}_{max} analysis and this is further confirmed by the agreement of the energy evolution of X^{μ}_{max} with the published results [121], which are derived with a different MPD reconstruction method for inclined events.
An important outcome has been derived by the inspection of the evolution of X^{μ}_{max} with zenith angle: in particular, an increasing difference with expectations with growing inclination of the primary has been found in this work, as derived with other muon-related observables [47, 120].
Finally, by comparing the logarithm of the primary mass from different measurements performed at the Pierre Auger Observatory, a complex scenario has been highlighted. If one considers $\langle \ln A \rangle$ from X^{μ}_{max} derived in this thesis, it is in agreement with the published MPD $\langle \ln A \rangle$ results for both the considered hadronic interaction models. EPOS-

LHC turns out to be again disfavoured, because the composition seems to be dominated by elements heavier than iron. Most importantly, the inconsistency of EPOS-LHC results is highlighted when $\langle \ln A \rangle$ from X^{μ}_{max} is compared to $\langle \ln A \rangle$ from X_{max}: the measurements show a 6σ-level incompatibility.
For what concerns QGSJetII-04 model, $\langle \ln A \rangle$ from X^{μ}_{max} of this work and $\langle \ln A \rangle$ from X_{max} are marginally compatible, within 2.5σ, and a trend towards heavier composition is observed across the whole energy range between 0.6 EeV and 100 EeV. It is however interesting to point out that this model gives unphysical variances of lnA from X_{max} data [105] and yields also inconsistent results for the risetime asymmetry analysis [119].
By assuming that the most recent hadronic interaction models are a fair representation of reality, they should all be compatible, while on the contrary the discrepancies found from the different analyses point to possible failures of the models. The results reached in this thesis further underline the importance of the measurements of the muon components in air showers to investigate the hadronic interactions and test their models at the ultra-high energies.
An important step forward can be expected from the completion of the Pierre Auger Observatory upgrade [103], obtaining new additional composition-sensitive information, a reduction of the systematic uncertainties and opening the possibility to further investigate the hadronic interactions at the ultra-high energies.

List of Figures

List of Tables

Bibliography

[1] V. L. Ginzburg and S. I. Syrovatskii. *The Origin of Cosmic Rays*. New York: Macmillan, 1964.

[2] Mario Edoardo Bertaina. Cosmic rays from the knee to the ankle. *Comptes Rendus Physique*, 15(4):300 – 308, 2014.

[3] Veniamin Berezinsky, Askhat Gazizov, and Svetlana Grigorieva. On astrophysical solution to ultrahigh energy cosmic rays. *Phys. Rev. D*, 74:043005, Aug 2006.

[4] Karl-Heinz Kampert. Ultrahigh-energy cosmic rays: Results and prospects. *Brazilian Journal of Physics*, 43(5):375–382, 2013.

[5] Fermi E. Galactic magnetic fields and the origin of cosmic radiation. *Astrophysical Journal*, 119:1, January 1954.

[6] Andrei Bykov, Neil Gehrels, Henric Krawczynski, Martin Lemoine, Guy Pelletier, and Martin Pohl. Particle acceleration in relativistic outflows. *Space Science Reviews*, 173(1):309–339, 2012.

[7] Pisin Chen, Toshiki Tajima, and Yoshiyuki Takahashi. Plasma wakefield acceleration for ultrahigh-energy cosmic rays. *Phys. Rev. Lett.*, 89:161101, Sep 2002.

[8] Fan Guo, Hui Li, William Daughton, and Yi-Hsin Liu. Formation of Hard Powerlaws in the Energetic Particle Spectra Resulting from Relativistic Magnetic Reconnection. *Phys. Rev. Lett.*, 113:155005, 2014, 1405.4040.

[9] R. J. Protheroe. Origin and Propagation of the Highest Energy Cosmic Rays. In M. M. Shapiro, R. Silberberg, and J. P. Wefel, editors, *Towards the Millennium in Astrophysics, Problems and Prospects. International School of Cosmic Ray Astrophysics 10th Course*, page 3, 1998, astro-ph/9612213.

[10] Lagage P.O. and Cesarsky C.J. The maximum energy of cosmic rays accelerated by supernova shocks. *Astronomy and Astrophysics*, 125:249–257, September 1983.

[11] Hillas A.M. "The origin of ultra-high-energy cosmic rays". *Annual Review of Astronomy and Astrophysics*, 22:425–444, 1984.

[12] Anthony M. Hillas. Cosmic Rays: Recent Progress and some Current Questions. In *Conference on Cosmology, Galaxy Formation and Astro-Particle Physics on the Pathway to the SKA Oxford, England, April 10-12, 2006*, 2006, astro-ph/0607109.

[13] E. G. Berezhko. Maximum energy of cosmic rays accelerated by supernova shocks. *Astroparticle Physics*, 5:367–378, October 1996.

[14] V. Ptuskin, V. Zirakashvili, and E.-S. Seo. Spectrum of Galactic Cosmic Rays Accelerated in Supernova Remnants. *Astrophysical Journal*, 718:31–36, July 2010, 1006.0034.

[15] P. Blasi, R. I. Epstein, and A. V. Olinto. Ultra-High-Energy Cosmic Rays from Young Neutron Star Winds. *Astrophysical Journal Letters*, 533:L123–L126, April 2000, astro-ph/9912240.

[16] Jonathan Arons. Magnetars in the metagalaxy: an origin for ultrahigh-energy cosmic rays in the nearby universe. *Astrophys. J.*, 589:871–892, 2003, astro-ph/0208444.

[17] Ke Fang, Kumiko Kotera, and Angela V. Olinto. Ultrahigh Energy Cosmic Ray Nuclei from Extragalactic Pulsars and the effect of their Galactic counterparts. *JCAP*, 1303:010, 2013, 1302.4482.

[18] Pijushpani Bhattacharjee and Gunter Sigl. Origin and propagation of extremely high-energy cosmic rays. *Phys. Rept.*, 327:109–247, 2000, astro-ph/9811011.

[19] P. L. Biermann. TOPICAL REVIEW: The origin of the highest energy cosmic rays. *Journal of Physics G Nuclear Physics*, 23:1–27, January 1997.

[20] Eli Waxman. Cosmological gamma-ray bursts and the highest energy cosmic rays. *Phys. Rev. Lett.*, 75:386–389, 1995, astro-ph/9505082.

[21] C. J. Cesarsky. Cosmic rays with $E > 10^{19}$ eV : Origin and transport. *Nuclear Physics B Proceedings Supplements*, 28:51–60, November 1992.

[22] H. Kang, D. Ryu, and T. W. Jones. Cluster Accretion Shocks as Possible Acceleration Sites for Ultra–High-Energy Protons below the Greisen Cutoff. *Astrophysical Journal*, 456:422, January 1996, astro-ph/9507113.

[23] Kenneth Greisen. End to the cosmic-ray spectrum? *Phys. Rev. Lett.*, 16:748–750, Apr 1966.

[24] G. T. Zatsepin and V. A. Kuz'min. Upper Limit of the Spectrum of Cosmic Rays. *Soviet Journal of Experimental and Theoretical Physics Letters*, 4:78, August 1966.

[25] J. W. Cronin. The highest-energy cosmic rays. *Nuclear Physics B Proceedings Supplements*, 138:465–491, January 2005, astro-ph/0402487.

[26] Diego Harari. The flux suppression at the highest energies. *Comptes Rendus Physique*, 15:376–383, 2014, 1406.1117.

[27] T. E. Clarke, P. P. Kronberg, and H. Böhringer. A New Radio-X-Ray Probe of Galaxy Cluster Magnetic Fields. *The Astrophysical Journal*, 547:L111–L114, February 2001, astro-ph/0011281.

[28] P. P. Kronberg. Extragalactic magnetic fields. *Reports on Progress in Physics*, 57:325–382, April 1994.

[29] P. Blasi, S. Burles, and A. V. Olinto. Cosmological Magnetic Field Limits in an Inhomogeneous Universe. *The Astrophysical Journal*, 514:L79–L82, April 1999, astro-ph/9812487.

[30] W. Heitler. *The Quantum Theory of Radiation*. Oxford University Press, London, 1954.

[31] J. Matthews. A heitler model of extensive air showers. *Astroparticle Physics*, 22(5–6):387 – 397, 2005.

[32] T. K. Gaisser. *Cosmic Rays And Particle Physics*. Cambridge University Press, 1990.

[33] J. Alvarez-Muñiz, R. Engel, T. K. Gaisser, J. A. Ortiz, and T. Stanev. Hybrid simulations of extensive air showers. *Physical Review D*, 66(3):033011, August 2002, astro-ph/0205302.

[34] R. Ulrich, J. Blümer, R. Engel, F. Schüssler, and M. Unger. On the measurement of the proton-air cross section using air shower data. *New Journal of Physics*, 11(6):065018, 2009.

[35] J. Linsley. Structure of Large Air Showers at Depth 834 g cm^{-2} Fluctuations. *International Cosmic Ray Conference*, 12:62, 1977.

[36] Jorg R. Horandel. On total inelastic cross-sections and the average depth of the maximum of extensive air showers. *J. Phys.*, G29:2439–2464, 2003, astro-ph/0309010.

[37] D. Heck, J. Knapp, J. N. Capdevielle, G. Schatz, and T. Thouw. *CORSIKA: A Monte Carlo code to simulate extensive air showers*. Forschungszentrum Karlsruhe GmbH, 1998.

[38] S. J. Sciutto. AIRES: A System for air shower simulations. User's guide and reference manual. Version 2.2.0. 1999, astro-ph/9911331.

[39] T. Pierog, Iu. Karpenko, J. M. Katzy, E. Yatsenko, and K. Werner. EPOS-LHC: Test of collective hadronization with data measured at the CERN Large Hadron Collider. *Phys. Rev.*, C92(3):034906, 2015, 1306.0121.

[40] S. Ostapchenko. Monte carlo treatment of hadronic interactions in enhanced pomeron scheme: Qgsjet-ii model. *Phys. Rev. D*, 83:014018, Jan 2011.

[41] T. Pierog and K. Werner. Muon production in extended air shower simulations. *Phys. Rev. Lett.*, 101:171101, Oct 2008.

[42] Sergey Ostapchenko. QGSJET-II: Results for extensive air showers. *Nucl. Phys. Proc. Suppl.*, 151:147–150, 2006, astro-ph/0412591.

[43] Eun-Joo Ahn, Ralph Engel, Thomas K. Gaisser, Paolo Lipari, and Todor Stanev. Cosmic ray interaction event generator sibyll 2.1. *Phys. Rev. D*, 80:094003, Nov 2009.

[44] Felix Riehn, Ralph Engel, Anatoli Fedynitch, Thomas K. Gaisser, and Todor Stanev. A new version of the event generator Sibyll. 2015, 1510.00568.

[45] TOTEM Collaboration. The TOTEM Experiment at the CERN Large Hadron Collider. *Journal of Instrumentation*, 3:S08007, August 2008.

[46] T. Pierog, R. Engel, D. Heck, and G. Poghosyan. Future of Monte Carlo simulations of atmospheric showers. In *European Physical Journal Web of Conferences*, volume 89 of *European Physical Journal Web of Conferences*, page 01003, March 2015.

[47] Pierre Auger Collaboration, Alexander Aab, et al. Testing Hadronic Interactions at Ultrahigh Energies with Air Showers Measured by the Pierre Auger Observatory. *Phys. Rev. Lett.*, 117(19):192001, 2016, 1610.08509.

[48] Pierre Auger Collaboration, Alexander Aab, et al. The Pierre Auger Cosmic Ray Observatory. *Nucl. Instrum. Meth.*, A798:172–213, 2015, 1502.01323.

[49] H. Kawai et al. Proceedings of the xiv international symposium on very high energy cosmic ray interactions telescope array experiment. *Nuclear Physics B - Proceedings Supplements*, 175:221 – 226, 2008.

[50] John Linsley. Evidence for a primary cosmic-ray particle with energy 10^{20} ev. *Phys. Rev. Lett.*, 10:146–148, Feb 1963.

[51] M.A. Lawrence, R.J.O. Reid, and A.A. Watson. The cosmic ray energy spectrum above 4×10^{17}ev as measured by the haverah park array. *Journal of Physics G: Nuclear and Particle Physics*, 17(5):733, 1991.

[52] AGASA Collaboration. Akeno giant air shower array (agasa) covering 100 km2 area. *Nuclear Instruments and Methods in Physics Research Section A: Accelerators, Spectrometers, Detectors and Associated Equipment*, 311(1):338 – 349, 1992.

[53] M. Aglietta, G. Badino, L. Bergamasco, C. Castagnoli, A. Castellina, G. Cini, M. Dardo, B. D'Ettorre-Piazzoli, W. Fulgione, P. Galeotti, P. Ghia, G. Mannocchi,

C. Morello, G. Navarra, L. Periale, P. Picchi, O. Saavedra, G. Trinchero, P. Vallania, and S. Vernetto. The eas-top array at e0 = 10^{14}-10^{16} ev: Stability and resolutions. *Nuclear Instruments and Methods in Physics Research Section A: Accelerators, Spectrometers, Detectors and Associated Equipment*, 277(1):23 – 28, 1989.

[54] KASCADE Collaboration. The cosmic-ray experiment {KASCADE}. *Nuclear Instruments and Methods in Physics Research Section A: Accelerators, Spectrometers, Detectors and Associated Equipment*, 513(3):490 – 510, 2003.

[55] KASCADE-Grande collaboration. The kascade-grande experiment. *Nuclear Instruments and Methods in Physics Research Section A: Accelerators, Spectrometers, Detectors and Associated Equipment*, 620(2–3):202 – 216, 2010.

[56] V. A. Belyaev and A. E. Chudakov. Ionization glow of air and its possible use for air shower detection. *Bulletin of USSR Academy of Sciences, Phys. Ser.*, 30(10):1700, 1966.

[57] T. Hara, F. Ishikawa, S. Kawaguchi, Y. Miura, M. Nagano, K. Suga, and G. Tanahashi. Detection of the atmospheric scintillation light from air showers. *International Cosmic Ray Conference*, 3:369, 1970.

[58] D. J. Bird et al. Detection of a cosmic ray with measured energy well beyond the expected spectral cutoff due to cosmic microwave radiation. *Astrophys. J.*, 441:144–150, 1995, astro-ph/9410067.

[59] J. H. Boyer et al. Fadc-based {DAQ} for hires fly's eye. *Nuclear Instruments and Methods in Physics Research Section A: Accelerators, Spectrometers, Detectors and Associated Equipment*, 482(1-2):457 – 474, 2002.

[60] A. E. Chudakov, N. M. Nesterova, V. I. Zatsepin, and E. I. Tukish. Cerenkov radiation produced by extensive air showers of cosmic ray. *International Cosmic Ray Conference*, 2:50, 1960.

[61] A. Borione et al. A large air shower array to search for astrophysical sources emitting γ-rays with energies $\geq 10^{14}$ ev. *Nuclear Instruments and Methods in Physics Research Section A: Accelerators, Spectrometers, Detectors and Associated Equipment*, 346(1):329 – 352, 1994.

[62] S. F. Berezhnev et al. The Tunka-133 EAS Cherenkov light array: Status of 2011. *Nuclear Instruments and Methods in Physics Research A*, 692:98–105, November 2012, 1201.2122.

[63] A. A. Ivanov and L. V. Timofeev. Temporal signatures of the Cherenkov light induced by extensive air showers of cosmic rays detected with the Yakutsk array. *ArXiv e-prints*, April 2016, 1604.05088.

[64] J. R. Patterson and A. M. Hillas. The relation of the lateral distribution of Cerenkov light from cosmic-ray showers to the distance of maximum development. *Journal of Physics G Nuclear Physics*, 9:1433–1452, November 1983.

[65] Daniel Ferenc. The magic gamma-ray observatory. *Nuclear Instruments and Methods in Physics Research Section A: Accelerators, Spectrometers, Detectors and Associated Equipment*, 553(1-2):274–281, 2005. Proceedings of the fifth International Workshop on Ring Imaging DetectorsFifth International Workshop on Ring Imaging Detectors.

[66] J. Holder et al. Status of the VERITAS Observatory. *AIP Conf. Proc.*, 1085:657–660, 2009, 0810.0474.

[67] J. A. Hinton. The Status of the H.E.S.S. project. *New Astron. Rev.*, 48:331–337, 2004, astro-ph/0403052.

[68] M. Actis and others. Design concepts for the Cherenkov Telescope Array CTA: an advanced facility for ground-based high-energy gamma-ray astronomy. *Experimental Astronomy*, 32:193–316, December 2011, 1008.3703.

[69] J. V. Jelley, J. H. Fruin, N. A. Porter, T. C. Weekes, F. G. Smith, and R. A. Porter. Radio Pulses from Extensive Cosmic-Ray Air Showers. *Nature*, 205:327–328, January 1965.

[70] LOPES Collaboration. Detection and imaging of atmospheric radio flashes from cosmic ray air showers. *Nature*, 435:313–316, May 2005, astro-ph/0505383.

[71] D. Ardouin, A. Bellétoile, D. Charrier, R. Dallier, L. Denis, P. Eschstruth, T. Gousset, F. Haddad, J. Lamblin, P. Lautridou, A. Lecacheux, D. Monnier-Ragaigne, A. Rahmani, and O. Ravel. Radio-detection signature of high-energy cosmic rays by the CODALEMA experiment. *Nuclear Instruments and Methods in Physics Research A*, 555:148–163, December 2005, astro-ph/0504297.

[72] F. G. Schröder. Radio detection of high-energy cosmic rays with the Auger Engineering Radio Array. *Nuclear Instruments and Methods in Physics Research A*, 824:648–651, July 2016, 1601.00462.

[73] P. A. Bezyazeekov et al. Measurement of cosmic-ray air showers with the Tunka Radio Extension (Tunka-Rex). *Nuclear Instruments and Methods in Physics Research A*, 802:89–96, December 2015, 1509.08624.

[74] M. P. van Haarlem et al. LOFAR: The LOw-Frequency ARray. *Astronomy and Astrophysics*, 556:A2, August 2013, 1305.3550.

[75] S. Argiro, S. L. C. Barroso, J. Gonzalez, L. Nellen, Thomas Cantzon Paul, T. A. Porter, L. Prado, Jr., M. Roth, R. Ulrich, and D. Veberic. The Offline Software Framework of the Pierre Auger Observatory. *Nucl. Instrum. Meth.*, A580:1485–1496, 2007, 0707.1652.

[76] M. Takeda et al. Extension of the cosmic ray energy spectrum beyond the predicted Greisen-Zatsepin-Kuz'min cutoff. *Phys. Rev. Lett.*, 81:1163–1166, 1998, astro-ph/9807193.

[77] I. Allekotte et al. The Surface Detector System of the Pierre Auger Observatory. *Nucl. Instrum. Meth.*, A586:409–420, 2008, 0712.2832.

[78] X. Bertou, P.S. Allison, C. Bonifazi, P. Bauleo, C.M. Grunfeld, M. Aglietta, F. Arneodo, D. Barnhill, J.J. Beatty, N.G. Busca, A. Creusot, D. Dornic, A. Etchegoyen, A. Filevitch, P.L. Ghia, I. Lhenry-Yvon, M.C. Medina, E. Moreno, D. Nitz, T. Ohnuki, S. Ranchon, H. Salazar, T. Suomijärvi, D. Supanitsky, A. Tripathi, M. Urban, and L. Villasenor. Calibration of the surface array of the pierre auger observatory. *Nuclear Instruments and Methods in Physics Research Section A: Accelerators, Spectrometers, Detectors and Associated Equipment*, 568(2):839 – 846, 2006.

[79] Pierre Auger Collaboration, J. Abraham, et al. Trigger and aperture of the surface detector array of the pierre auger observatory. *Nuclear Instruments and Methods in Physics Research Section A: Accelerators, Spectrometers, Detectors and Associated Equipment*, 613(1):29 – 39, 2010.

[80] K. Kamata and J. Nishimura. The Lateral and the Angular Structure Functions of Electron Showers. *Progress of Theoretical Physics Supplement*, 6:93–155, 1958.

[81] K. Greisen. Cosmic ray showers. *Ann. Rev. Nucl. Part. Sci.*, 10:63–108, 1960.

[82] A. M. Hillas, J. D. Hollows, H. W. Hunter, and D. J. Marsden. Calculations on the particle and energy-loss densities in extensive air showers at large axial distances. *International Cosmic Ray Conference*, 3:533, 1970.

[83] David Newton, J. Knapp, and A. A. Watson. The Optimum Distance at which to Determine the Size of a Giant Air Shower. *Astropart. Phys.*, 26:414–419, 2007, astro-ph/0608118.

[84] Carla Bonifazi, A. Letessier-Selvon, and E. M. Santos. A model for the time uncertainty measurements in the Auger surface detector array. *Astropart. Phys.*, 28:523–528, 2008, 0705.1856.

[85] J. Hersil, I. Escobar, D. Scott, G. Clark, and S. Olbert. Observations of extensive air showers near the maximum of their longitudinal development. *Phys. Rev. Lett.*, 6:22–23, Jan 1961.

[86] C. Bonifazi and Pierre Auger Collaboration. The angular resolution of the Pierre Auger Observatory. *Nuclear Physics B Proceedings Supplements*, 190:20–25, May 2009, 0901.3138.

[87] A. Schulz. The measurement of the energy spectrum of cosmic rays above 3×10^{17} eV with the Pierre Auger Observatory. In *Proceedings, 33rd International Cosmic Ray Conference (ICRC2013): Rio de Janeiro, Brazil, July 2-9, 2013*, 2013.

[88] R. Pesce. Energy calibration of data recorded with the surface detectors of the Pierre Auger Observatory: An update. In *Proceedings, 32nd International Cosmic Ray Conference (ICRC 2011): Beijing, China, August 11-18, 2011*, volume 2, page 214, 2011.

[89] V. Verzi. The Energy Scale of the Pierre Auger Observatory. In *Proceedings, 33rd International Cosmic Ray Conference (ICRC2013): Rio de Janeiro, Brazil, July 2-9, 2013*, page 0928, 2013.

[90] D. Ravignani. Measurement of the energy spectrum of cosmic rays above 3×10^{17} eV using the AMIGA 750 m surface detector array of the Pierre Auger Observatory. In *Proceedings, 33rd International Cosmic Ray Conference (ICRC2013): Rio de Janeiro, Brazil, July 2-9, 2013*, 2013.

[91] H. P. Dembinski, P. Billoir, O. Deligny, and T. Hebbeker. A phenomenological model of the muon density profile on the ground of very inclined air showers. *Astropart. Phys.*, 34:128–138, 2010, 0904.2372.

[92] Pierre Auger Collaboration, J. Abraham, et al. The Fluorescence Detector of the Pierre Auger Observatory. *Nucl. Instrum. Meth.*, A620:227–251, 2010, 0907.4282.

[93] Fernando Arqueros, Joerg R. Hoerandel, and Bianca Keilhauer. Air Fluorescence Relevant for Cosmic-Ray Detection - Summary of the 5th Fluorescence Workshop, El Escorial 2007. *Nucl. Instrum. Meth.*, A597:1–22, 2008, 0807.3760.

[94] M. Giller, G. Wieczorek, A. Kacperczyk, H. Stojek, and W. Tkaczyk. Energy spectra of electrons in the extensive air showers of ultra-high energy. *Journal of Physics G: Nuclear and Particle Physics*, 30(2):97, 2004.

[95] Frank Nerling, J. Bluemer, R. Engel, and M. Risse. Universality of electron distributions in high-energy air showers: Description of Cherenkov light production. *Astropart. Phys.*, 24:421–437, 2006, astro-ph/0506729.

[96] M. D. Roberts. The role of atmospheric multiple scattering in the transmission of fluorescence light from extensive air showers. *Journal of Physics G: Nuclear and Particle Physics*, 31(11):1291, 2005.

[97] J. PeĶala, P. Homola, B. Wilczyńska, and H. Wilczyński. Atmospheric multiple scattering of fluorescence and Cherenkov light emitted by extensive air showers. *Nuclear Instruments and Methods in Physics Research A*, 605:388–398, July 2009, 0904.3230.

[98] M. Giller and A. Śmiałkowski. An analytical approach to the multiply scattered light in the optical images of the extensive air showers of ultra-high energies. *Astroparticle Physics*, 36:166–182, August 2012, 1201.4052.

[99] T. K. Gaisser and A. M. Hillas. Reliability of the method of constant intensity cuts for reconstructing the average development of vertical showers. *International Cosmic Ray Conference*, 8:353–357, 1977.

[100] Matias J. Tueros. Estimate of the non-calorimetric energy of showers observed with the fluorescence and surface detectors of the Pierre Auger Observatory. In *Proceedings, 33rd International Cosmic Ray Conference (ICRC2013): Rio de Janeiro, Brazil, July 2-9, 2013*, page 0705, 2013.

[101] Pierre Auger Collaboration, J. Abraham, et al. A study of the effect of molecular and aerosol conditions in the atmosphere on air fluorescence measurements at the Pierre Auger Observatory. *Astroparticle Physics*, 33:108–129, March 2010, 1002.0366.

[102] P. Abreu et al. The Pierre Auger Observatory V: Enhancements. In *Proceedings, 32nd International Cosmic Ray Conference (ICRC 2011): Beijing, China, August 11-18, 2011*, 2011, 1107.4807.

[103] Pierre Auger Collaboration, Alexander Aab, et al. The Pierre Auger Observatory Upgrade - Preliminary Design Report. 2016, 1604.03637.

[104] I. Valino. The flux of ultra-high energy cosmic rays after ten years of operation of the Pierre Auger Observatory. *PoS*, ICRC2015:271, 2016.

[105] Pierre Auger Collaboration, A. Aab, et al. Depth of maximum of air-shower profiles at the Pierre Auger Observatory. I. Measurements at energies above $10^{17.8}$ eV. *Phys. Rev.*, D90(12):122005, 2014, 1409.4809.

[106] Pierre Auger Collaboration, Telescope Array Collaboration, R. Abbasi, et al. Report of the Working Group on the Composition of Ultra High Energy Cosmic Rays. *JPS Conf. Proc.*, 9:010016, 2016, 1503.07540.

[107] E. Barcikowski, J. Bellido, J. Belz, Y. Egorov, S. Knurenko, V. de Souza, Y. Tameda, Y. Tsunesada, and M. Unger. Mass Composition Working Group Report at UHECR-2012. *EPJ Web Conf.*, 53:01006, 2013, 1306.4430.

[108] Karl-Heinz Kampert and Michael Unger. Measurements of the cosmic ray composition with air shower experiments. *Astroparticle Physics*, 35(10):660 – 678, 2012.

[109] O. Deligny. Large-Scale Distribution of Arrival Directions of Cosmic Rays Detected at the Pierre Auger Observatory and the Telescope Array above 10^{19} eV. In *Pierre Auger Observatory and Telescope Array: Joint Contributions to the 34th International Cosmic Ray Conference (ICRC 2015)*, 2015, 1511.02103.

[110] Pierre Auger Collaboration, A. Aab, et al. Searches for Anisotropies in the Arrival Directions of the Highest Energy Cosmic Rays Detected by the Pierre Auger Observatory. *Astrophys. J.*, 804(1):15, 2015, 1411.6111.

[111] W. H. Baumgartner, J. Tueller, C. B. Markwardt, G. K. Skinner, S. Barthelmy, R. F. Mushotzky, P. A. Evans, and N. Gehrels. The 70 month swift-bat all-sky hard x-ray survey. *The Astrophysical Journal Supplement Series*, 207(2):19, 2013.

[112] C. Bleve. Update of the neutrino and photon limits from the Pierre Auger Observatory. In *Proceedings, 34rd International Cosmic Ray Conference (ICRC2015): The Hague, The Netherlands, July 30-August 6, 2015*, 2015.

[113] R. Ulrich. Extension of the measurement of the proton-air cross section with the Pierre Auger Observatory. In *Proceedings, 34rd International Cosmic Ray Conference (ICRC2015): The Hague, The Netherlands, July 30-August 6, 2015*, 2015.

[114] Pedro Abreu et al. Interpretation of the Depths of Maximum of Extensive Air Showers Measured by the Pierre Auger Observatory. *JCAP*, 1302:026, 2013, 1301.6637.

[115] Pierre Auger Collaboration, A. Aab, et al. Depth of maximum of air-shower profiles at the Pierre Auger Observatory. II. Composition implications. *Phys. Rev.*, D90(12):122006, 2014, 1409.5083.

[116] Pierre Auger Collaboration, Alexander Aab, et al. Evidence for a mixed mass composition at the ankle in the cosmic-ray spectrum. *Phys. Lett.*, B762:288–295, 2016, 1609.08567.

[117] R. Aloisio, D. Boncioli, A di Matteo, A. F. Grillo, S. Petrera, and F. Salamida. Cosmogenic neutrinos and ultra-high energy cosmic ray models. *JCAP*, 1510(10):006, 2015, 1505.04020.

[118] A. Di Matteo. Combined fit of spectrum and composition data as measured by the Pierre Auger Observatory. *PoS*, ICRC2015:249, 2016.

[119] Pierre Auger Collaboration, Alexander Aab, et al. Azimuthal Asymmetry in the Risetime of the Surface Detector Signals of the Pierre Auger Observatory. *Phys. Rev.*, D93(7):072006, 2016, 1604.00978.

[120] Pierre Auger Collaboration, A. Aab, et al. Muons in air showers at the Pierre Auger Observatory: Mean number in highly inclined events. *Phys. Rev.*, D91(3):032003, 2015, 1408.1421. [Erratum: Phys. Rev.D91,no.5,059901(2015)].

[121] Pierre Auger Collaboration, A. Aab, et al. Muons in air showers at the Pierre Auger Observatory: Measurement of atmospheric production depth. *Phys. Rev.*, D90(1):012012, 2014, 1407.5919. [Erratum: Phys. Rev.D92,no.1,019903(2015)].

[122] M. T. Dova, M. E. Mancenido, Analisa G. Mariazzi, H. Wahlberg, F. Arqueros, and D. Garcia-Pinto. Time asymmetries in extensive air showers: a novel method to identify UHECR species. *Astropart. Phys.*, 31:312–319, 2009, 0903.1755.

[123] L. Cazon, R. Conceicao, M. Pimenta, and E. Santos. A model for the transport of muons in extensive air showers. *Astropart. Phys.*, 36:211–223, 2012, 1201.5294.

[124] S. Andringa, L. Cazon, R. Conceicao, and M. Pimenta. The Muonic longitudinal shower profiles at production. *Astropart. Phys.*, 35:821–827, 2012, 1111.1424.

[125] Pierre Auger Collaboration, Alexander Aab, et al. Reconstruction of inclined air showers detected with the Pierre Auger Observatory. *JCAP*, 1408(08):019, 2014, 1407.3214.

[126] Collica L. for the Pierre Auger Collaboration. Measurement of the Muon Production Depths at the Pierre Auger Observatory. *Eur. Phys. J. Plus*, 131(9):301, 2016, 1609.02498.

[127] L. Collica. *Mass composition studies of Ultra High Energy cosmic rays through the measurement of the Muon Production Depths at the Pierre Auger Observatory*. PhD thesis, Universita' Degli Studi Di Milano, Dipartimento di Fisica, 2014.

[128] L. Collica, M. Mallamaci, A. Castellina, and B. Caccianiga. A comprehensive study of the X_{μ}^{max} bias in an extended angular and energy range. Internal Auger GAP Note (62), 2015.

[129] L. Collica, M. Mallamaci, A. Castellina, and B. Caccianiga. Measurement of the X_{max}^{μ} and of its fluctuations above $10^{19.2}$ eV. Internal Auger GAP Note (32), 2016.

[130] L. Cazon, R. A. Vazquez, A. A. Watson, and Enrique Zas. Time structure of muonic showers. *Astropart. Phys.*, 21:71–86, 2004, astro-ph/0311223.

[131] L. Cazon. *Modelling the muon time distribution in extensive air showers*. PhD thesis,

Dipartimento di Fisica, Universitá degli Studi di Milano, 2014.

[132] Pierre Billoir. A sampling procedure to regenerate particles in a ground detector from a thinned air shower simulation output. *Astroparticle Physics*, 30(5):270 – 285, 2008.

[133] Pierre Auger Collaboration, A. Aab, et al. Erratum: Muons in air showers at the pierre auger observatory: Measurement of atmospheric production depth [phys. rev. d90, 012012(2014)]. *Phys. Rev. D*, 92:019903, Jul 2015.

[134] A. Bueno, D. Gamez, and L. Molina Bueno. Towards a full understanding of the different contributions to X^{μ}_{max} bias. Internal Auger GAP Note (34), 2015.

[135] D. Gamez and L. Molina Bueno. The resampling algorithm in offline: bias in the time of the particles injected in the surface detectors. Internal Auger GAP Note (6), 2015.

[136] B. Zamorano. *Inferring the mass composition of Ultra-High Energy Cosmic Rays through the characterisation of the muon production profile*. PhD thesis, Dpto. de Física Teórica y del Cosmos & CAFPE, Universidad de Granada, 2014.

[137] M.T. Dova, F.G. Monticelli, and H. Wahlberg. Influence of the reconstructed core position on S(1000) for inclined showers. Internal Auger GAP Note (35), 2006.

[138] M. Horvata and D. Veberic. On shower-front start-time variance. Internal Auger GAP Note (57), 2007.

[139] L. Cazon, R. Conceicao, C. Espirito-Santo, M. Oliveira, M. Pimenta, A. Bueno, and D. Garcia-Gamez. Consistency between X_{max} and X^{μ}_{max} as a way to test hadronic models. Internal Auger GAP Note (68), 2012.

[140] Ralf Ulrich, Colin Baus, and Ralph Engel. Relation between hadronic interactions and ultra-high energy extensive air showers. *EPJ Web Conf.*, 99:11001, 2015.

[141] Sergey Ostapchenko and Marcus Bleicher. Constraining pion interactions at very high energies by cosmic ray data. *Phys. Rev. D*, 93:051501, Mar 2016.

Acknowledgments

I consider my PhD as a member of the Pierre Auger Collaboration in the Milano group a unique experience that enabled me to really express myself and grow. For this reason, I have to thank my supervisor, Prof. Lino Miramonti, and all people of the Milano group. A special thank is for Dott. Barbara Caccianiga, who followed me during all the period of the PhD and helped me a lot in taking forward the work of this thesis. I would like to thank a lot the *ALABAMA* group, formed by myself and Barbara, and by Dott. Laura Collica and Dott. Antonella Castellina from Torino University. During these 3 years, we worked together on the MPD very hard and with a lot of passion for reaching solid scientific results. I thank my referees, Prof. Antonio Insolia from Catania University and Prof. Mosé Mariotti from Padova University, I am very grateful for your time. I thank the full Pierre Auger Collaboration, every single person I met during the collaboration meetings in Argentina and all over the world. I loved so much traveling and knowing interesting people and valuable scientists from different countries.
My thanks go also to my family: my husband who understands me and supported me with his love during the hard periods, my father, my mother and my brother who have always believed in me and in my skills, and all other members of my family and friends, because each of them is a precious and cherished gift that God donated to me.